JOURNAL OF FOOD PROCESS ENGINEERING

D.R. HELDMAN
and
R.P. SINGH
COEDITORS

FOOD & NUTRITION PRESS, INC.

VOLUME 19, NUMBER 4 NOVEMBER 1996

JOURNAL OF FOOD PROCESS ENGINEERING

All articles for publication and inquiries regarding publication should be sent to DR. D.R. HELDMAN, COEDITOR, *Journal of Food Process Engineering*, Food Science/Engineering Unit, University of Missouri-Columbia, 235 Agricultural/Engineering Bldg., Columbia, MO 65211 USA; or DR. R.P. SINGH, COEDITOR, *Journal of Food Process Engineering*, University of California, Davis, Department of Agricultural Engineering, Davis, CA 95616 USA.

All subscriptions and inquiries regarding subscriptions should be sent to Food & Nutrition Press, Inc., 6527 Main Street, P.O. Box 374, Trumbull, CT 06611 USA.

One volume of four issues will be published annually. The price for Volume 19 is $149.00, which includes postage to U.S., Canada, and Mexico. Subscriptions to other countries are $172.00 per year via surface mail, and $183.00 per year via airmail.

Subscriptions for individuals for their own personal use are $119.00 for Volume 19, which includes postage to U.S., Canada and Mexico. Personal subscriptions to other countries are $142.00 per year via surface mail, and $153.00 per year via airmail. Subscriptions for individuals should be sent directly to the publisher and marked for personal use.

The *Journal of Food Process Engineering* is listed in *Current Contents/Agriculture, Biology & Environmental Sciences (CC/AB)*, and SciSearch, and Research Alert.

The *Journal of Food Process Engineering* (ISSN:0145-8876) is published quarterly (March, June, September and December) by Food & Nutrition Press, Inc.—Office of Publication is 6527 Main Street, P.O. Box 374, Trumbull, Connecticut 06611 USA.

Second class postage paid at Bridgeport, CT 06602

POSTMASTER: Send address changes to Food & Nutrition Press, Inc., 6527 Main Street, P.O. Box 374, Trumbull, Connecticut 06611 USA.

JOURNAL OF FOOD PROCESS ENGINEERING

JOURNAL OF FOOD PROCESS ENGINEERING

Journal of FOOD PROCESS ENGINEERING

VOLUME 19
NUMBER 4

Coeditors: D.R. HELDMAN
R.P. SINGH

FOOD & NUTRITION PRESS, INC.
TRUMBULL, CONNECTICUT 06611 USA

ISSN 0145-8876

Printed in the United States of America

F N P PUBLICATIONS IN FOOD SCIENCE AND NUTRITION

Journals

JOURNAL OF FOOD LIPIDS, F. Shahidi
JOURNAL OF RAPID METHODS AND AUTOMATION IN MICROBIOLOGY, D.Y.C. Fung and M.C. Goldschmidt
JOURNAL OF MUSCLE FOODS, N.G. Marriott, G.J. Flick, Jr. and J.R. Claus
JOURNAL OF SENSORY STUDIES, M.C. Gacula, Jr.
JOURNAL OF FOODSERVICE SYSTEMS, C.A. Sawyer
JOURNAL OF FOOD BIOCHEMISTRY, J.R. Whitaker, N.F. Haard and H. Swaisgood
JOURNAL OF FOOD PROCESS ENGINEERING, D.R. Heldman and R.P. Singh
JOURNAL OF FOOD PROCESSING AND PRESERVATION, D.B. Lund
JOURNAL OF FOOD QUALITY, J.J. Powers
JOURNAL OF FOOD SAFETY, T.J. Montville
JOURNAL OF TEXTURE STUDIES, M.C. Bourne and M.A. Rao

Books

HACCP: MICROBIOLOGICAL SAFETY OF MEAT AND POULTRY, J.J. Sheridan, R.L. Buchanan and T.J. Montville
OF MICROBES AND MOLECULES: FOOD TECHNOLOGY AT M.I.T., S.A. Goldblith
MEAT PRESERVATION: PREVENTING LOSSES AND ASSURING SAFETY, R.G. Cassens
S.C. PRESCOTT, M.I.T. DEAN AND PIONEER FOOD TECHNOLOGIST, S.A. Goldblith
FOOD CONCEPTS AND PRODUCTS: JUST-IN-TIME DEVELOPMENT, H.R. Moskowitz
MICROWAVE FOODS: NEW PRODUCT DEVELOPMENT, R.V. Decareau
DESIGN AND ANALYSIS OF SENSORY OPTIMIZATION, M.C. Gacula, Jr.
NUTRIENT ADDITIONS TO FOOD, J.C. Bauernfeind and P.A. Lachance
NITRITE-CURED MEAT, R.G. Cassens
POTENTIAL FOR NUTRITIONAL MODULATION OF AGING, D.K. Ingram *et al.*
CONTROLLED/MODIFIED ATMOSPHERE/VACUUM PACKAGING OF FOODS, A.L. Brody
NUTRITIONAL STATUS ASSESSMENT OF THE INDIVIDUAL, G.E. Livingston
QUALITY ASSURANCE OF FOODS, J.E. Stauffer
THE SCIENCE OF MEAT AND MEAT PRODUCTS, 3RD ED., J.F. Price and B.S. Schweigert
HANDBOOK OF FOOD COLORANT PATENTS, F.J. Francis
ROLE OF CHEMISTRY IN PROCESSED FOODS, O.R. Fennema *et al.*
NEW DIRECTIONS FOR PRODUCT TESTING OF FOODS, H.R. Moskowitz
ENVIRONMENTAL ASPECTS OF CANCER: ROLE OF FOODS, E.L. Wynder *et al.*
FOOD PRODUCT DEVELOPMENT AND DIETARY GUIDELINES, G.E. Livingston, R.J. Moshy and C.M. Chang
SHELF-LIFE DATING OF FOODS, T.P. Labuza
ANTINUTRIENTS AND NATURAL TOXICANTS IN FOOD, R.L. Ory
UTILIZATION OF PROTEIN RESOURCES, D.W. Stanley *et al.*
VITAMIN B_6: METABOLISM AND ROLE IN GROWTH, G.P. Tryfiates
POSTHARVEST BIOLOGY AND BIOTECHNOLOGY, H.O. Hultin and M. Milner

Newsletters

MICROWAVES AND FOOD, R.V. Decareau
FOOD INDUSTRY REPORT, G.C. Melson
FOOD, NUTRITION AND HEALTH, P.A. Lachance and M.C. Fisher

CONTENTS

NMR IMAGING, CALORIMETRIC, AND MATHEMATICAL MODELING STUDIES OF FOOD FREEZING

W.L. KERR[1,4], R.J. KAUTEN[2], M. OZILGEN[3], M.J. McCARTHY[2] and D.S. REID[2]

Department of Food Science and Technology
[1]University of Georgia, Athens, GA 30602
[2]University of California, Davis, CA 95616

[3]Food Engineering Department
Middle East Technical University, 06531 Ankara, Turkey

Accepted for Publication November 30, 1995

ABSTRACT

Nuclear magnetic resonance imaging (MRI), calorimetry, and temperature measurements were used to monitor cylindrical potato sections frozen at -11C and -42C. MRI showed the advance of the nonsymmetric freezing zone and loss of signal intensity as liquid water turned to ice. Differential calorimetry was used to follow heat removal during transient freezing. Measured times to 95% enthalpy change were 24 min (-42C) and 49 min (-11C), as compared to modeled values of 29 min (-42C) and 100 min (-11C). Times to 95% change in the NMR signal, integrated over the area of the image, were 21 min (-42C) and 56 min (- 11C). Changes in NMR signal intensity could be correlated with the amount of unfrozen water remaining after a steady-state had been reached. At -42C, NMR indicated 25% unfrozen water remaining as compared to 26% by calorimetry, and 22% by modeling. At -11C, NMR measured 67% unfrozen water remaining as compared to 48% by calorimetry, and 25% by equilibrium modeling.

INTRODUCTION

Freezing of foods is a major means of food preservation. Lowering the temperature of a food while converting water to ice helps limit the growth of microorganisms, slows deleterious chemical reactions, and in some cases, imparts desirable sensory qualities to the food. It is important to predict or monitor food freezing processes for several reasons. Overall, it is necessary to know the total heat removed from a product in going from its initial state to its steady state frozen storage temperature, as this value determines the refrigeration

Author for Correspondence

Journal of Food Process Engineering **19** (1996) 363–384.

requirements for freezing. In many cases, this can be estimated from tables describing enthalpy values for foods as a function of temperature (Dickerson 1968; ASHRAE 1993). In research settings, it can be measured directly by adiabatic calorimetry (Reidel 1951; Charm and Moody 1966; Fleming 1969).

The assessment of transient freezing processes is also critical due to its impact on product quality, equipment design, and energy costs. The rate of freezing effects the temperature history of the food as well as the size and distribution of ice crystals within the product. For most foods, optimal quality is obtained with rapid freezing, as smaller ice crystals and less cell dehydration are obtained (Reid 1983, 1990). Once the specified enthalpy change has been accomplished, further time spent in the freezer wastes energy and limits throughput. Conversely, it is crucial that the product remain in the freezer as long as necessary. Frozen storage rooms are designed to prevent further heat gain or loss, and may not have the capacity to remove additional heat from a product that arrives underfrozen. In addition, freezing in such a room is likely to be slower and result in lower product quality.

To date, the primary means of measuring or predicting food freezing rates have been through thermometric measurements during freezing or mathematical modeling of freezing. In the former, thermocouples are embedded in the food while it is frozen (Cleland and Earle 1979; de Michelis and Calvelo 1983; Hung and Thompson 1983; Purwadaria and Heldman 1982). This provides a recorded history of temperature profiles within the material. Freezing rate has been defined in several ways, such as by dividing the surface to center distance by the time required for the surface to reach 0C and the thermal center to reach 5C below the freezing temperature (IIR 1971). More common is the concept of "freezing time", such as the time required for the slowest cooling point to decrease from 0C to -5C (Heldman and Singh 1981). Monitoring freezing by changes in temperature can be problematic. First, it does not lend itself to inline processing conditions. Second, the presence of thermocouples may provide additional heat conduction paths to the sample or alter air flow patterns. In addition, temperature is an insensitive measure of extent of freezing; for example, a frozen product at -4C may have a much larger fraction of unfrozen water than one at -5C.

Many mathematical models have been proposed for predicting freezing rates or times. The extensive literature covering these methods has been reviewed by Hung and Thompson (1980), Cleland and Earle (1984), Hung (1990), Cleland (1990), and Kluza (1994). Various approaches can be classified as either analytical or numerical (Hung 1990). Analytical solutions are simple to use but incorporate questionable assumptions. However, several empirical methods exist which have reasonable predictive value (Cleland 1990).

It is untenable to obtain an exact solution for heat conduction in a system undergoing a gradual phase change, and in which the pertinent physical

properties vary with temperature. Numerical techniques, such as finite element models, overcome these difficulties by describing average properties within segmented volumes of the material. Enthalpy formulation methods have been used for many decades to describe processes involving phase change (Dusinberre 1949, 1962; Rose 1960; Solomon 1966; Voller and Cross 1981, 1985). A program made available by Mannapperuma and Singh (1988, 1989) uses finite difference methods to simulate freezing and thawing of different geometries. This program runs on personal computers and can also be used to estimate the properties of foods during freezing.

In the past few years, several methods have become available for monitoring freezing progress. Kerr *et al.* (1993) describe a differential compensated calorimeter which can be used to follow heat removal in foods during freezing. The advantage of this system over adiabatic calorimetry is that samples are frozen within the freezer of interest, rather than in the calorimeter itself. Thus energy changes during the course of freezing can be followed in addition to the overall changes between steady states.

Another important tool which can be applied to freezing is magnetic resonance imaging (MRI). MRI has proven invaluable in noninvasive medical research and diagnosis (Morris 1986), as well as in food research (McCarthy 1994). Data obtained with MRI have been used successfully in association with mathematic modeling to describe aspects of food processing operations (McCarthy and McCarthy 1994; Heil *et al.* 1992; McCarthy *et al.* 1991a). Recently, MRI technology has been applied to characterization of freezing processes (McCarthy *et al.* 1991b; McCarthy and Kauten 1990; McCarthy *et al.* 1989; Fyfe *et al.* 1989). In particular, MRI is useful for visualizing the freezing interface zone, while quantifying the number of liquid water molecules.

In this study, thermometry, calorimetry, and MRI were combined to study potatoes freezing in a commercial air blast freezer. This allowed alternative views for assessing freezing, by showing the time evolution of temperature, heat content, fraction of water frozen, and freezing interface position. Results were compared with an enthalpy-based numerical model which incorporates each of these parameters. Each approach was evaluated in terms of its ability to describe steady state changes as well as freezing rates.

MATERIAL AND METHODS

Freezing Process

Potatoes were chosen for this study as they are a major frozen commodity, are homogeneous, and are easily cut into regular geometric shapes. Samples of white potato were prepared by cutting cylindrical cores 3.5 cm in diameter and 6 cm in length. This allowed for relatively uniform air flow around the samples,

and facilitated mathematical modeling. All samples were weighed on a top loading balance (PE 2000, Mettler Corp., Highstown, NJ), with a typical sample weighing about 55 g.

Freezing was accomplished using a Frigoscandia (Sweden) laboratory air-blast freezer (Fig. 1). The freezer was modified so that it could deliver cold air through an insulated 6 m section of PVC pipe (7.6 cm ID). The PVC pipe continued through the center of the MRI bore before returning to the intake of the freezer. An insulated NMR probe was constructed to fit tightly over the PVC pipe. Air temperature was monitored with a thermocouple placed near the sample. Air velocity was adjusted with a diversion valve to between 2-10 m/s, and measured with a Model HH-30 anemometer (Omega, Stamford, CT).

The sample was introduced into the pipe by means of a push rod. The rod was equipped with a platform made of two 1/4 in. (0.64 cm) diameter wood dowels. These contacted the sample at two points and kept it suspended, and centered it within the diameter of the pipe. The rod was 1.2 m long and inserted after removing an endcap from where the PVC pipe exited the magnet. A locating pin at the end opposite the sample fixed the sample so that it was directly within the confines of the imaging coil.

Nuclear Magnetic Resonance Imaging

The sample was placed in the freezer tube and within a 10 cm "birdcage" imaging coil. The coil size was selected so as to maximize the filling factor of the RF coils, thereby enhancing the signal-to-noise ratio. MRI images were obtained using a CSI-2 Fourier Transform NMR Spectrometer (General Electrical Medical Systems, Fremont, CA), tuned to the hydrogen nuclear frequency of 85.53 MHz. A spin-echo pulse sequence was used in imaging the samples (Morris 1986).

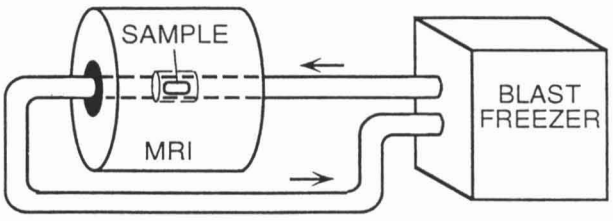

FIG. 1. EXPERIMENTAL SET-UP FOR MONITORING POTATO FREEZING USING MAGNETIC RESONANCE IMAGING

Images were plotted directly to a Tektronix 4634 plotter (Beaverton, OR). Raw data files were also kept and ported to an Apple MacIntosh Quadra computer (Cupertino, CA). This allowed further analysis of the data. For example, images were color-enhanced through the Spyglass image analysis software (Spyglass, Inc., Champaign, IL) to facilitate detection of the freezing interface. In other cases, data were analyzed with the MathCAD mathematics program (MathSoft, Inc., Cambridge, MA).

Temperature Profiles During Freezing

Temperatures within a sample were monitored by a series of thermocouples placed along the sample axis parallel to the air flow. Thermocouples were constructed from 0.01 in. diameter copper and constantan wire. A trial and error procedure was required to find the proper length of wire that caused the least noise in the MRI images. The thermocouples were inserted 1 cm from the front surface and at the center of the sample. The leads were fed out through a 2mm opening in the PVC pipe and connected to a Molytech 32-channel datalogger (Pittsburgh, PA). MRI images were made of longitudinal slices through the sample, allowing precise definition of thermocouple placement. By staggering collection of temperature and MRI image data, the best image quality was maintained. In addition, MRI images were taken in subsequent experiments without thermocouples present in the sample.

Differential Calorimetry

A differential compensated type calorimeter was used to monitor heat removal during freezing. Details on its construction and operation are given by Kerr *et al.* (1993). The calorimeter uses two identical vessels, so that any heat loss from the sample chamber is compensated for by the reference chamber. Careful control of the calorimeter temperature was not required, as the calorimeter fluid (water) was at the same temperature as the surrounding room. The differential temperature between the vessels was measured by a multijunction thermocouple.

Samples were removed from the freezer at regular intervals during transient freezing; a new sample was placed in the freezer for each time interval to be explored. By compiling data for several samples, a plot of heat removal versus time in the freezer could be formed for each set of freezer conditions. Once removed from the freezer, the samples were immediately introduced into the sample vessel. As heat was dissipated into the sample chamber, a temperature difference developed between sample and reference chambers. A controlled heater was used to eliminate any temperature differential. The amount of energy introduced into the sample by the heater measures the amount of heat removed from the sample within the freezer.

Thermophysical Properties

Thermal properties for potato were required for numerical calculations of freezing times. The initial freezing point (T_f) for raw potato was determined by differential scanning calorimetry. Values of density (ρ), enthalpy (H), heat capacity (C_p), and thermal conductivity (k) were calculated from potato composition data as described by Mannaperuma and Singh (1989). A phase diagram was constructed using the formula (Kerr *et al.* 1993):

$$\begin{aligned}\Delta H = &(1-x)C_{p,H_2O}(T_i - T_f)\\ &+Y\Delta H_{lat}+yC_{p,ice}(T_f - T)\\ &+(1-y-x)C_{p,H_2O}(T_f - T)\\ &+xC_{p,solids}(T_i - T)\end{aligned} \quad (1)$$

where

x	=	weight fraction of solids
y	=	weight fraction of ice
C_{p,H_2O}	=	4.19 J/g°C
$C_{p,ice}$	=	1.89 J/g°C
$C_{p,solids}$	=	1.256 J/g°C
ΔH_{lat}	=	333.6 J/g
T_i	=	Initial product temperature
T_f	=	Freezing point of product
T	=	Average temperature at specified time

Heat Transfer Coefficents

Heat transfer coefficents (h) were determined using a model system in a manner similar to that of Flores and Mascheroni (1988). An aluminum cylinder was machined to the same dimensions as the potato samples (3.5 cm diam × 6 cm length), and a thermocouple positioned at its center to monitor temperature (T_c). The cylinder was placed in the freezer in identical conditions as the potato samples. Assuming a negligible thermal gradient exists across the aluminum cylinder, a heat balance gives

$$v\rho C_p \frac{dT_c}{dt} = hA(T_A - T_C) \quad (2)$$

where V is the cylinder volume, A is the surface area, T_A is the ambient temperature, ρ is the density, and C_p the heat capacity of the aluminum cylinder.

Integration of Eq. 2 yields

$$\ln\left(\frac{T_A - T_o}{T_A - T_C}\right) = \frac{hA}{V\rho C_p}t \tag{3}$$

Where T_o is the initial cylinder temperature. Thus, h can be determined from the slope of a semilogarithmic plot of normalized temperature versus time.

An alternative estimate for heat transfer coefficients was determined from calorimetry data of the potato samples. At t=0, no thermal gradient exists across the potato and heat transfer is limited at the surface; thus, initial heat flow is $q_o = hA(T_A - T_o)$. This heat flow in J/s can be determined from the slope of a line tangent to the heat removal curves at zero time.

RESULTS AND DISCUSSION

Thermophysical Properties

Calculated values of density (ρ), specific heat (C_p), enthalpy (H), and thermal conductivity (k) for raw potato as a function of temperature are shown in Table 1. The initial freezing point as measured by DSC was T_f = - 1.2C. An equilibrium phase diagram for potato is shown in Fig. 2.

Surface heat transfer coefficients (h) are shown in Fig. 3, which plots the Nusselt number $N_{NU} = \frac{Hd}{k}$ versus the Reynolds number $N_{Re} = \frac{\rho dV}{\mu}$ where D is the pipe diameter, k the thermal conductivity, ρ the density, v the velocity, and μ the viscosity of air. N_{Re} ranged from 19,700 to 92,900. A least squares fit showed the data is well represented by the power law (r=0.91)

$$N_{Nu} = 0.35N_{Re}^{0.6} \tag{4}$$

MRI Images

Figure 4a shows a series of MRI images taken during freezing of potato at -42C (air velocity: v =7.9 ms^{-1}). The presence of mobile water is indicated by greater signal intensity (brighter regions), whereas loss of signal intensity (darker regions) occurs upon freezing. Image resolution was 620 μm. Also shown for each image is an intensity profile plot along the central axis. As can

TABLE 1.
ESTIMATED THERMAL PROPERTIES OF RAW POTATO

TEMP (°C) (°C)	ρ (kg/m^3)	C_p (kJ/kgK)	Enthalpy[1] (kJ/kg)	k (W/mK)
-52.1	1022	2.17	-26.98	2.021
-39.3	1022	2.30	1.61	1.908
-32.9	1022	2.41	16.71	1.849
-26.5	1022	2.56	32.64	1.787
-20.1	1022	2.86	49.95	1.719
-16.9	1023	3.13	59.55	1.681
-13.7	1024	3.60	70.29	1.637
-10.5	1025	4.55	83.19	1.582
-8.9	1026	5.44	91.15	1.546
-7.3	1028	6.98	101.00	1.502
-5.7	1031	9.98	114.30	1.439
-4.9	1033	12.69	123.30	1.395
-4.1	1035	17.13	135.08	1.336
-3.3	1040	25.18	151.67	1.252
-2.9	1043	31.92	163.01	1.193
-2.5	1047	42.16	177.69	1.116
-2.1	1052	58.77	197.59	1.011
-1.9	1056	71.28	210.54	0.941
-1.7	1061	88.46	226.42	0.855
-1.5	1067	112.93	246.39	0.745
-1.4	1070	129.30	258.49	0.677
-1.3	1075	149.63	272.42	0.599
-1.2	1080	175.16	288.59	0.508
0	1080	3.65	292.98	0.510
15	1079	3.66	347.91	0.534
30	1079	3.67	402.98	0.557

[1]Referenced to H=0 kJ/kg at -40°C

be seen from the image at t=0, the change in full signal intensity from the potato to the low signal intensity of the surrounding space occurs over an approximately 1 mm region. The 2-dimensional image results from averaging the signal across the width of the cylinder and projecting into a rectangular plane. Thus, the initial ramping edge may be due to slight misalignments of the cylinder with respect to the MRI probe, or to cylinder faces which are not perfectly flat. In addition, contributions to the signal intensity gradation occurs due to changes which occur over the finite ($\sim$2 min) imaging time.

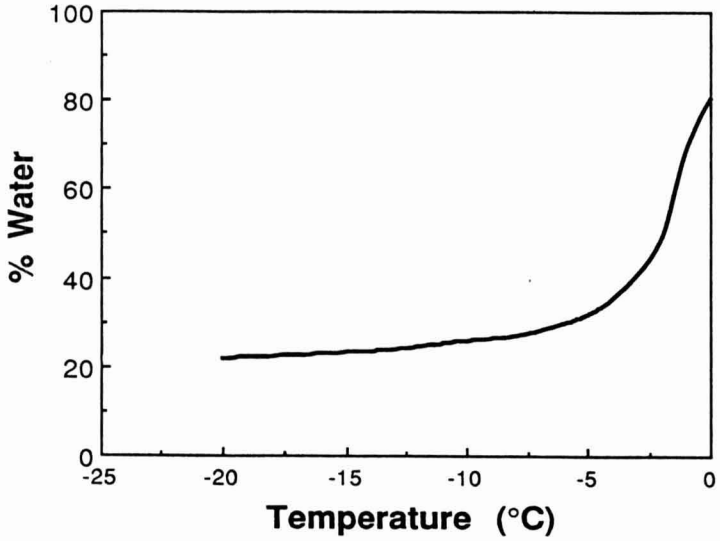

FIG. 2. PHASE DIAGRAM FOR RAW POTATO AT TEMPERATURES BETWEEN -20C (Tg′) AND -1.2C (T_m)

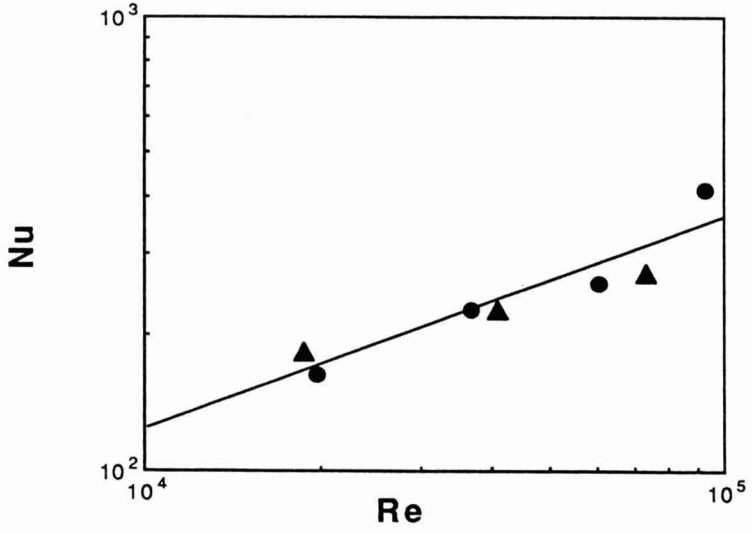

FIG. 3. DEPENDENCE OF HEAT TRANSFER COEFFICIENTS ON FLOW RATE EXPRESSED AS Nu=hD/k VS Re=ρDv/μ
▲ calorimetric method, ● aluminum cylinder method

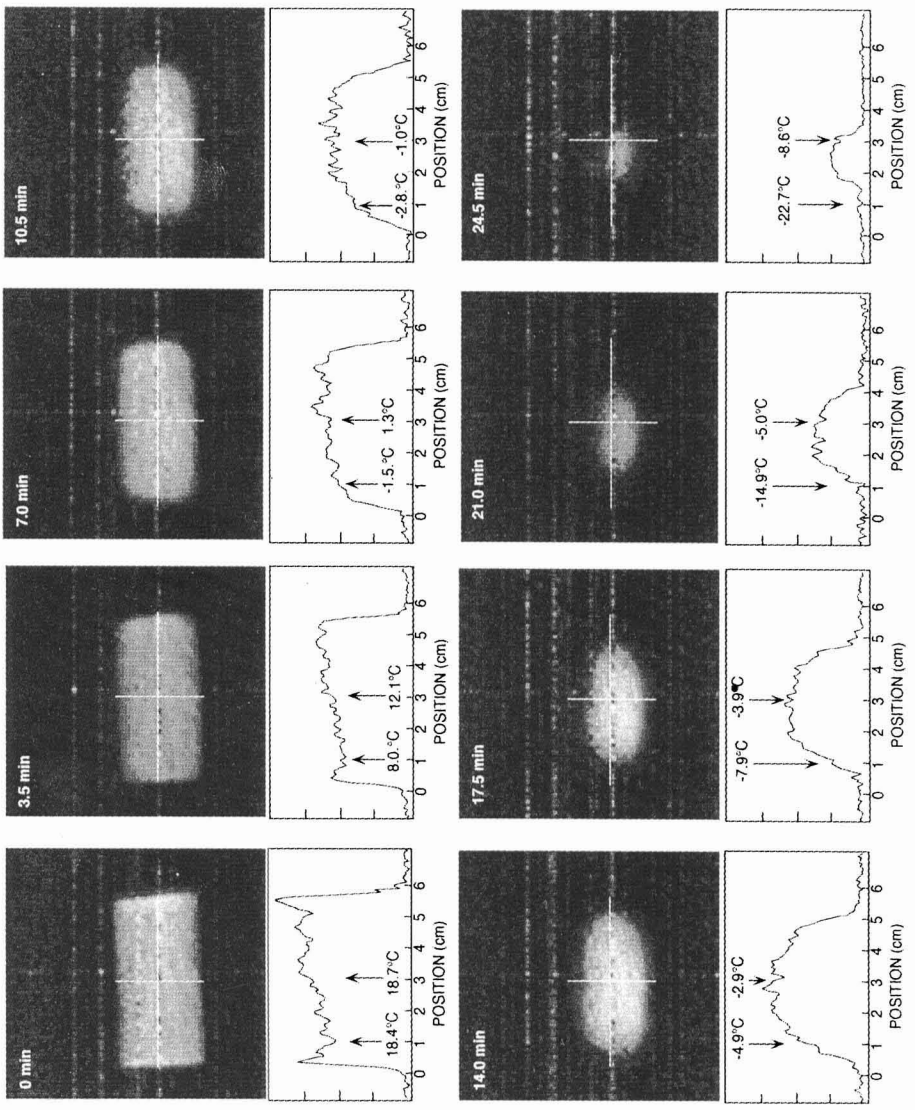
0 min
18.4°C
18.7°C
3.5 min
8.0°C
12.1°C
7.0 min
-1.5°C
1.3°C
10.5 min
-2.8°C
-1.0°C
14.0 min
-4.9°C
-2.9°C
17.5 min
-7.9°C
-3.9°C
21.0 min
-14.9°C
-5.0°C
24.5 min
-22.7°C
-8.6°C
POSITION (cm)
0 1 2 3 4 5 6

(A)

(B)

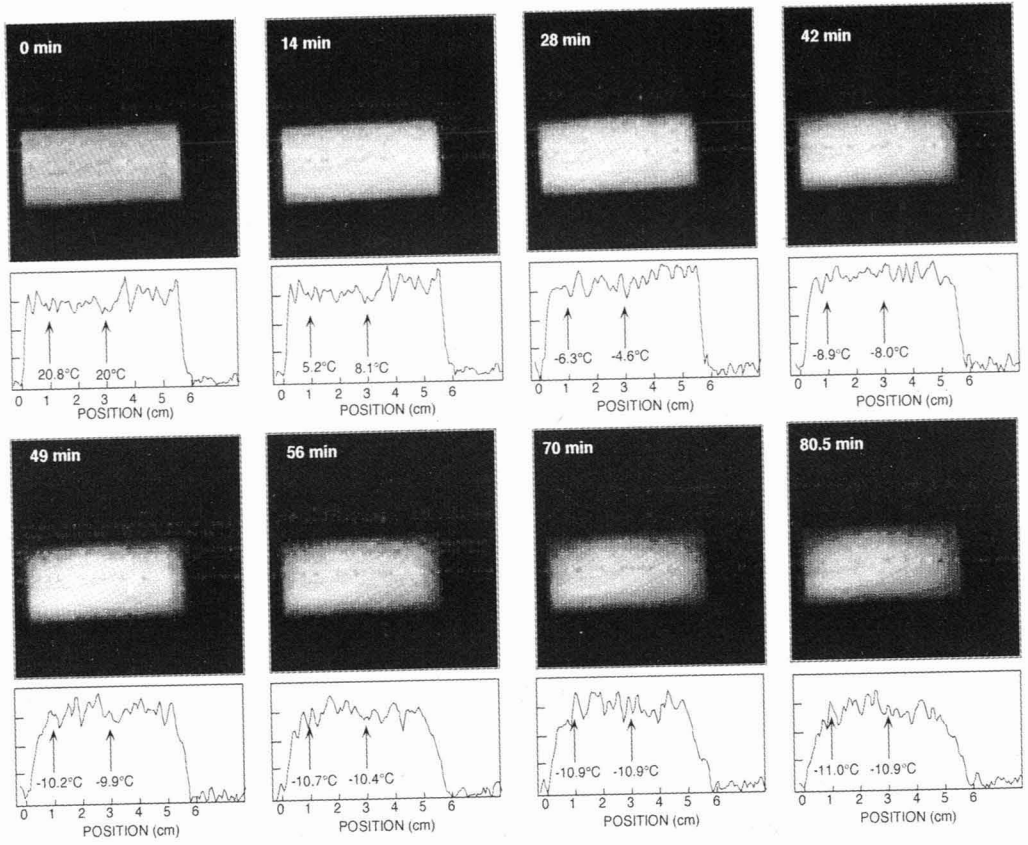

FIG. 4. MAGNETIC RESONANCE IMAGES OF POTATO DURING FREEZING AT (A) T_A=-42C, V=7.9 MS^{-1} AND (B) T_A=-11C, V=2.1 MS^{-1} Contour plots indicate NMR signal intensity along central axis of image. Dashed lines in image show position where T=-1.2C as predicted by numerical model of Mannaperuma and Singh (1989). Vertical lines in contour plots show temperature at positions 1 and 3 cm from front surface.

As freezing progresses, the intensity of outer regions of the potato become similar to the background value. In addition, the transition from low to high signal regions becomes more gradual. This occurs due to the 3-dimensional nature of the freezing process; that is, freezing occurs both radially and longitudinally. As freezing continues, the initially cylindrical volume of unfrozen water becomes smaller in all directions and more like a spherical ellipsoid. Thus, signal averaging across the radial direction produces a steeper slope and a lessening of overall intensity.

A different pattern developed when freezing occurred at -11C (υ=2.1 ms^{-1}) [Fig. 4b]. Here, no distinguishable interface formed, even after 80.5 min, at which time calorimetry and visual inspection indicated that significant freezing had occurred. As time passed, some fuzziness did develop in the images at the periphery of the potato. In addition, overall signal intensity decreased with time.

Two factors need to be considered when assessing signal intensity and interface position. The first relates to the temperature dependence of the NMR signal. At lower temperatures, proton mobility is decreased as randomization of an initially polarized population of protons is diminished. This results in both greater initial magnetization as well as potentially larger relaxation time constants (McCarthy 1994). The signal intensity (S_w) is inversely related to the absolute temperature by:

$$S_w = \rho_{w1} \left[\frac{1}{\Theta} \right] \exp \left[\frac{-TE}{T_{21}} \right] \tag{5}$$

where ρ_{w1} is the density of liquid water protons, TE is the echo time, T_{21} is the spin-spin relaxation time of liquid water protons, and Θ is the absolute temperature.

Temperature also directly affects the ρ_{w1} term in Eq. 5, at temperatures below the initial freezing temperature (T_m). As temperature is lowered below T_m = -1.2C, the fraction of unfrozen water decreases as the liquid phase becomes increasingly concentrated in solutes. For example, for equilibrated potato at a temperature just above -1.2C, the 81% water all exists in the liquid state. At T = -5C, the percent of unfrozen water is 33%; the remaining 47% exists as ice. As the system is progressively cooled, a temperature is reached below which no further freeze-concentration occurs. At lower temperatures, the liquid phase becomes glassy. The temperature at which the system enters the glass phase is denoted T_g'. For raw potato, T_g' = -20C (Ju 1994). This means that while temperature gradients exist across the potato, frozen regions more centrally located will contain more unfrozen water than those near the exterior. Thus,

each volume element (voxel) containing liquid water may not contain the same amount of liquid water as surrounding voxels.

Temperature effects on signal intensity were calculated and plotted in Fig. 5. Temperature profiles within a potato were estimated using the freezing model of Mannaperuma and Singh (1989). Filled circles show temperatures as a function of distance from the surface, up to a position half way through the potato. The values shown were calculated for the following conditions:

T_a = ambient freezer temperature = - 42C
Ti = initial product temperature = 25C
h = heat transfer coefficient = 75 W/m^{2}K

For each position, values of ρ_{wl} = %UFW were determined from Fig. 2. For $T > T_m$, %UFW was measured as 81%; for $T < T_g'$, %UFW was 22%. Finally, NMR signal strength emanating from each position was estimated from Eq. 5, with 1/Ø temperature correction.

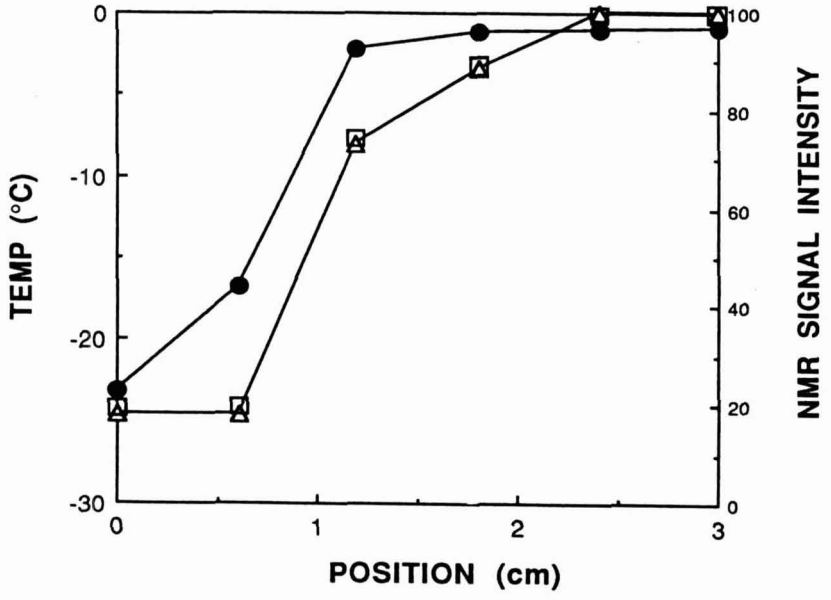

FIG. 5. EFFECT OF TEMPERATURE ON NMR SIGNAL INTENSITY ALONG CENTRAL AXIS OF POTATO

(●) Temperature profile predicted by numerical model; (□) NMR signal intensity corrected for temperature dependence (Eq. 1); (Δ) NMR signal intensity corrected for effects of varying unfrozen water with temperature (Eq. 2).

The plots in Fig. 5 indicate that at a given time, NMR signal intensity would vary in a region over which ice is still actively developing. Comparisons of signal plots with and without 1/Ø temperature correction showed that while the absolute value and temperature sensitivity would be expected to differ, the transitions between different regions still occur at the same temperatures. At positions where $T > T_m$, maximum liquid water exists and the signal is greatest. At temperatures $T < T_g'$, maximum ice formation has occurred, and the signal takes its lowest value. At temperatures below this, the fraction of unfrozen water is glassy and remains constant.

For situations in which freezing occurs at temperatures above T_g', substantial liquid water may still reside in the frozen product. For freezing at -11C, at least 25% of the product would be unfrozen, liquid water. This explains why no distinct interface develops in these conditions, although signal intensity does diminish. That is, although ice may be forming in the potato, enough liquid water exists to contribute to a substantial NMR signal.

Temperature Profiles

Center temperatures (T_c) are plotted versus time in Fig. 6. T_c reached lower final values and decreased at a faster rate for lower ambient temperatures. At T_a = -42C, 95% of the temperature change is accomplished in 28 min, 50% in 13 min; at -11C, 95% of the change occurs in 45 min, 50% in 32 min (Table 2). Temperatures are also shown in Fig. 4. Here, measurements are shown in comparison with MRI images, and in particular indicating the time at which the thermocouples at positions 1 and 3 cm from the front surface first register at -1.2C. At T_a = -42C, the thermocouple at 1 cm measures a temperature of -1.2C after 7 min; the thermocouple at 3 cm measures -1.2C after 10.5 min. As can be seen, the freezing temperature is reached within the interior of the potato prior to formation of the imaged interface. This suggests that portions of the food may undercool before ice actually forms.

Calorimetry

Figure 7 shows the heat removed from potatoes during freezing at -42C (air speed: 7.9 ms^{-1}) and at -11C (air speed: 2.1 ms^{-1}). Table 2 shows a list of characteristics describing the heat removal curves. Heat removal was initially faster at -42C (67 J $g^{-1}min^{-1}$) than at -11C (10 J $g^{-1}min^{-1}$). This reflects both the greater heat transfer due to a larger temperature differential, as well as a greater heat transfer coefficient due to increased air velocity. The maximum amount of heat removed was 346 J g^{-1} at -42C, and 203 J g^{-1} at -11C. The larger heat removal at -42C occurs due to a larger ice content at that temperature as well as the larger sensible heat change.

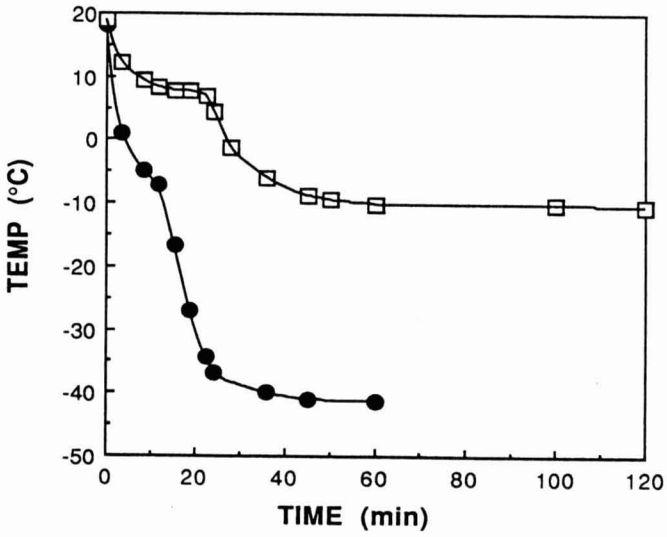

FIG. 6. CENTER TEMPERATURE (T_C) OF POTATO DURING FREEZING AT (●) T_A=-42C, V=7.9 MS^{-1} AND (□) T_A=-11C, V=2.1 MS^{-1}

TABLE 2.
TIME REQUIRED TO ACCOMPLISH 50 AND 95% CHANGE DURING FREEZING OF POTATOES

Percent Change	Freezer Temp	NMR Signal	Time (min) Calorimetry	Time (min) Numerical Model	Time (min) Center Temp
50	-42C	8	7	11	13
95	-42C	21	24	29	28
50	-11C	17	13	36	32
95	-11C	56	49	100	45

Freezing time can be described in terms of the time required for some portion of the energy change to occur. Table 2 shows times for 50 and 95% of the total change to be completed. At -42C, these times were 7 and 24 min, respectively; at -11C, they were 13 and 29 min.

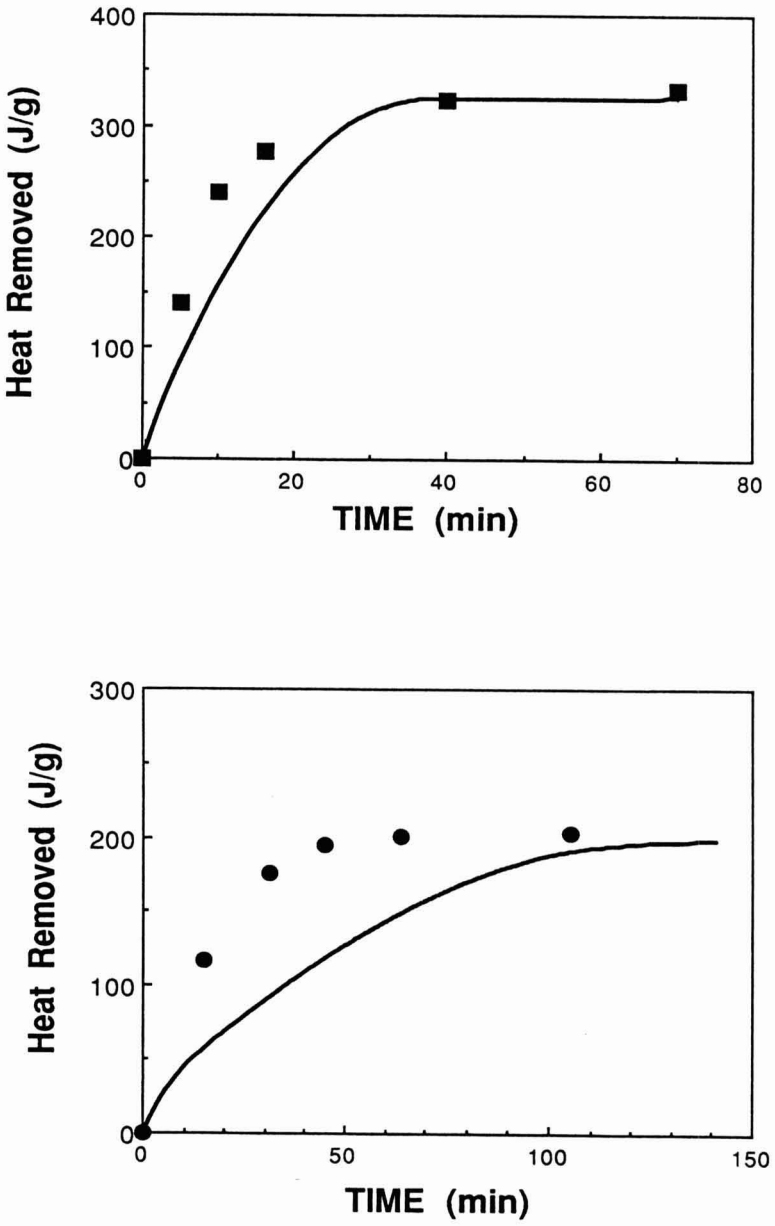

FIG. 7. HEAT REMOVED FROM FREEZING POTATOES AT (A) T_A=-42C AND (B) T_A=-11C AS DETERMINED BY DIFFERENTIAL CALORIMETRY
Bold lines show heat removal as predicted by numerical modeling, using measured heat transfer coefficients (Fig. 3).

Numerical Modeling of Freezing

The enthalpy based numerical freezing model of Mannaperuma and Singh (1988, 1989) was used to analyze freezing data, assuming a finite-cylinder geometry. Thermophysical properties of potato used are shown in Table 1. Heat transfer coefficents were taken from the best linear fit of data in Fig. 3. For freezing at -42C and $\upsilon = 7.9$ ms^{-1}, h = 75 W/m^{2}K; for freezing at -11C and $\upsilon = 2.1$ ms^{-1}, h = 47 W/m^{2}K.

The solid lines in Fig. 7 show calculated heat removal versus time as compared to experimental calorimetry data (filled symbols). Table 2 shows times required for 50 and 95% of heat removal to be accomplished. The numerical model predicted a 5.1% larger total heat removal at -42C (364 kJ/kg vs 346 kJ/kg by calorimetry). At -11C, the predicted total heat removal was 40% larger (284 kJ/kg vs 203 kJ/kg).

The predicted rate of heat removal was much lower, particularly at -11C. For example, at -42C the time to 95% heat removal was 24 min compared to a predicted value of 29 min; at -11C the time to 95% heat removal was 49 min compared to a predicted value of 100 min.

The discrepancy between measured and calculated total heat removal may be contributed to difficulties in assigning thermal properties to frozen foods. However, the fact that the measured enthalpy change was some 40% less than expected at -11C suggests that other factors may contribute. One possibility is that the potato freezing at - 11C never became fully equilibrated. This could be due to lack of nucleation in some of the cells; freeze-concentration of cell solutes during slow freezing would depress the cell freezing point, and may lower the nucleation temperature below -11C. Evidence for the importance of undercooling in food freezing has been shown by Kerr *et al.* (1993b).

Differences between measured and modeled freezing rates could be attributed to several factors. First, numerical modeling is a pseudo-equilibrium approach, where freezing is assumed to occur at the equilibrium freezing point. As mentioned above, equilibrium may not have been achieved. Similarly, the freezing interface may not exist at T_f throughout the product because initial freezing increases solute concentrations and progressively decreases the freezing point. Second, the accuracy of measured heat transfer coefficients is always suspect. In addition, our modeling assumed uniform heat transfer over all surfaces, which evidenced by the MRI images, is not the case.

NMR Signal Intensity

Apart from the spatial information provided by MRI, the NMR signal intensity is related to the fraction of liquid water at each voxel. By integrating over all voxels in the sample, a total NMR signal is obtained which is related to liquid water content. Figure 8 shows total NMR signal intensity versus time

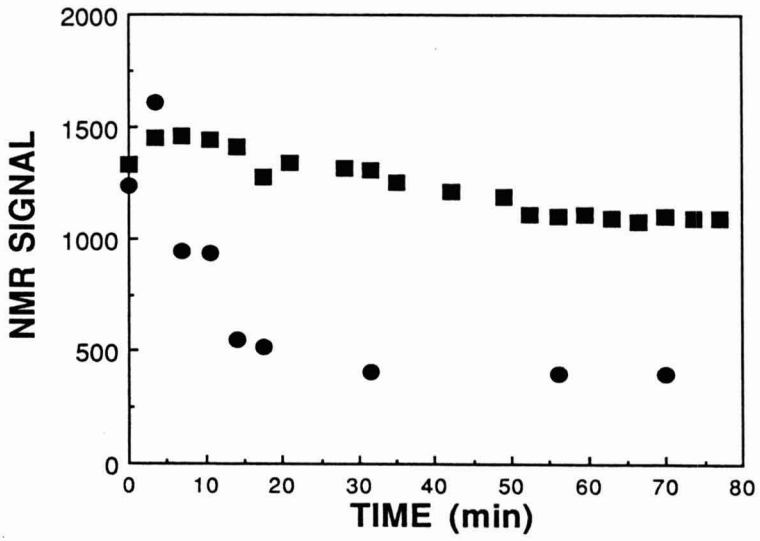

FIG. 8. CHANGE IN INTEGRATED NMR SIGNAL DURING FREEZING OF POTATOES AT (●) T_A=-42C AND (■) T_A=-11C

for potatoes freezing at -42C and -11C. As can be seen, at -42C the signal decreases to about a third of its initial value within 20 to 30 min. At -11C, the signal decreases more gradually to a final value about three-fourths of its initial value. The time required for 50% and 95% of the change to occur was 8 and 21 min at -42C, 17 and 56 min at -11C (Table 2). As compared to calorimetry data, the NMR signal reached a 95% change level 3 min (12% less) before calorimetry values at -42C; at -11C, NMR signal lagged the calorimetry values by 7 min (14% greater).

Due to the thermal gradients across the sample, it was not possible in this experiment to calculate the liquid water content during transient freezing from NMR signal intensity. However, estimates were made for steady-state values assuming the product approaches a constant temperature and the initial and final NMR signals can be corrected for temperature effects as shown in Eq. 5. With this approach, it was calculated that at -42C, 25% of the product remains as unfrozen water (56% as ice) while at -11C, 67% remains as unfrozen water (14% as ice) (Table 3). This compares to the equilibrium phase diagram values of 22% unfrozen water at -42C and 25% at -11C. Similarly, calorimetrically determined enthalpy changes were used in Eq. 1 to calculate unfrozen water remaining; this gave values of 26% unfrozen water after freezing at -42C, 48% at -11C. Both the calorimetry and NMR data support the notion that less than maximum ice formation occurred during freezing at -11C.

TABLE 3.
UNFROZEN WATER REMAINING AFTER
FREEZING AT -42C AND -11C

Freezer Temp	% Unfrozen Water		
	NMR Signal	Calorimetry	Numerical Model
-42C	25	26	22
-11C	67	48	25

CONCLUSIONS

Each of the methods presented offers a unique view of the freezing process. For example, calorimetry measures the heat removed during freezing. This parameter is of importance to food processors as it directly determines the energy requirements for freezing. The rate of heat removal can also be related to the rate of ice production. This is important because it affects quality aspects such as the size of ice crystals in the food. The enthalpy data did emphasize one problem with freezing times, namely, determining when freezing is complete. For convenience, we chose times at which 50% and 95% of the total heat was removed. A useful aspect of relying on calorimetry measurements is that these decisions can be made based on energy costs.

The magnetic resonance images were particularly useful for visualizing the freezing process, allowing one to see when ice is formed and how it moves through the product. In the simple case of cylindrical potatoes, it showed that ice does not form symmetrically about the product. This points out one difficulty in modeling freezing, namely how to describe heat transfer over the entire surface of a product. This becomes even more difficult for irregularly shaped products. Kerr *et al.* (1993b) have used MRI to image freezing in a number of products including salmon, chicken legs, corn, and carrots. These foods typically have irregular geometries that cannot easily be modeled; however, ice formation can be discerned readily by MRI.

One way of linking NMR information to freezing is by following the signal intensity integrated over the whole region of the imaged food. This value is related to the fraction of unfrozen liquid water in the food. The time required for a 95% change agreed to within 14% of that found by calorimetry. Steady-state signal intensities showed 25% of the product remaining as unfrozen water as compared to 26% by calorimetry and 22% by modeling. At -11C, NMR and calorimetry both indicated more unfrozen water than predicted by equilibrium considerations.

Thermocouples were used to monitor temperature at two places in the product. Temperature is a critical factor in freezing as it determines the state of the product, chemical reaction rates, and physical properties such as diffusion rates. The rate of temperature change can be used as an indication of freezing progress. However, a direct relationship could not be formed with product enthalpy, as a complete temperature map was not obtained by these experiments. In addition, nonequilibrium conditions limit our ability to relate temperature with thermophysical properties. For example, comparisons of temperature measurements and MRI images indicate that substantial undercooling may occur in some regions before ice formation ensues.

In conclusion, NMR and calorimetric techniques can provide valuable information regarding energy flow and ice formation during freezing. In addition, these methods may provide a basis for process monitoring systems. Present work in this lab is focused on developing NMR sensors for monitoring freezing progress in-line.

REFERENCES

ASHRAE. 1993a. Thermal properties of foods. Ch. 30. In *1993 ASHRAE Handbook Fundamentals*, (R.A. Parsons, ed.). American Society of Heating, Refrigerating, and Air-Conditioning Engineers, Inc., Atlanta, GA.

CHARM, S.E. and MOODY, P. 1966. Bound water in haddock muscle. ASHRAE J. *8*, 39-42.

CLELAND, A.C. 1990. *Food Refrigeration Processes: Analysis, Design, and Simulation*. Elsevier Applied Science, London.

CLELAND, A.C. and EARLE, R.L. 1979. A comparison of methods for predicting the freezing times of cylindrical and spherical foodstuffs. J. Food Sci. *44*, 958-963.

CLELAND, A.C. and EARLE, R.L. 1984. Assessment of freezing time prediction methods. J. Food Sci. *49*. 1034–1042.

DE MICHELIS, A. and CALVELO, A. 1983. Freezing time predictions for brick and cylindrical-shaped foods. J. Food Sci. *48*, 909–913.

DICKERSON, R.W. 1968. Thermal properties of foods. Ch. 2. In *The Freezing Preservation of Foods*, 4th Ed., Vol. 2, (D.K. Tressler, W.B. Van Arsdel and M.J. Copley, eds.) pp. 26-51, Van Nostrand Reinhold/AVI, New York.

DUSINBERRE, G.M. 1949. *Numerical Analysis of Heat Transfer*. McGraw Hill, New York.

DUSINBERRE, G.M. 1962. *Heat Transfer Calculations by Finite Difference*. International Textbook Co., Scranton, PA.

FLEMING, A.K. 1969. Calorimetric properties of lamb and other meats. J. Food Technol. *4*, 199–215.

FLORES, E.S. and MASCHERONI, R.H. 1988. Determination of heat transfer coefficents for continuous belt freezers. J. Food Sci. *53*(6), 1872–1876.

FYFE, C.A., BURLINSON, N.E., KAO, P. and ISBELL, S. 1990. Nuclear magnetic resonance imaging of freezing/thawing phenomena of liquids in heterogeneous systems. In *Conference Proceedings: 31st Experimental Nuclear Magnetic Resonance Spectroscopy Conference*, p. 56. April 1-5, Asilomar Conference Center, Pacific Grove, CA.

HEIL, J.R., McCARTHY, M.J. and OZILGEN, M. 1992. Magnetic resonance imaging and modeling of water up-take into dry beans. Lebens. Wiess. u Technol. *25*, 280–285.

HELDMAN, D.R. and SINGH, R.P. 1981. Thermodynamics of food freezing, Ch. 4. In *Food Process Engineering*, 2nd Ed. Van Nostrand Reinhold/AVI, New York.

HUNG, Y.C. 1990. Prediction of cooling and freezing times. Food Tech. *44*(5), 137–153.

HUNG, Y.C. and THOMPSON, D.R. 1980. Freezing time prediction: a review. ASAE Tech. Paper 80-6501.

HUNG, Y.C. and THOMPSON, D.R. 1983. Freezing time prediction for slab shape foodstuffs by an improved analytical method. J. Food Sci. *48*, 555–560.

IIR. 1971. *Recommendations for the Processing and Handling of Frozen Foods*. 2nd Ed., Internat. Inst. of Refrig., Paris.

JU, J. 1994. The Relevance of Glassy States to Frozen Food Stability. M.S. Thesis, Agricultural Chemistry, University of California, Davis.

KERR, W.L., JIE, J. and REID, D.S. 1993. Enthalpy of frozen foods determined by differential compensated calorimetry. J. Food Sci. *58*(3), 675–679.

KERR, W.L., KAUTEN, R.J., McCARTHY, M.J. and REID, D.S. 1993b. Combined NMR imaging and calorimetric study of food freezing. 3rd Conference of Food Engineering, February 21-23, 1993, Chicago, Illinois.

KLUZA, F. and SPIESS, W.E.L. 1994. A comparative study of freezing time prediction for food products. In *Proceedings of the 6th International Congress on Engineering and Foods*, pp. 376–378, Blackie Academic and Professional, Glasgow.

MANNAPPERUMA, J.D. and SINGH, R.P. 1988. Prediction of freezing and thawing times of foods using a numerical method based on enthalpy formulation. J. Food Sci. *53*, 626–630.

MANNAPPERUMA, J.D. and SINGH, R.P. 1989. A computer aided method for the prediction of properties and freezing/thawing times of foods. J. Food Eng. *9*, 275–304.

McCARTHY, M.J. 1994. *Magnetic Resonance Imaging in Foods*. Chapman and Hall, New York.

McCARTHY, M.J., CHAROENREIN, S., HEIL, J.R. and REID, D.S. 1989. MRI measurements of frozen systems. In *Technical Innovations in Freezing and Refrigeration of Fruits and Vegetables* (D.S. Reid, ed.) pp. 237–241, Proceedings of the International Conference held at University of California, Davis, July 9-12. Issued by International Institute of Refrigeration, Paris.

McCARTHY, M.J. and KAUTEN, R.J. 1990. Magnetic resonance imaging applications in food research. Trends in Food Sci. and Technol. *1*(12), 134–139.

McCARTHY, M.J. and McCARTHY, K. 1994. Quantifying transport phenomena in food processing with nuclear magnetic resonance imaging. J. Sci. Food Agric. *65*, 257–270.

McCARTHY, M.J., PEREZ, E. and OZILGEN, M. 1991a. Model for transient moisture profiles of a drying apple slab using data obtained with magnetic resonance imaging. Biotechnol. Progress *7*, 540–543.

McCARTHY, M.J., CHAROENREIN, S., GERMAN, J.B., McCARTHY, K. L. and REID, D.S. 1991b. Phase volume measurements using magnetic resonance imaging. In *Water Relationships in Foods: Advances in the 1980s and Trends for the 1990s* (H. Levine and L. Slade, eds.) pp. 615–626, Volume 302 of Advances in Experimental Medicine and Biology. Plenum Press, New York.

MORRIS, P.G. 1986. *Nuclear Magnetic Resonance Imaging in Medicine and Biology*. Clarendon Press, Oxford.

PURWADARIA, H.K. and HELDMAN, D.R. 1982. A finite element model for prediction of freezing rates in food products with anomolous shapes. Trans. ASAE *25*, 827-832.

REID, D.S. 1983. Fundamental physicochemical aspects of freezing. Food Technol. *4*, 110-113.

REID, D.S. 1990. Optimizing the quality of frozen foods. Food Technol. *7*, 78–82.

REIDEL, L. 1951. The refrigerating effect required to freeze fruits and vegetables. Refrig. Eng. *59*, 670-673.

ROSE, M.E. 1960. A method for calculating solutions of parabolic equations with free boundary. Mathemat. Comput. *14*, 249–256.

SOLOMON, A. 1966. Some remarks on the Stefan problem. Mathemat. Comput. *20*, 347–360.

VOLLER, V. and CROSS, M. 1981. Accurate solutions of moving boundary problems using the enthalpy method. Int. J. Heat Mass Transfer *24*(3), 545–556.

VOLLER, V. and CROSS, M. 1985. Application of control volume enthalpy methods in solution of Stefan problems. In *Computation Techniques in Heat Transfer* (R.W. Lewis, K. Morgan, J.A. Johnson and R. Smith, eds.) Pineridge Press, Swansea, U.K.

PREDICTING THE COOLING TIME FOR IRREGULAR SHAPED FOOD PRODUCTS

NATALIE CARROLL

Department of 4-H Youth
Purdue University
West Lafayette, Indiana

RABI MOHTAR

Department of Biological and Agricultural Engineering
Purdue University
West Lafayette, Indiana

LARRY J. SEGERLIND[1]

Department of Agricultural Engineering
Michigan State University
East Lansing, Michigan 48824

Accepted for Publication December 12, 1995

ABSTRACT

A new method for calculating the cooling time for fresh fruits and vegetables and processed foods is presented. The method uses the truncated analytical solution of the governing partial differential equation to define a cooling curve with two parameters. One parameter is the lowest eigenvalue for the product. The second parameter is a constant multiplier similar to the one that occurs in the analytical solution. The lowest eigenvalue is evaluated using a finite element analysis. The multiplying constant is evaluated using a finite element solution in time. Cooling curves for a Rome apple and a Bartlett pear are presented and discussed.

INTRODUCTION

Cooling of a product is an important task in the food industry. The need for cooling includes fresh fruits and vegetables, the carcass of an animal after slaughter, and processed products in cans or jars. Cooling is usually accom-

[1]Corresponding Author

Journal of Food Process Engineering **19** (1996) 385–401. *All Rights Reserved.*

plished using forced air, hydrocooling or refrigerated room cooling. In each case, the heat moves to the surface by conduction and from the surface by convection. Heat loss by convection is dependent on the type of cooling process selected. The cooling time depends on whether the product is cooled individually or whether the product is stored in boxes or bulk bins. One engineering aspect of the cooling process is to predict the time required for a product to cool to its surrounding temperature. This calculation for food products is often complicated by irregular geometries. Cooling times are presently calculated by approximating the product as a slab, a cylinder or a spherical body because temperature response curves are available for these shapes (Singh and Heldman 1993).

The objective of this paper is to present a new procedure for estimating the cooling time for irregularly shaped food products. The method utilizes the irregular grid analysis capabilities of the finite element method to evaluate a pair of parameters that define a cooling curve for a product. The procedure for developing a cooling curve is presented using a pair of axisymmetric products, a Rome apple and a Bartlett pear.

REVIEW OF LITERATURE

Traditional methods to determine the time needed to cool agricultural products have used the Fourier equation for transient heat transfer. This equation is limited to homogeneous, isotropic substances with nice shapes such as slabs, cylinders and spheres. Heldman (1977) gives the infinite series solutions to the governing differential equation for the infinite slab, the infinite cylinder and a sphere and shows how to apply these solutions to solve heating and cooling problems. Singh and Heldman (1993) present the Fourier equation in one-dimension and solve heating and cooling problems using temperature response charts for the well defined shapes.

Smith *et al.* (1967) preformed a similitude study to develop a nomograph that could be used to predict the cooling time of anomalous shapes. They concluded that the ellipsoidal model was the most valid model and adapted well for replacing a large range of anomalous shapes for predictions in transient conduction heat transfer.

DeBaerdemaeker *et al.* (1977) used the finite element method to solve time dependent problems related to food materials. The temperature history was calculated for the heating of a cylindrical can, the heating of an infinite slab, the cooling of a pear, the cooking of a chicken leg and the cooking of a slice of ham that is turned over during the process. Predicted temperature histories were given for each case.

Misra and Young (1979) used the finite element method for a time dependent heat transfer problem, approximating apples as a spherical body. Their numerical results agreed well with an analytical solution and the authors

concluded that the finite element method gave a very good approximation for the transient heat transfer problem in a sphere.

Hayakawa and Succar (1982) used the finite element method to determine thermal response and moisture loss during cooling of fresh potatoes and tomatoes. The surface heat conductance and transpiration coefficient were found to strongly effect the thermal response and moisture loss of spherical produce.

Bazan *et al.* (1989) predicted the temperature response during room cooling of a confined bin of spherical fruit. Experimental results agreed well with simulation studies. These investigators determined that small temperature gradients exist inside the fruit during cooling.

Pan and Bhownik (1991) used the finite element method to predict the temperature distribution in individual mature green tomatoes during forced air cooling. The calculated results were within 1C of the experimental results when cooling the tomatoes from 20C to 12C.

Fraser and Otten (1992) studied the cooling of peaches in well-vented containers. They measured temperature values and compared the results to the analytical solution for a sphere composed of peach flesh. Cooling times were slower for the peaches than predicted by the model. Fraser and Otten believed the slower cooling occurred because of the increase in air temperature as it flowed through the packed bed of peaches.

BASIC THEORY

The procedure for defining a cooling curve presented here starts with the well known Fourier equation for transient heat transfer. The idea can be illustrated by using the analytical solution to

$$\frac{\partial^2 T}{\partial x^2} = \frac{1}{a}\frac{\partial T}{\partial t} \tag{1}$$

for an insulated bar of unit length with the initial conditions of $T(x,0) = T_i$, boundary conditions of $T(0,t) = T(1,t) = T_\infty$ where T_∞ is a specified value. The parameters in (1) are the temperature, T, the time, t, the coordinate variable, x, and the thermal diffusivity, a. The units for temperature, time and space must be consistent with the units for the thermal diffusivity. The analytical solution of (1) for initial and boundary conditions similar to those given above is presented by several authors. A modification of the solution given by Smith (1978) is used here. The modification includes the dimensionless temperature ratio, (DTR)

$$DTR = \frac{T - T_\infty}{T_i - T_\infty} \tag{2}$$

and the thermal diffusivity, a. Most authors present the solution to (1) for the case where $a = 1$, $T_i = 1$ and $T_\infty = 0$.

The general solution to (1) is

$$DTR = \frac{4}{\pi} \sum_{n=0}^{\infty} \frac{1}{(2n+1)} [\sin(2n+1)\pi x]\exp[-(2n+1)^2 a\pi^2 t] \tag{3}$$

The slowest point to cool occurs at the center of the bar, $x = 1/2$.

Substituting $x = 1/2$ reduces (3) to

$$DTR = \frac{4}{\pi} \sum_{n=0}^{\infty} (-1)^n \frac{e^{-\beta_n t}}{(2n+1)} \tag{4}$$

where the sequence of numbers

$$\beta_n = (2n+1)^2 \pi^2 a \tag{5}$$

are called eigenvalues. The specific equations for a sequence of eigenvalues vary with the shape of the region, the boundary conditions and the material properties. Eigenvalues have units of s^{-1}.

The series in (4) can be simplified for two reasons. First, the cooling time for a product involves large values of time. Most of the exponential terms go to zero. Second, the eigenvalues are well spaced. The first three terms of (4) are

$$DTR = \frac{4}{\pi} \left(e^{-\beta_1 t} - \frac{1}{3} e^{-\beta_2 t} + \frac{1}{5} e^{-\beta_3 t} - \right) \tag{6}$$

where

$$\beta_1 = a\pi^2, \ \beta_2 = 9a\pi^2, \text{ and } \beta_3 = 25a\pi^2$$

The quantity $e^{-5} = 0.0067$ is negligible in the determination of the cooling time. When $\beta_2 t = 5$, which occurs when DTR = 0.73, the series in (4) reduces to

$$DTR = \frac{4}{\pi} e^{-\beta_1 t} \tag{7}$$

Every term in the series except the first disappears during the first 27% of the cooling process. The dimensionless temperature ratio can be represented by the two parameter equation

$$DTR = A\, e^{-\beta t} \tag{8}$$

The two parameters are the first or lowest eigenvalue, β, and a coefficient A.

The lowest eigenvalue in (8) can be determined from the system of ordinary differential equations generated by applying the finite element or finite difference method to (1). The parameter A varies with the dimension of the problem and the boundary conditions.

The derivation of (8) from (3) considered the one-dimensional step change problem. The analytical solutions for one-dimensional problems with convection boundary conditions and two- and three-dimensional problems are more complicated. Each solution, however, involves exponential terms and eigenvalues which are spaced such that the cooling process reduces to the solution of an equation similar to (8).

The value of the dimensionless temperature ratio at which all but the first term can be neglected is a function of the dimension and the boundary conditions. Calculations for one- and two-dimensional problems and cylindrical problems (not presented here) indicate that more than 50% of the cooling process is governed by an equation similar to (8) for the least favorable conditions. This fact is verified by observing the temperature response curves (Lienhard 1981; Singh and Heldman 1993). The straight line property of the curves on a semi-log plot indicate that only one term is left in the infinite series solution. Analysis of the temperature response curves indicates that the lowest starting point for the straight line relationship occurs for the cylindrical problem and starts with DTR = 0.65.

EVALUATION OF THE LOWEST EIGENVALUE

One reason a method similar to the procedure presented here has not been used is the difficulty involved in calculating the lowest eigenvalue for food

products with irregular shapes. Analytical evaluations of the lowest eigenvalue are not possible. The evaluation of β must be done numerically and requires a significant amount of computer software.

Application of the finite element or finite difference method to time dependent heat transfer problems defined by (1) produces a system of ordinary differential equations

$$[C] \{\frac{dT}{dt}\} + [K] \{T\} - \{F\} = \{0\} \tag{9}$$

where [C] is the capacitance matrix, [K] is the stiffness or conductance matrix and {F} is a vector that contains a part of the convection boundary condition and point source or sink values. The details of the finite element formulation for (9) are given by Segerlind (1984). The analytical solution of (9) requires the evaluation of a set of eigenvalues that satisfy the relationship

$$([K] - \beta_n [C]) \{T\} = \{0\} \tag{10}$$

In this case, n is finite and corresponds to the number of nodes at which the temperature is not known.

An excellent discussion of the solution of (10) is given by Bathe and Wilson (1976). Equation 10 can be solved for all of the eigenvalues using one of several methods. Jacobi's method and Householder's method are two of these. Alternatively, (10) can be solved for the lowest eigenvalue or the largest eigenvalue using the inverse iteration method or forward iteration method, respectively. The most important concept, however, is that the lowest eigenvalue for (10) approaches the value of the lowest eigenvalue for the analytical solution of (1).

The evaluation of the lowest eigenvalue, β, for the cooling problems presented in this paper used the finite element method to generate [C] and [K] in (9) and the inverse iteration method discussed by Bathe and Wilson (1976) to obtain β. The lowest eigenvalue for any problem has a fixed value and the value calculated from a finite element or finite difference grid will converge as the grid is refined. The amount of the grid refinement may affect the rate of convergence but should not influence its final value.

A complicating factor when using the finite element method to formulate (9) is that there are two ways to define the capacitance matrix [C]: The lumped formulation and the consistent formulation, Segerlind (1984). The lumped formulation produces a diagonal [C] and is similar to the finite difference formulation. The consistent formulation produces [C] with nonzero off-diagonal

values. Calculations reveal that the lumped formulation produces eigenvalues that converge to β from below while the consistent formulation produces values that converge to β from above, Hughes (1987). Hughes shows that an average of the values calculated using the two formulations gives an excellent estimate for the lowest eigenvalue when solving one-dimensional problems. Preliminary calculations done for this study indicated that the same property existed for axisymmetric problems. The average of the lowest eigenvalue calculated using the lumped and consistent formulations is very close to the analytical value for a finite cylinder with the temperature specified on the boundary. Preliminary calculations also showed that the grid should have a minimum of 16 nodes that are not a part of the boundary conditions in order to obtain an accurate value for β.

EVALUATION OF THE COEFFICIENT A

The simplified form of the cooling curve in (8) has a multiplying coefficient A. The value of A for the step change problem in (3) is $A = 4/\pi = 1.27$. The value changes with the boundary conditions and with the geometry of the problem. The cooling curves for a particular type of problem are not defined until A has been evaluated. The following procedure was used to evaluate A.

(1) Define the geometry for the shape and generate a finite element grid.
(2) Specify the boundary conditions which consist of known temperatures on the boundary or the convection heat loss condition. When convection heat loss occurs, the derivative boundary condition contains the ratio h/k where h is the convection coefficient, $W/m^2 \cdot °C$ and k is the thermal conductivity of the material, $W/m \cdot °C$.
(3) Evaluate the lowest eigenvalue using the inverse iteration method.
(4) Solve the transient heat transfer problem in time using the finite element method to generate the matrices in (9). A lumped formulation should be used for the capacitance matrix. Equation 9 is then solved using a central difference method in time because this method is second order accurate, Gear (1971). The advantages of the lumped formulation over the consistent formulation when developing (9) are discussed by Segerlind (1984). The selection of the time step required for an accurate solution using the central difference method is discussed by Mohtar (1994).
(5) Determine the time required for the dimensionless time ratio to decrease from one to a specified value. A value of 0.125 was used in this study. Equation (8) can be solved for the coefficient A from the time required to reach the specified dimensionless time ratio and the value of β.

The procedure outlined above must be performed for the shape of interest. The thermal diffusivity, a, and thermal conductivity, k, must be known for the material being cooled.

DETERMINATION OF THE COOLING EQUATIONS FOR A ROME APPLE AND A BARTLETT PEAR

Cooling curves were determined for two agricultural products, a Rome apple and a Bartlett pear. Each product was assumed to be axisymmetric. The cross section and the finite element grid for each are presented in Fig. 1. The Rome apple had a maximum horizontal diameter of 0.091m and a height of 0.067m. The Bartlett pear had a maximum horizontal diameter of 0.079m and a height of 0.107m. The thermal properties for an apple are given by Singh and Heldman (1993). The thermal properties for a pear are given by DeBaerdemaeker *et al.* (1977). A thermal diffusivity of a = 1.39E-07 m^2/sec and a thermal conductivity of k = 0.4 W/m·°C were used for the apple. A

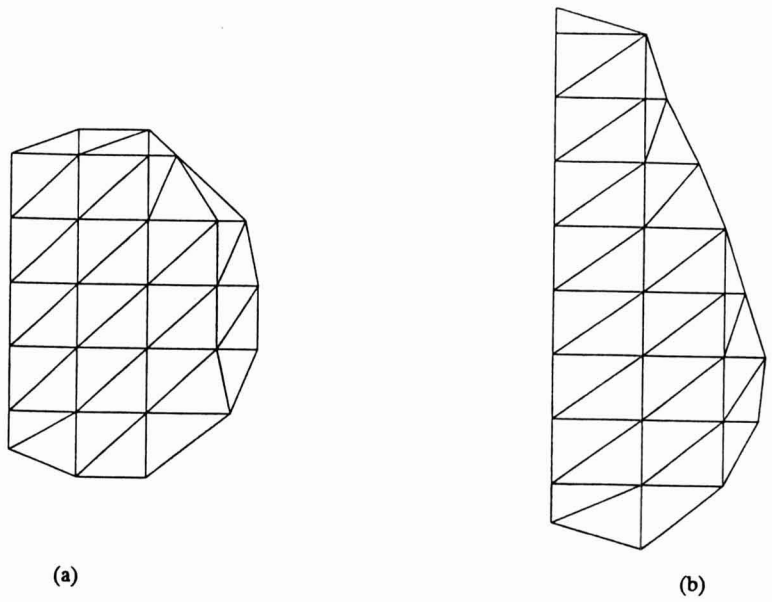

FIG. 1. THE FINITE ELEMENT GRIDS FOR (a) ROME APPLE AND (b) BARTLETT PEAR

thermal diffusivity of a = 1.65E-07 m^2/sec and a thermal conductivity of k = 0.6 W/m·°C were used for the pear.

The lowest eigenvalue and the coefficient A were evaluated for nine different values of h/k for each product. The lowest value of 10 is in the range for cooling by natural convection. Using the values given by Fraser and Otten (1992) and Leinhard (1981), h for natural convection is in the range of 5 or 6 $W/m^2 \cdot °C$. Using h = 5, h/k = 5/0.4 = 12.5 m^{-1} for the apple and h/k = 8.33 m^{-1} for the pear. The largest value of h/k = ∞ occurs when the temperature on the boundary is known.

The calculated values for the lowest eigenvalue and the A coefficient are summarized in Tables 1 and 2 for the apple and pear, respectively. The values in this table can be used in (8) to provide an explicit equation for the cooling process. The values can also be used to generate product specific cooling curves that allow a graphical solution. The variation of the lowest eigenvalue with h/k is presented in Fig. 2. The cooling curves for the apple and pear are given in Fig. 3 and 4, respectively.

The temperature response curves (Singh and Heldman 1993) are presented using a Biot number as one of the dimensionless parameters. The Biot number is Bi = hD/k where D is a characteristic length. The results in Table 1 and 2 are presented in terms of h/k and a Biot number calculated using the largest radius value for each product as D. The primary reason for presenting the Biot values is to allow researchers familiar with the Biot number a basis on which to evaluate the results. The calculations presented in the next section use the h/k values when interpolating to determine β and A. The definition of a characteristic length for an irregular shaped food product could be useful and should be studied.

TABLE 1.
COOLING PARAMETERS FOR A ROME APPLE

$\frac{h}{k}, \frac{1}{m}$	Biot Number	β	A
10	0.455	0.212E-04	1.01
25	1.14	0.508E-04	1.05
50	2.28	0.952E-04	1.09
125	5.69	2.030E-04	1.23
250	11.4	3.280E-04	1.43
625	28.4	5.140E-04	1.76
1250	56.9	6.500E-04	1.94
∞	∞	7.550E-04	2.06

TABLE 2.
COOLING PARAMETERS FOR A BARTLETT PEAR

$\frac{h}{k}, \frac{1}{m}$	Biot Number	β	A
10	0.395	0.457E-04	1.05
25	0.988	1.061E-04	1.10
50	1.98	1.918E-04	1.19
125	4.94	3.790E-04	1.37
250	9.88	5.600E-04	1.57
625	24.7	7.650E-04	1.77
1250	49.4	8.580E-04	1.83
∞	∞	9.630E-04	1.87

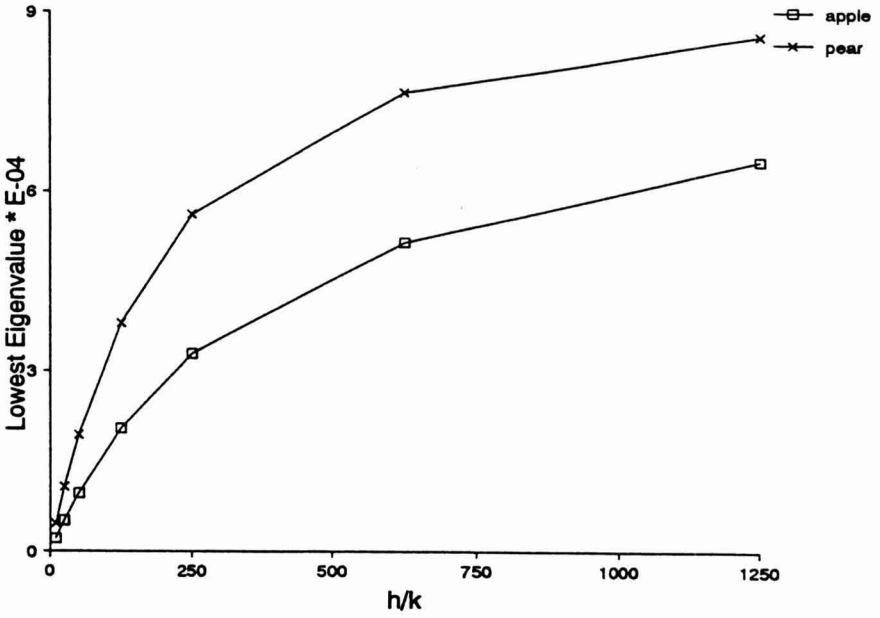

FIG. 2. THE LOWEST EIGENVALUE FOR A ROME APPLE AND A BARTLETT PEAR

EXAMPLE PROBLEM

A Bartlett pear of the size in this study (0.107 m height, 0.079 m in diameter) is being cooled from 20C to 2C using forced air with h = 25 $W/m^2 \cdot °C$. The thermal conductivity of the pear is k = 0.6 $W/m \cdot °C$. How long will it take for the pears to cool to 3°C. The dimensionless temperature ratio is

$$DTR = (3-2)/(20-2) = 0.056$$

The convection/conduction ratio is h/k = 25/0.6 = 41.67 m^{-1}. Linear interpolation of the values in Table 2 gives β = 1.63E-04 and A = 1.17. The equation for the cooling of the pears is

$$DTR = Ae^{-\beta t} = 1.17e^{-1.63E-04)t}$$

Since DTR = 0.056,

$$t = -\frac{\ln (DTR/A)}{\beta}$$

$$t = -\frac{\ln (0.056/1.17)}{1.63E-04}$$

$$t = 18650s = 5.18h$$

The cooling curve in Fig. 4 could have been used to solve this problem. The answer would have been subject to the visual interpolation errors that go with a graphical solution.

COMPARISON WITH STANDARD SHAPES

Given a method for defining the cooling equation for an irregular shaped food product, it is of interest to compare the cooling time using this equation with the time calculated using a standard shape such as the infinite slab, infinite cylinder or a sphere. A comparison of the cooling time for the Rome apple when modeled as a sphere and the cooling time for the Bartlett pear when modeled as an infinite cylinder is discussed here.

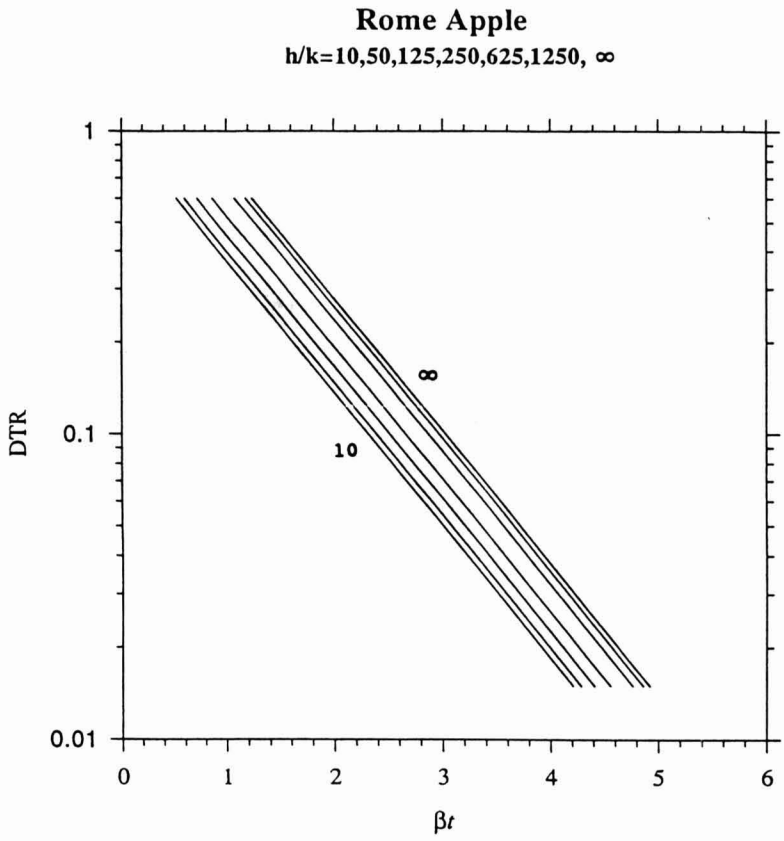

FIG. 3. COOLING CURVES FOR A ROME APPLE

The volume of the Rome apple and the Bartlett pear were calculated during the finite element formulation of (9). The volumes were 3.463E-04 m^3 and 3.043E-04 m^3 for the apple and pear, respectively. A sphere with the same volume as the apple has a radius of 0.0436m. A finite cylinder of height 0.107m with the same volume as the pear has a radius of 0.0301m.

The temperature response curves given by Singh and Heldman (1993), and other books, require a significant amount of visual interpolation unless values are selected on the basis of readability. Easily readable values were selected for this part of the study. The curves are given in terms of the dimensionless temperature ratio, DTR, the inverse of the Biot number and the dimensionless parameter, at/D^2 where D is the outside radius. A dimensionless temperature ratio of 0.100 was used. Inverse Biot values of 0, 0.5 and 1.0 were used for the apple and 0, 0.4 and 1.0 were used for the pear because the curves for these

values intercepted the DTR value of 0.100 at locations which reduced the amount of visual interpolation required.

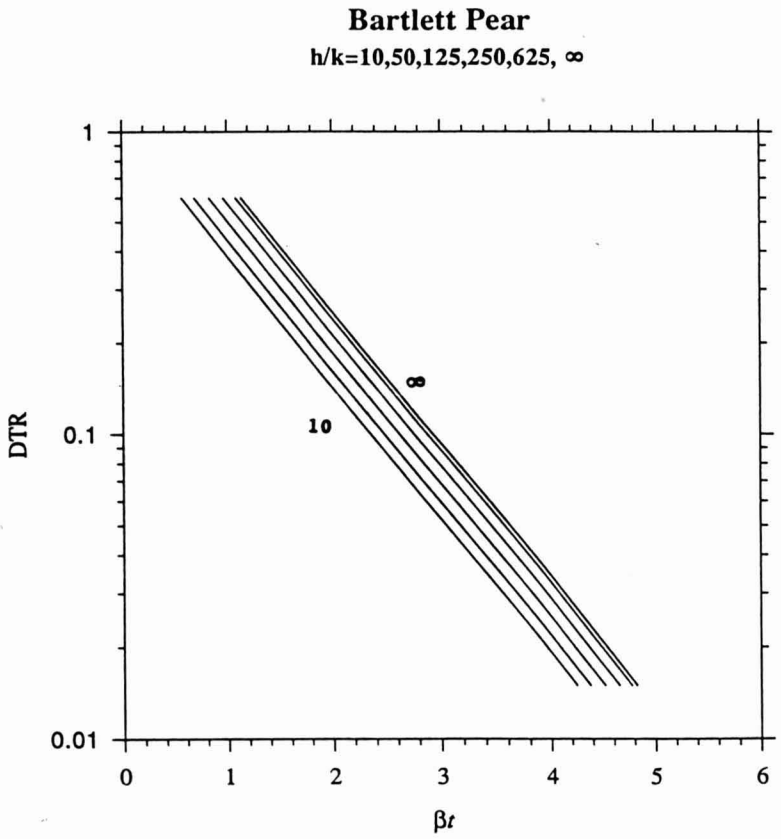

FIG. 4. COOLING CURVES FOR A BARTLETT PEAR

The time to cool each product to DTR = 0.100 was calculated using the finite element solution of (9) as described in step 4 to evaluate the coefficient A. The cooling time was also calculated using the numerical value of at/D^2 obtained from the temperature response curves. The results of each set of calculations are summarized in Tables 3 and 4.

TABLE 3.
COOLING TIME TO DTR = 0.100
USING TWO DIFFERENT METHODS, ROME APPLE

Type of Calculation	Bi^{-1} 0	0.5	1.0
Temperature Response Curve	4790	9436	14360
Numerical Analysis	3220	27000	50000

Calculated values are in seconds

TABLE 4.
COOLING TIME TO DTR = 0.100
USING TWO DIFFERENT METHODS, BARTLETT PEAR

Type of Calculation	Bi^{-1} 0	0.4	1.0
Temperature Response Curve	2730	4360	8720
Numerical Analysis	3060	8770	17700

Calculate values are in seconds

The conclusion of this comparison is that there is no relationship between the two methods of calculating the cooling values. In fact, the disparities between the calculated cooling times are so great, the finite element code was rechecked for programming errors and rechecked using a finite cylindrical shape. No errors were found in the software. It appears from these calculations that an apple should not be modeled by a sphere nor should a pear be modeled by an infinite cylinder when trying to estimate the time to cool to a specified temperature. These results may not be as surprising as they seem because the cooling of an apple or pear is a special two-dimensional problem, axisymmetric, and the infinite slab, the infinite cylinder and a sphere are one-dimensional problems.

COOLING TIME ESTIMATE

Equation (8) and the A values for the apple and pear can be used to generate a simple equation to estimate the cooling time. The equation contains a numerical value divided by the lowest eigenvalue. The equation has the simple form

$$t = \frac{C}{\beta} \tag{11}$$

The cooling time to a specified DTR value is

$$t = -\frac{\ln (DTR/A)}{\beta} \tag{12}$$

The numerator in (12) has similar values for apples and pears for the same h/k values. Suppose h/k = 125 m^{-1} and DTR = 0.02. The corresponding A values are 1.23 and 1.37 for the apple and pear, respectively. The numerator values are 1.789 and 1.836 with an average of 1.81. The time required to cool the apple or pear is

$$t = \frac{1.81}{\beta} \tag{13}$$

Using the eigenvalue for each fruit when h/k = 125 m^{-1} in (12), the estimated time to cool each fruit 98% is 8920 s for the apple and 4780 s for the pear. These values compare with 8810 s, apple, and 4840 s, pear, calculated using (8). The cooling time for each fruit has a 1.2% error. The largest time difference is less than 2 min.

Table 5 contains the C values required for (11) for six different DTR values and convection coefficients corresponding to natural convection, h = 5 $W/m^2°C$, forced convection, h = 25 $W/m^2°C$, and hydrocooling, h = 70 $W/m^2°C$. The convection coefficients are given by Fraser and Otten (1992). The C coefficients were calculated using the A values given in Table 5. Each A value was determined using linear interpolation in Table 2 or Table 3 and is the average for the apple and the pear.

The advantage of the cooling time estimate given by (13) is that the lowest eigenvalue is much easier to evaluate than a time dependent finite difference or finite element solution of the fruit. No decisions have to be made about the solution procedure or the time step. A good estimate of the lowest eigenvalue, β, is obtained from a relatively coarse grid of the shape. The best approach is to average the lowest eigenvalue for the lumped and consistent formulations of the time problem. The C values may also be relatively independent of the axisymmetric shape. Further study is needed on this aspect.

TABLE 5.
THE COEFFICIENT C USED TO ESTIMATE THE TIME REQUIRED TO COOL A ROME APPLE AND A BARTLETT PEAR

Type of Cooling	A	DTR 0.125	0.100	0.075	0.050	0.025	0.010
Natural	1.03	0.916	1.01	1.14	1.30	1.61	2.04
Forced	1.14	0.960	1.06	1.18	1.36	1.66	2.06
Hydro	1.33	1.03	1.12	1.25	1.42	1.72	2.12

SUMMARY

A procedure for developing a cooling equation for an irregular shaped food product has been presented. The cooling equation includes two parameters that are a function of the product shape, material properties and boundary conditions. The procedure utilizes the finite element method to calculate the lowest eigenvalue for the transient heat transfer problem. The second parameter is obtained by determining the time required for the dimensionless temperature ratio to reach a specified value. The method was applied to the cooling of an apple and a pear. A table of the lowest eigenvalues and the multiplying coefficient A as a function of h/k is given for the Rome apple and the Bartlett pear, respectively. The method gives reasonable cooling time values for the two products analyzed. A comparison with temperature response curves indicates that the calculations for an apple modeled using a sphere with the same volume are not comparable. The same noncomparble result was found for the pear when it was modeled using a finite cylinder with the same volume.

The method of analysis presented here could be the basis for a computer code that is capable of determining the cooling time for axisymmetric shapes because the cooling time can be represented by a single numerical coefficient divided by the lowest eigenvalue for the product being cooled. All of the thermal properties of the cooling problem are incorporated in the lowest eigenvalue. The lowest eigenvalue is a more desirable parameter than the Biot number because the Biot number is not clearly defined for irregular geometries. The computer software would ask for information that defines the shape and thermal properties, calculate the lowest eigenvalue for the product and give the time to cool the product to a specified dimensionless temperature ratio.

REFERENCES

BATHE, K.-J. and WILSON, E.L. 1976. *Numerical Methods in Finite Element Analysis*. Prentice-Hall Inc. Englewood Cliffs, New Jersey.

BAZAN, T., CHAU, K.V and BAIRD, C.D. 1989. Heat Transfer Simulation of the Bulk Cooling of Fruits. Paper No. 89-6559, ASAE, St. Joseph, MI.

DeBAERDEMAEKER, J., SINGH, R.P. and SEGERLIND, L.J. 1977. Modelling heat transfer in foods using the finite-element method. J. Food Process Engineering *1*, 37–50.

FRASER, H. and OTTEN, L. 1992. Predicting 7/8 Cooling Times for Peaches by Comparing Heat Transfer Modelling and Field Measurements Methods. Paper No. 92-6016. ASAE. St. Joseph, MI.

GEAR, C.W. 1971. *Numerical Initial Value Problems In Ordinary Differential Equations*. Prentice-Hall. Englewood Cliffs, NJ.

HAYAKAWA, K.-I. and SUCCAR, J. 1982. Heat Transfer and Moisture Loss of Spherical Fresh Produce. J of Food Sci. *47*(2), 596.

HELDMAN, D.R. 1977. *Food Process Engineering*. Van Nostrand Reinhold/ AVI New York.

HUGHES, T.J.R. 1987. *The Finite Element Method*. Prentice-Hall, Englewood Cliffs, New Jersey.

LIENHARD, J.H. 1981. *A Heat Transfer Book*. Prentice-Hall, Englewood Cliffs, New Jersey.

MISRA, R.N. and YOUNG, J.H. 1979. The finite element approach for solution of transient heat transfer in a sphere. Trans. of the ASAE. *22*(4), 944–949.

MOHTAR, RABI HASSAN. 1994. Dynamic Time Step Estimates For Transient Field Problems. Unpublished Ph.D. Dissertation. Michigan State University.

PAN, J.C. and BHOWMIK, S.R. 1991. The finite element analysis of transient heat transfer in fresh tomatoes during cooling. Trans. of ASAE, *34*, 972–976.

SEGERLIND, L.J. 1984. Applied finite element analysis. 2nd Ed. John Wiley & Sons, New York.

SINGH, R.P. and HELDMAN, D.R. 1993. *Introduction to Food Engineering*, 2nd Ed. Academic Press, San Diego, CA.

SMITH, G.D. 1978. *Numerical Solution of Partial Differential Equations: Finite Difference Methods*. 2nd Ed. Clarendon Press, Oxford.

SMITH, R.E., NELSON, G.L. and HENRICKSON, R.L. 1967. Analyses on Transient Heat Transfer form Anomalous Shapes. Trans of ASAE, 10, 236–245.

PARTICLE HEAT TRANSFER COEFFICIENTS UNDER VARIOUS RETORT OPERATING CONDITIONS WITH END-OVER-END ROTATION

S.S. SABLANI and H.S. RAMASWAMY[1]

Department of Food Science and Agricultural Chemistry
Macdonald Campus of McGill University
Ste Anne-de-Bellevue, PQ H9X 3V9, Canada

Accepted for Publication December 12, 1995

ABSTRACT

Forced convection heat transfer in cans was studied experimentally during end-over-end sterilization in a full-immersion, hot-water rotary sterilizer. A polypropylene spherical particle (diameter = 19 mm) was suspended in a high temperature bath oil (Newtonian liquid) using a flexible fine-wire thermocouple attached to the can wall providing uninhibited heat transfer conditions. The overall heat transfer coefficient, U, was determined using a lumped capacity heat balance approach and the fluid-to-particle heat transfer coefficient, h_{fp}, was determined from transient temperature data at the center of the particle using a finite difference computer simulation. The effects of retort temperature (110 to 130C), rotational speed (0 to 20 rpm), radius of rotation (0 to 27 cm) and can headspace (6.4 and 10 mm) were examined on the associated heat transfer coefficients. Higher heat transfer coefficients were obtained with increasing values of all four variables, and the effects of rotational speed and headspace were more significant than those of retort temperature and radius of rotation. U values ranged from 120 to 187 $W/m^2.K$ and h_{fp} values ranged from 23 to 145 $W/m^2.K$ depending on the operating conditions.

INTRODUCTION

Mathematical modelling of heat sterilization of canned liquids with suspended food particles in rotary autoclaves requires data on (1) thermo-physical properties of both liquids and solid food particles and (2) associated heat transfer coefficients. In such systems, both the overall heat transfer coefficient, U, and the fluid-to-particle heat transfer coefficient, h_{fp}, are needed to predict heat transferred to solid food particles. Little information is available on h_{fp} in cans during agitation processing due to difficulties in monitoring the transient temperature of freely moving particles. Earlier studies reported h_{fp} values

[1]Corresponding Author

Journal of Food Process Engineering **19** (1996) 403–424. *All Rights Reserved.*

between a stationary particle, fixed on to a rigid thermocouple, and fluid moving around it (Lenz and Lund 1978; Sastry 1984; Fernandez *et al.* 1988 and Deniston *et al.* 1987). Recently, efforts have been made to measure h_{fp} while allowing some particle movement inside the can during agitation sterilization (Stoforos and Merson 1990 and 1991; Weng *et al.* 1992; Sablani and Ramaswamy 1995). Mechanical agitation of cans in rotary autoclaves enhances heat transfer rates to both fluid and particle, and has the potential to improve the quality retention compared with those foods processed in still autoclaves. However, there is a need to quantify the effect of agitation and other parameters influencing U and h_{fp}. Several studies have been published on liquid foods thereby evaluating the effect of various parameters on U, and these have been presented in a review article by Rao and Anantheswaran (1988). Some studies on convective heat transfer in the presence of particles have focused only on the liquid portion of the canned food, thus determining the effects of various parameters on heat transfer rates to liquid (Berry *et al.* 1979; Berry and Bradshaw 1980, 1982; Berry and Dickerson 1981).

The effect of various parameters, e.g. process temperature, rotational speed, fluid viscosity, particle properties and volume fraction occupied by the particles etc., on h_{fp} have been experimentally investigated by Lenz and Lund (1978), Sastry (1984), Deniston *et al.* (1987) and Fernandez *et al.* (1988). In these studies, motion of the experimental particle was completely restricted by a rigid thermocouple, used for temperature measurement at the particle center. Since the relative velocity between particle and fluid influences h_{fp}, its magnitude is expected to be different when the particle is free to move. Stoforos and Merson (1992) investigated the effect of fluid viscosity, particle properties and rotational speed on h_{fp} and U in axially rotating cans by measuring the surface temperature using liquid crystals as the particles moved freely in the cans during agitation. However, the liquid crystals used in the study covered only a narrow temperature range (26 to 50C), and the simulated food particles (teflon and aluminum) were of high density. Naveh and Kopelman (1980) studied the effect of mode of agitation on overall heat transfer coefficient and found that U was improved by two to three times in end-over-end agitation compared to axial mode of rotation.

Recently, Sablani and Ramaswamy (1995) developed a method to measure the convective heat transfer coefficients in cans during agitation processing using a flexible thermocouple technique. In that study, particle transient temperatures were measured at the center using a flexible fine-wire thermocouple allowing sufficient particle motion during processing for providing a more realistic data on associated h_{fp} values. The objective of this study was to use this flexible thermocouple approach for quantifying the effect of system parameters, such as retort temperature, rotational speed, radius of rotation and can headspace on U and h_{fp}, during end-over-end sterilization.

MATHEMATICAL FORMULATION

The overall thermal energy balance on a particulate-liquid food system can be used to calculate associated convective heat transfer coefficients. The governing equation for heat transfer in such systems can be written as (Deniston *et al.* 1987) (all symbols are detailed in nomenclature):

$$U.A_c.(T_R-T_f)=m_f.C_{pf}.\frac{dT_f}{dt}+m_p.C_{pp}.\frac{d<T_p>}{dt} \quad (1)$$

The following are assumed for deriving Eq. (1): uniform initial temperature for the particle, uniform initial and transient temperatures for liquid, constant heat transfer coefficients, constant physical and thermal properties for both fluid and particles, and no energy accumulation in can wall.

The second term on the right side of Eq. (1) is equal to the heat transferred to particles from the liquid across the particle surface:

$$m_p.C_{pp}.\frac{d<T_p>}{dt}=h_{fp}.A_p.(T_f-T_{ps}) \quad (2)$$

The heat flow in a spherical particle immersed in fluid can be described by the following partial differential equation (Ozisik 1985)

$$\frac{\partial T}{\partial dt}=\alpha_p.(\frac{\partial^2 T}{\partial r^2}+\frac{2}{r}.\frac{\partial T}{\partial r}) \quad (3)$$

The initial and boundary conditions are:

$$T(r,0)=T_i \qquad \text{at } t=0 \quad (4)$$

$$\frac{\partial T(r,t)}{\partial dr}=0 \qquad \text{at } r=0 \quad (5)$$

$$k_p.\frac{\partial T}{\partial dr}=h_{fp}.(T_f-T_{ps}) \qquad \text{at } r=a \quad (6)$$

MATERIALS AND METHODS

A high temperature bath oil (100 CST at 38C, Fisher Scientific Ltd., Montreal, PQ) and polypropylene spheres (Small Parts Inc., Miami, FL) of

diameter 19 mm were used as model liquid and particle, respectively. Thermo-physical properties for the liquid and particle were determined and summarized in Table 1. The density of polypropylene sphere was obtained from the volume of water displaced by the spheres and their weight; specific heat was measured using a calorimetric method. Thermal diffusivity of polypropylene sphere was evaluated using the heating rate index method by heating it in a steam cabinet (Singh 1982). Thermal conductivity of particle was back calculated from measured values of thermal diffusivity, density and specific heat. Oil density was obtained by measuring the volume using Pycnometer and weight of the oil. Heat capacity of oil was measured by comparing the heating rates of equal masses of oil and water for same power input. Thermal conductivity of oil was measured using a conductivity probe (Ramaswamy and Tung 1981).

TABLE 1.
THERMO-PHYSICAL PROPERTIES OF TEST MATERIALS

Material	Density kg/m^3	Heat Capacity kJ/kg.K	Thermal-conductivity W/m.K	Thermal-diffusivity m^2/s	Kinematic-viscosity m^2/s
Polypropylene	830	1.84	0.359	2.35×10^{-7}	-
Oil	880	2.21	0.165	0.85×10^{-7}	10^{-4}

Can liquid temperature was measured at the geometric center of the cans using CNS copper-constantan needle type thermocouples (Locking connector, C-10, Ecklund Harrison Technologies, Inc., Cape Coral, FL). For the purpose of measuring particle transient temperatures, a fine hole was drilled to the center of the spherical particle which was filled with a 50%:50% mixture of epoxy resin and hardener, and a fine-wire (0.0762 mm diameter) copper-constantan thermocouple was inserted to the center. In this way, the trapping of air along the channel was minimized. The thermocouple equipped particle was mounted inside the can using a brass connector (stuffing box for plastic pouches C-5.2, Ecklund Harrison Technologies, Inc., Cape Coral, FL) at half height of the can. The length of the thermocouple wire inside the can was kept approximately equal to half height of the can for allowing the particle movement inside the can. The thermocouples for test cans were passed through a 32- circuit slip-ring attached to the retort and connected to a data acquisition system [μ-MEGA 1050 remote intelligent measurement and control system (OM-1050), two 16-channel thermocouple/low level voltage expander board (OMX-STB-TC) and a 5-V battery pack; all from Omega Engineering Corp., Stamford, CT]. Thermocouple signals were recorded at 15 s time intervals using LABTECH NOTEBOOK (Laboratory Technologies Corporation, Wilmington, MA).

Cans of size 307 × 409 containing the high temperature bath oil and thermocouple equipped particle were processed in a batch type, rotary, full-immersion, hot-water sterilizer (Stock Rotomat-PR 900; Hermann Stock Maschinenfabrick, Germany). Only one particle per can was used. In each test run, four test cans were placed equidistant from the horizontal central axis of the rotating cage, in a vertical orientation, to give end-over-end rotation. The remaining space in the cage was filled with dummy cans containing water. Three retort temperatures (110, 120 and 130C), four rotational speeds (0, 10, 15 and 20 rpm), four radii of rotation (0, 9, 19 and 27 cm) and two can headspaces (6.4 and 10 mm) were employed as system (operating) variables. In the first set of experiments, a 3 × 3 × 4 full-factorial design was employed with the three retort temperatures, three rotational speeds (10, 15 and 20 rpm) and the four radii of rotations with a can headspace of 10 mm. In order to study the effect of can headspace, a 3 × 3 × 2 full-factorial design was used with the three retort temperatures, the three rotational speeds (10, 15 and 20) and the two can headspaces at a constant radius of rotation of 19 cm. Experiments were also carried out at 0 rpm (still retort processing condition) at the three retort temperatures. All of the processing conditions were repeated twice.

In order to verify the temperature uniformity in cans during the processing (a fundamental assumption in deriving the thermal energy balance on the can), needle type thermocouples of different lengths (#L1 = 42 mm, #L2 = 33 mm and #L3 = 21 mm) were mounted on each of two cans of size 307 × 409 at different heights (#H1 = 20 mm, #H2 = 56 mm and #H3 = 85 mm, from bottom of the can). These cans were processed at rotational speeds of 0, 10, 15 and 20 rpm at 120C.

Data Analysis

In each experiment, the heating time was kept sufficiently long such that the liquid and particle temperatures equilibrated to the heating medium temperature. The equilibrated liquid and particle temperatures were corrected to match the heating medium temperature. Temperature data were discarded if thermocouple breakage occurred during runs (about 15% of test cans suffered thermocouple breakages due to the use of fine wire thermocouples). The liquid and particle temperatures were recorded at 15 s intervals; however, the numerical solution of transient heat transfer involving the spherical particle with convective boundary condition required much shorter time intervals for the desired accuracy. For this purpose, liquid temperature profiles were computed from the evaluated heat penetration parameters (f_h and j_{ch}) using the formula developed by Hayakawa (1977). The heat penetration parameters (f_h and j_{ch}) were calculated using unaccomplished liquid temperature ratio based on retort temperature. Effectiveness of the retort come up time which varied 2 to 4 min,

was considered to be ~85%, typical of logarithmic comeup profiles (Ramaswamy 1993). Calculated heating rate index was then used in Eq. (7) for the overall heat transfer coefficient determination. Particle temperatures were interpolated from measured values for the shorter time intervals.

Since only one particle was used in each can, the amount of heat absorbed by the particle was small and considered negligible as compared to the heat absorbed by the liquid. Overall heat transfer coefficients (U) were calculated from the heating rate index for can fluid, $f_{h,f}$, mass of fluid, m_f, heat capacity of fluid, C_{pf} and total can surface area, A_c, using the following equation:

$$U = \frac{2.303 m_f \cdot C_{pf}}{(f_{h,f} \cdot A_c)} \tag{7}$$

The fluid-to-particle heat transfer coefficients (h_{fp}) were determined by solving the governing partial differential equation of conduction heat transfer in spherical co-ordinates with associated initial and boundary conditions using a finite difference method. The inverse heat conduction approach, where surface heat flux is estimated using one or more measured temperatures histories inside a heat-conducting body, was used to estimate h_{fp} values (Sablani and Ramaswamy 1995). Two different approaches were used to determine the fluid to particle heat transfer coefficient (h_{fp}). In the first approach (Lenz and Lund 1978), the h_{fp} value was obtained as the limiting value of heat transfer coefficient that minimizes the sum the of square of the difference between experimental and predicted temperatures (LSTD), and in the second approach (Weng *et al.* 1992), it is taken as the limiting value of heat transfer coefficient that minimizes the difference between the measured and predicted lethality (LALD). A computer program developed to solve a set of finite difference equations could incorporate either of the approaches. The difference between measured and calculated lethality at the particle center (slowest heating point in liquid/particulate system), F_o, was finally used as an objective function (LALD approach) due to its relevance to thermal processing. The procedure involved initially comparing the calculated and measured lethality (or temperatures) at the center of the particle based on an assumed h_{fp} value, and then subsequently changing h_{fp}, in a sequential pattern, until the calculated and measured lethality values (Eq. 8) matched a fixed value of 10 min.

$$F_o = \int_0^t 10^{\frac{(T-121.1)}{10}} dt \tag{8}$$

Overall heat transfer coefficient and fluid-to-particle heat transfer coefficient data were analyzed by using Statistical Analysis System (SAS) software program available on McGill University (Montreal, PQ) mainframe computer. Analysis

of variance (ANOVA) procedure was used to detect the significance of retort temperature, rotational speed, radius of rotation and can headspace and other combined effects. In order to estimate uncertainties in the calculated h_{fp} values, an error analysis was performed with respect to thermocouple location, particle thermal diffusivity and particle size. A thermocouple misplacement of 1.9 mm (20% of particle radius) from the particle center was taken as the maximum error with respect to thermocouple placement. The relative uncertainty in particle thermal diffusivity measurement was taken as $\pm$ 5%. Since particle thermal conductivity was calculated from the product of particle thermal diffusivity, density and heat capacity, the same amount of uncertainty ($\pm$5%) was considered with respect to particle thermal conductivity. Only $\pm$ 0.5% of uncertainty in particle size was considered since the particles were machine fabricated. The error analysis was carried out only with extreme conditions (lower range and higher range of values) of calculated h_{fp} values.

RESULTS AND DISCUSSION

Temperature Profiles and Temperature Uniformity

Typical time-temperature profiles of the retort heating medium, can fluid, particle center (experimental and predicted) are shown in Fig. 1a and c. For the lethality values of 10 min at the particle center, temperatures predicted at the particle center (LALD) were lower than the experimental temperatures in the beginning of the heating (below 90C); however, during later part of the heating (after 90C) the predicted temperature showed a better match with experimental temperatures. This is due to the nature of the objective function F_o used in the present case. The use of F_o as the objective function gave more weightage to temperatures higher than 90C due to its sensitivity to lethality. This is more evident from the accumulated lethality plot. Experimental lethality measured at the particle center had an excellent match with predicted lethality (Fig. 1b). When the measured and predicted temperature at the particle center was used an objective function (LSTD), the predicted fluid to particle heat transfer coefficients were found be considerably higher. This approach tends to overpredict the lethality as shown in Fig. 1d. Since this situation can potentially lead to underprocessing when employed for process design, the lethality approach was considered more appropriate and used for subsequent analyses.

Temperature uniformity in cans was measured in terms of heat penetration parameters, i.e., heating rate index, f_h and heating lag factor, j_{ch}. When the cans are processed in a still retort (0 rpm), the prevailing mode of heat transfer will be mostly natural convection. Hence, a large temperature gradient can be expected in cans. This was evident from the studies as shown in Table 2 with large location dependent differences in f_h, j_{ch} and t_1 values. The f_h value for

location No. 1 (bottom center) was nearly twice as compared to location No. 3 which was at the top corner (85 mm height from bottom) of the can. Temperature gradients for liquid inside the cans were virtually nonexistent during

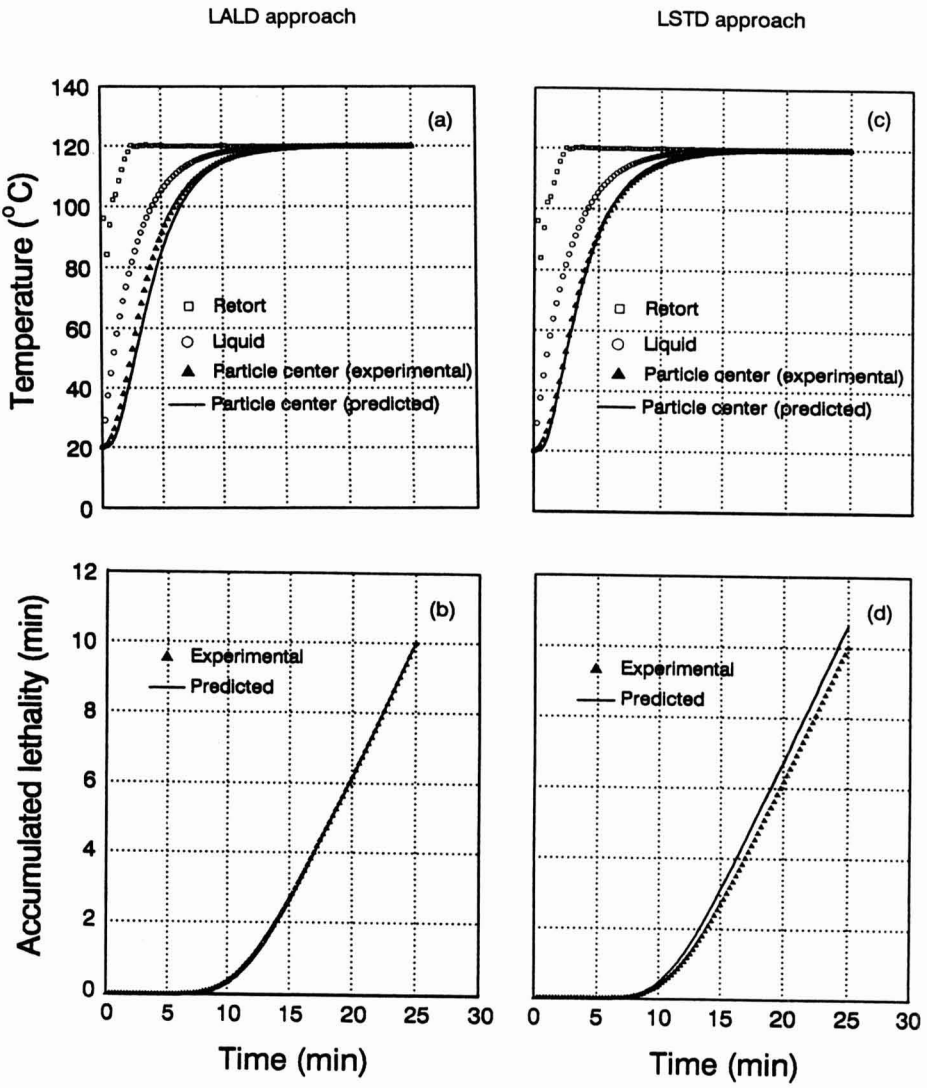

FIG. 1. TYPICAL EXPERIMENTAL AND PREDICTED TIME-TEMPERATURE PROFILES AND LETHALITY PLOTS FOR THE CAN PROCESSED AT 120C RETORT TEMPERATURE AND 15 RPM ROTATIONAL SPEED
[prediction was based on two approaches: Least squared temperature difference (LSTD) and least absolute lethality difference (LALD)]

TABLE 2.
TEMPERATURE UNIFORMITY OF LIQUID WITHIN THE CAN PROCESSED AT RETORT TEMPERATURE OF 120C AND FOUR ROTATIONAL SPEEDS

Rotational Speed (rpm)	Location 1			Location 2			Location 3			CV (%)	
	f_h	j_{ch}	t_l	f_h	j_{ch}	t_l	f_h	j_{ch}	t_l	f_h	j_{ch}
0	8.00	1.55	3.0	6.69	1.29	1.50	4.20	1.04	0.5	-	-
	8.03	1.63	3.0	6.71	1.41	1.50	4.17	1.01	0.5	-	-
10	7.91	1.01	0.5	7.94	1.03	0.5	7.91	1.06	0.5	0.18	1.99
	7.89	1.02	0.5	7.98	1.06	0.5	7.81	1.09	0.5	0.88	2.71
15	6.22	1.16	0.5	6.19	1.12	0.5	6.19	1.16	0.5	0.23	1.64
	6.22	1.10	0.5	6.29	1.14	0.5	6.13	1.20	0.5	1.05	3.58
20	4.83	1.21	0.5	4.92	1.14	0.5	4.88	1.16	0.5	0.76	2.5
	4.95	1.12	0.5	4.96	1.16	0.5	4.84	1.20	0.5	1.16	2.82

CV = Coefficient of variability (standard deviation/mean)

agitation processing. This was supported by the small differences in heat penetration parameters between different locations under 10-20 rpm. The gradual tightening of the temperature distribution under different test runs is shown as standard deviations in temperature with respect to time in Fig. 2. Stabilizing to within 0.5C standard deviation occurred within 5 min under agitation processing while it required about 20 min under still processing condition. An increase in rotational speed resulted in early stabilization resulting in uniform temperature within the can (Fig. 2.).

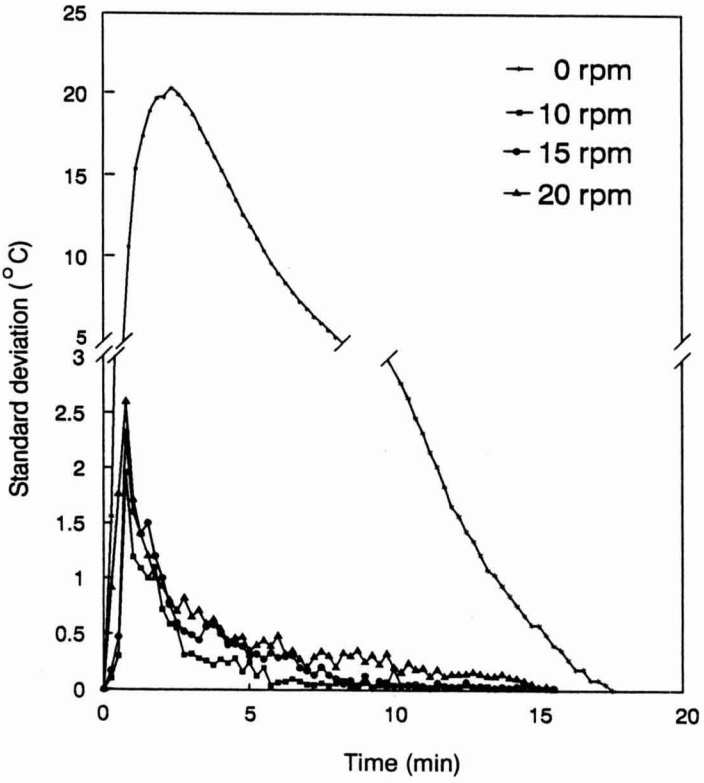

FIG. 2. STANDARD DEVIATIONS IN TEMPERATURES AS A FUNCTION OF HEATING TIME WITH RESPECT TO THREE THERMOCOUPLE LOCATIONS (42 & 20 mm; 33 & 56 mm; AND 21 & 85 mm, FROM THE CAN SURFACE AND BOTTOM, RESPECTIVELY) IN CANS SUBJECTED TO END-OVER-END PROCESSING AT VARIOUS ROTATIONAL SPEEDS (0 TO 20 RPM)

Overall Heat Transfer Coefficient (U)

Tables 3 and 4 summarize the overall heat transfer coefficients obtained under the different experimental conditions. U values varied from 120 to 187 $W/m^2.K$. Increasing the retort temperature improved the mean U value (6% increase from 110 to 130C) probably due to the lowering of fluid viscosity at higher retort temperature and probably creating more turbulence in fluid. The overall heat transfer coefficient also increased with the increasing rotational speed (38% increase in mean U value between 10 and 20 rpm), again possibly due to enhanced mixing resulting in a higher degree of turbulence. The influence of rotational speed on U was more pronounced than any other parameters under study. At 0 rpm (still report processing condition), the overall heat transfer

TABLE 3.
OVERALL HEAT TRANSFER COEFFICIENT, U, AS INFLUENCED BY RETORT TEMPERATURE, ROTATIONAL SPEED AND RADIUS OF ROTATION

Retort Temperature (°C)	Rotational Speed (rpm)	Radius of Rotation (cm)	U ($W/m^2 K$)
110	10	0	122.3 ± 0.9
		9	119.6 ± 0.1
		19	122.6 ± 0.0
		27	126.3 ± 2.6
	15	0	148.3 ± 0.4
		9	146.2 ± 3.2
		19	155.7 ± 2.4
		27	152.6 ± 0.6
	20	0	168.8 ± 0.5
		9	180.5 ± 1.6
		19	182.1 ± 1.7
		27	186.4 ± 2.2
120	10	0	132.7 ± 0.8
		9	134.7 ± 2.5
		19	138.4 ± 3.4
		27	135.3 ± 1.1
	15	0	154.3 ± 0.4
		9	154.2 ± 0.0
		19	160.7 ± 1.4
		27	161.9 ± 4.0
	20	0	178.5 ± 1.2
		9	180.8 ± 2.9
		19	185.3 ± 1.1
		27	188.1 ± 6.0
130	10	0	135.2 ± 0.4
		9	136.2 ± 1.4
		19	139.8 ± 0.6
		27	143.0 ± 4.7
	15	0	153.6 ± 1.4
		9	156.2 ± 1.2
		19	165.1 ± 0.8
		27	175.9 ± 1.5
	20	0	179.1 ± 4.0
		9	183.8 ± 2.6
		19	181.4 ± 1.0
		27	191.6 ± 1.9

TABLE 4.
OVERALL HEAT TRANSFER COEFFICIENT, U, AS INFLUENCED BY RETORT TEMPERATURE, ROTATIONAL SPEED AND HEADSPACE (mm)

Retort Temperature (°C)	Rotational Speed (rpm)	Headspace (cm)	U (W/m^2K)
110	0	6.4	120.9 ± 1.5
	10	6.4	121.5 ± 2.3
		10	122.6 ± 0.0
	15	6.4	135.2 ± 2.0
		10	155.7 ± 2.4
	20	6.4	146.7 ± 5.0
		10	182.1 ± 1.7
120	0	6.4	126.1 ± 1.3
	10	6.4	130.5 ± 1.5
		10	138.4 ± 3.4
	15	6.4	144.2 ± 3.4
		10	160.7 ± 1.4
	20	6.4	164.9 ± 7.9
		10	185.3 ± 1.1
130	0	6.4	130.8 ± 2.6
	10	6.4	133.5 ± 0.9
		10	139.8 ± 0.6
	15	6.4	145.6 ± 5.4
		10	165.1 ± 0.8
	20	6.4	158.7 ± 7.3
		10	181.4 ± 1.0

coefficient was calculated as for agitated processing conditions in which temperature uniformity of liquid within the can was achieved in a short time. Since temperature gradients which existed in 0 rpm test runs were large and natural convection was the predominant mode of heat transfer, the calculated U

may not be a true representation of convection heat transfer. However, since the objective was to evaluate if agitated processing improves the heat transfer rate as compared to still retort processing, a limited number of experiments were carried out with 0 rpm and data were treated in a similar fashion. These data were only used for the purpose of comparison and not included in the statistical analysis of variance.

Moving the can away from the central axis of rotation resulted in some improvement in U values because of the larger centripetal acceleration encountered by the liquid at larger radius of rotation. Increasing the radius of rotation from 0 to 9 cm improved the mean U value by 2% and from 9 to 19 cm, it improved by 3%; however, a further increase in radius of rotation to 27 cm did not change the U value. Overall, the effect of radius of rotation on U, compared to other parameters, was small. For thermal process design, the lower the effect of radius of rotation, the higher the uniformity in terms of lethality achieved in cans placed at different locations in the retort for processing, a desirable situation.

It was found that a small change in headspace also improved the mean U values. This is probably due to an increase in bubble size resulting in more efficient mixing. However, bubble size beyond a critical level may have a dampening effect on the efficiency of mixing due to increased drag on can wall resulting in disturbance in bubble-liquid phenomena (Naveh and Kopelman 1980). The headspace effect on U was the second most significant after rotational speed and an increase in headspace from 6.4 to 10 mm increased the mean U value by 16%. Analysis of variance of data revealed that all four factors were highly significant ($p \leq 0.0001$) with the influence of rotational speed on overall heat transfer coefficient being the most significant (Table 5 for retort temperature, rotation speed and radius of rotation and Table 6 for retort temperature, rotation speed and headspace). Two-way interaction effects were also significant with all factors; however, their contribution compared to the main effect were small. The main effect-plots are presented in Fig. 3 demonstrating the influence of principle factors described earlier.

Fluid-to-Particle Heat Transfer Coefficient (h_{fp})

Depending on experimental conditions, the fluid-to-particle heat transfer coefficient, h_{fp}, ranged from 23 to 145 $W/m^2.K$. Tables 7 and 8 summarize average h_{fp} values for all the processing conditions. Analysis of variance showed that all factors under study affected the h_{fp} values significantly (Tables 5 and 6). Interaction effects were not significant in this case and the main effects are shown in Fig. 4. Higher h_{fp} values were obtained at higher levels of all four parameters. The mean h_{fp} value increased by about 27% with an increase in the retort temperature from 110 to 130C. Increasing rotational speed from 10 to 20

TABLE 5.
ANALYSIS OF VARIANCE SHOWING THE INFLUENCE OF RETORT TEMPERATURE, ROTATIONAL SPEED AND RADIUS OF ROTATION ON U AND h_{fp}

Source	dF	Sum of Square (%) U	h_{fp}
Model	35	88.8**	72.4**
Retort temperature (RT)	2	03.9**	15.8**
Rotational speed (RS)	2	78.3**	26.7**
Radius of rotation (RR)	3	03.3**	22.8**
Interactions			
RT x RS	4	0.8**	1.1
RT x RR	6	1.0**	1.3
RS x RR	6	0.8*	2.1
RT x RS x RR	12	0.7	2.6
Residual (error)	55	11.2	27.6
	77 (h_{fp})		
Total	90		
	112 (h_{fp})		

** $p \leq 0.0001$, * $p \leq 0.005$

TABLE 6.
ANALYSIS OF VARIANCE SHOWING THE INFLUENCE OF RETORT TEMPERATURE, ROTATIONAL SPEED AND HEADSPACE ON U AND h_{fp}

Source	dF	Sum of Square (%) U	h_{fp}
Model	17	90.1**	80.4**
Retort temperature (RT)	2	05.5**	06.8**
Rotational speed (RS)	2	61.4**	17.6**
Headspace (HS)	1	16.7**	54.2**
Interactions			
RT x RS	4	1.0	0.6
RT x HS	2	0.2	0.3
RS x HS	2	4.2**	0.4
RT x RS x HS	4	0.7	0.5
Residual (error)	52	09.9	19.6
	40 (h_{fp})		
Total	65		
	57 (h_{fp})		

** $p \leq 0.0001$

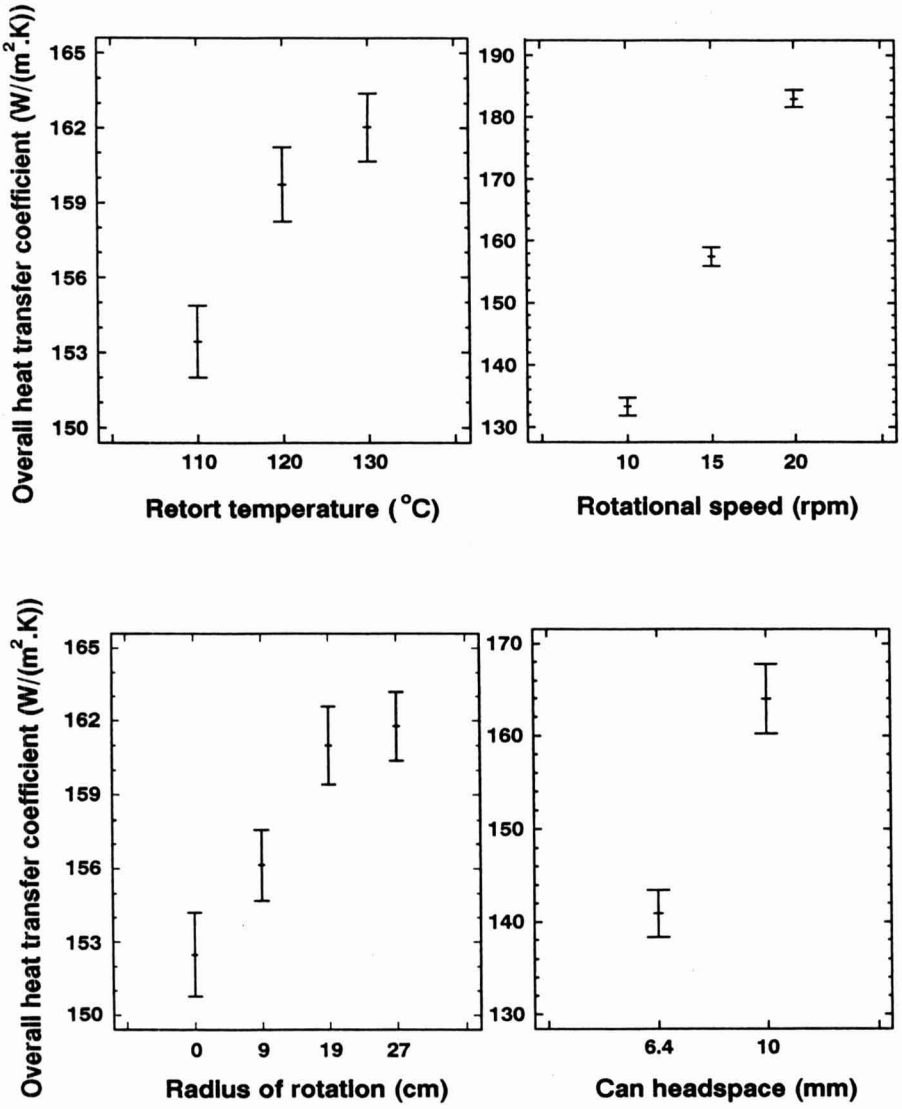

FIG. 3. OVERALL HEAT TRANSFER COEFFICIENT (U) AS INFLUENCED BY RETORT TEMPERATURE, ROTATIONAL SPEED, RADIUS OF ROTATION AND CAN HEADSPACE

(Each point represents the overall mean value. Error bars represent ± standard deviation)

TABLE 7.
FLUID-TO-PARTICLE HEAT TRANSFER COEFFICIENT, h_{fp}, AS INFLUENCED BY RETORT TEMPERATURE, ROTATIONAL SPEED AND RADIUS OF ROTATION

Retort Temperature (°C)	Rotational Speed (rpm)	Radius of Rotation (cm)	h_{fp} ($W/m^2 K$)
110	10	0	69.6 ± 0.4
		9	68.2 ± 3.3
		19	95.0 ± 1.6
		27	95.6 ± 3.9
	15	0	86.3 ± 0.8
		9	82.8 ± 4.7
		19	109.7 ± 6.2
		27	123.6 ± 6.8
	20	0	103.3 ± 0.8
		9	107.8 ± 7.9
		19	123.3 ± 4.7
		27	126.3 ± 12.4
120	10	0	73.0 ± 6.0
		9	77.7 ± 5.2
		19	99.5 ± 1.5
		27	94.8 ± 4.0
	15	0	91.5 ± 1.0
		9	95.3 ± 7.0
		19	115.0 ± 14.1
		27	133.6 ± 11.9
	20	0	110.5 ± 5.5
		9	121.7 ± 8.3
		19	124.0 ± 6.0
		27	137.0 ± 18.6
130	10	0	88.8 ± 11.3
		9	96.0 ± 2.2
		19	109.0 ± 4.0
		27	122.3 ± 7.6
	15	0	110.0 ± 6.5
		9	118.0 ± 15.6
		19	137.5 ± 2.5
		27	137.0 ± 16.4
	20	0	118.3 ± 6.8
		9	125.7 ± 4.9
		19	142.5 ± 2.5
		27	135.5 ± 2.9

TABLE 8.
FLUID-TO-PARTICLE HEAT TRANSFER COEFFICIENT, h_{fp}, AS INFLUENCED BY RETORT TEMPERATURE, ROTATIONAL SPEED AND HEADSPACE (mm)

Retort Temperature (°C)	Rotational Speed (rpm)	Headspace (cm)	h_{fp} (W/m^2K)
110	0	6.4	25.2 ± 1.6
	10	6.4	49.3 ± 2.9
		10	95.0 ± 1.0
	15	6.4	61.3 ± 1.3
		10	109.7 ± 6.2
	20	6.4	73.3 ± 1.3
		10	123.3 ± 4.7
120	0	6.4	27.4 ± 1.1
	10	6.4	53.5 ± 2.1
		10	99.5 ± 1.5
	15	6.4	66.5 ± 2.4
		10	115.0 ± 14.1
	20	6.4	94.2 ± 13.2
		10	124.0 ± 6.0
130	0	6.4	32.1 ± 3.0
	10	6.4	61.2 ± 4.6
		10	109.0 ± 4.0
	15	6.4	83.0 ± 1.0
		10	137.5 ± 2.5
	20	6.4	100.5 ± 1.5
		10	142.5 ± 2.5

rpm improved mean h_{fp} value by 37% probably due to increased particle-to-fluid relative velocity at higher rotational speed. However, the influence of rotational speed on h_{fp} was less than that of headspace unlike in the case of U probably due

to associated small changes in particle to fluid velocity. Since the density of polypropylene particles was relatively closer to that of the bath oil, the particle settling due to gravity was minimal. The effect of radius of rotation on h_{fp}, on

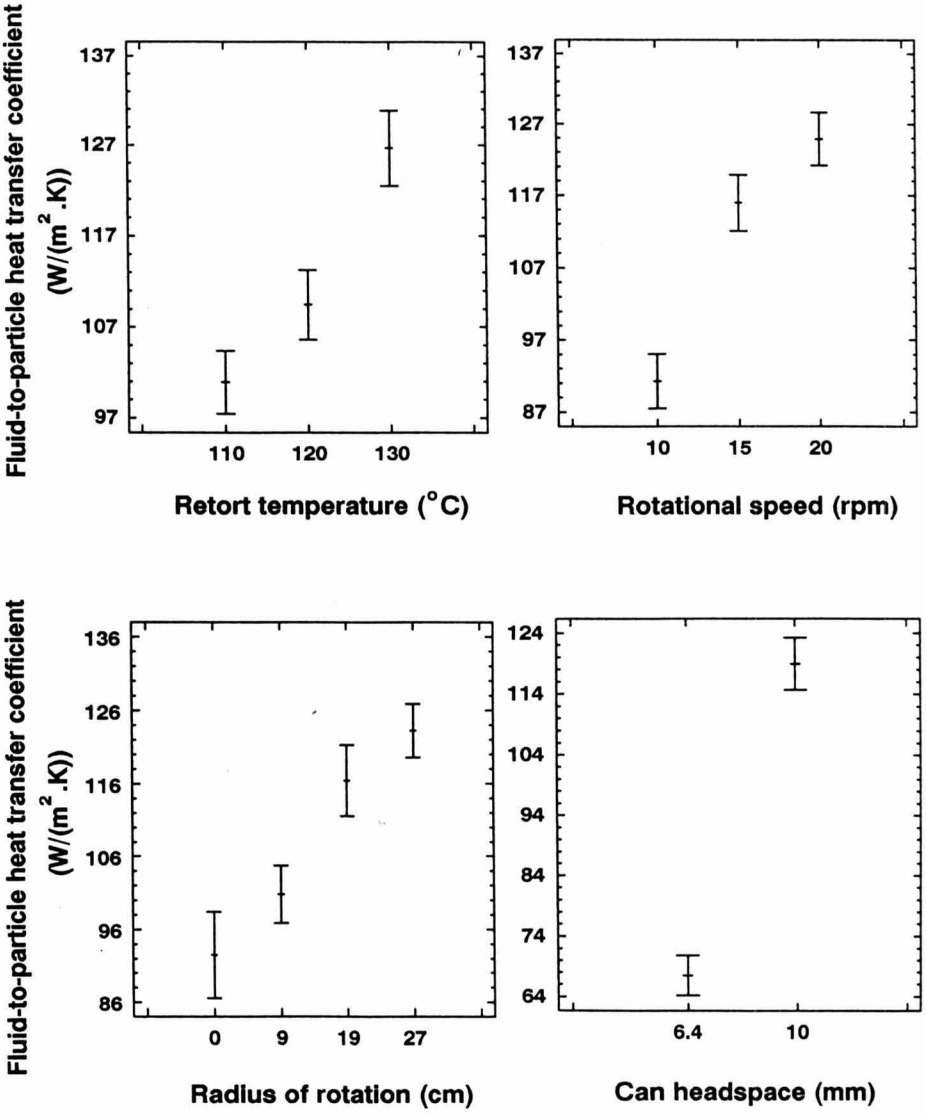

FIG. 4. FLUID-TO-PARTICLE HEAT TRANSFER COEFFICIENT (h_{fp}) AS INFLUENCED BY RETORT TEMPERATURE, ROTATIONAL SPEED, RADIUS OF ROTATION AND CAN HEADSPACE

(Each point represents the overall mean value. Error bars represent ± standard deviation)

the other hand, was more pronounced than with U. Increasing radius of rotation improved the h_{fp} in a sigmoidal fashion as shown in Fig. 4. At the lower end, an increase in radius of rotation from 0 to 9 cm improved the mean h_{fp} by 8% and a further increase from 9 to 19 cm improved mean h_{fp} by 16%, and again at the higher end, an increase in the radius of rotation from 19 to 27 cm changed the mean h_{fp} by only 6%. Radius of rotation effect on h_{fp} compared to the those of can headspace and rotational speed was also less, which is again better in terms of process design point of view. Headspace effect on h_{fp} was the most significant compared to the other three parameters under study. Higher bubble velocity due to its larger size resulted in better mixing and affected the particle to fluid velocity, also probably causing local turbulence surrounding the particle area. A change in headspace from 6.4 to 10 mm increased the mean h_{fp} by 75%.

Error Analysis

Error analysis results are summarized in Table 9. The thermocouple misplacement error of 1.9 mm from the center of the particle reduced the calculated h_{fp} values by only 1.1% at the lower end and at the higher end the reduction was 3.9%. The low errors are probably due to high thermal diffusivity of polypropylene particle used as model food particle. The error in temperature measurement due to thermocouple displacement at the particle center will be even lower due to symmetry of temperature distribution around the center. A change in thermal diffusivity of particle by +5% reduced the h_{fp} in its lower and higher range by 2 and 7.5%, respectively. A -5% change in thermal diffusivity resulted in 3 and 9.5% increase in h_{fp}, respectively. The h_{fp} values increased by 1.5 and 3.2% when the particle size changed by +0.5% and a -0.5% change in particle size reduced the calculated h_{fp} by 0.3 and 1.5% in the lower and higher range, respectively.

TABLE 9.
% ERROR ASSOCIATED WITH CALCULATED HEAT TRANSFER COEFFICIENT, h_{fp}, VALUES AS INFLUENCED BY ERROR IN CHARACTERISTIC PARAMETERS

Parameter	Level	Lower end of h_{fp}	Higher end of h_{fp}
Thermocouple misplacement	1.9 mm (20% of particle radius)	1.1	3.9
Thermal diffusivity	+ 5%	2.0	7.5
	-5%	3.0	9.5
Particle size	+ 0.5%	1.5	3.2
	- 0.5%	0.3	1.5

CONCLUSIONS

An experimental study of forced convection heat transfer in cans during end-over-end processing is reported. Temperature uniformity of liquid in cans was verified using heat penetration parameters and standard deviation of temperature at different location at various rotational speeds. Forced convection heat transfer coefficients were influenced ($p \leq 0.0001$) by all parameters studied. Rotational speed effect was more predominant in the case of U but headspace effect was the most significant on h_{fp}. Effect of radius of rotation on U and retort temperature effect on h_{fp} was least among all the four parameters. The effect of system variables has been evaluated in this study. Apart from these, parameters related to physical properties of the particle, i.e., particle size, shape, density and particle fraction and also fluid viscosity strongly affect the U and h_{fp}. These are currently being explored.

NOMENCLATURE

a	Radius of sphere, m
A	Total external surface area, m^2
C_p	Heat capacity, J/kg.K
$f_{h,f}$	Heating rate index, min
F_o	Process lethality, min
h_{fp}	Fluid-to-particle heat transfer coefficient, $W/m^2.K$
H	Height from the bottom of can, mm
j_{ch}	Heating lag factor
k	Thermal conductivity, W/m.K
L	Length of thermocouple, mm
LALD	Least Absolute Lethality Difference
LSTD	Least sum of Squared Temperature Differences
m	Mass, kg
r	Radial coordinate system
T	Temperature, °C
t	Time, s
t_1	Time in the curvilinear portion of the heating curve, s
U	Overall heat transfer coefficient, $W/m^2.K$
$< >$	Volume average

Greek symbol

α	Thermal diffusivity, m^2/s

Subscripts

c	Can
i	Initial condition
f	Fluid
p	Particle
R	Retort
s	Surface

REFERENCES

BERRY, JR., M.R. and BRADSHAW, J.G. 1980. Heating characteristics of condensed cream of celery soup in a Steritort: Heating penetration and spore count reduction. J. Food Sci. *45*, 869–874, 879.

BERRY, JR., M.R. and BRADSHAW, J.G. 1982. Heat penetration for sliced mushrooms in brine processed in still and agitating retorts with comparisons to spore count reduction. J. Food Sci. *47*, 1698–1704.

BERRY, JR., M.R. and DICKERSON, R.W. 1981. Heating characteristics of whole kernel corn processed in a Steritort. J. Food Sci. *46*, 889–895.

BERRY, JR., M.R., SAVAGE, R.A. and PFLUG, I.J. 1979. Heating characteristics of cream-style corn processed in a Steritort: Effect of headspace, reel speed and consistency. J. Food Sci. *44*, 831–835.

DENISTON, M.F., HASSAN, B.H. and MERSON, R.L. 1987. Heat transfer coefficients to liquids with food particles in axially rotating cans. J. Food Sci. *52*, 962–966, 979.

FERNANDEZ, C.L., RAO, M.A., RAJAVASIREDDI, S.P. and SASTRY, S.K. 1988. Particulate heat transfer to canned snap beans in Steritort. J. Food Process Engineering *10*, 183–198.

HAYAKAWA, K-I. 1977. Mathematical methods for estimating proper thermal processes and their computer implementation. Adv. in Food Res. *23*, 75–141.

LENZ, M.K. and LUND, D.B. 1978. The lethality-Fourier number method. Heating rate variations and lethality confidence intervals for forced-convection heated foods in containers. J. Food Process Engineering *2*, 227–271.

NAVEH, D. and KOPELMAN, I.J. 1980. Effect of some processing parameters on the heat transfer coefficients in a rotating autoclave. J. Food Processing Preservation *4*, 67–77.

OZISIK, M.N. 1985. *Heat Transfer: A Basic Approach*, International Ed. McGraw-Hill Book Co., Singapore.

RAMASWAMY, H.S. 1993. Come-up time effectiveness for process calculations involving thin-profile packages. J. Food Eng. *19*, 109–117.

RAMASWAMY, H.S. and TUNG, M.A. 1981. Thermo-physical properties of apples in relation to freezing. J. Food Sci. *46*, 724–729.

RAO, M.A. and ANANTHESWARAN, R.C. 1988. Convective heat transfer to fluids in cans. Adv. Food Res. *32*, 39–84.

SABLANI, S.S. and RAMASWAMY, H.S. 1995. Fluid/particle heat transfer coefficient in cans during end-over-end processing. Lebensm.-Wiss. u.-Technol. *28* (1), 56–61.

SASTRY, S.K. 1984. Convective heat transfer coefficients for canned mushrooms processed in still retorts. ASAE Paper No. 84, 6517.

SINGH, R.P. 1982. Thermal diffusivity in food processing. Food Technol. *36* (2), 87–91.

STOFOROS, N.G. and MERSON, R.L. 1990. Estimating heat transfer coefficients in liquid/particulate canned foods using only liquid temperature data. J. Food Sci. *55*, 478–483.

STOFOROS, N.G. and MERSON, R.L. 1991. Measurement of heat transfer coefficients in rotating liquid/particle systems. Biotechnol. Prog. *7*, 267–271.

STOFOROS, N.G. and MERSON, R.L. 1992. Physical property and rotational speed effect on heat transfer in axially rotating liquid/particulate canned foods. J. Food Sci. *57*, 749– 754.

WENG, Z., HENDRICKX, M., MAESMANS, G. and TOBBACK, P. 1992. The use of time-temperature-integrator in conjunction with mathematical modelling for determining liquid/particle heat transfer coefficients. J. Food Eng. *16*, 197–214.

ANALYSIS OF EXPANDED-FOOD TEXTURE BY IMAGE PROCESSING
PART I: GEOMETRIC PROPERTIES

X. GAO and J. TAN[1]

Dept. of Biological & Agricultural Engineering
University of Missouri
Columbia, MO 65211

Accepted for Publication January 14, 1996

ABSTRACT

Color image processing techniques were developed to characterize the textural properties of expanded food products. Three major approaches were taken to extract image features from surface and cross-section images of a test product. Scanning electronic microscopy (SEM) was employed to measure the cell size and density. Correlation and regression analyses were performed between the image features and SEM measurements. A number of image features were found highly descriptive of texture-related geometric properties.

INTRODUCTION

Among the attributes and quantities that collectively define food quality, texture is an important quality aspect for numerous food products. In the sensory literature, the term texture is used to describe an assortment of characteristics. Brandt (1963) and Szczesniak (1963) described texture in terms of geometric and mechanical characteristics plus moisture and fat contents. Their definition of a texture profile and classification of textural properties have become a set of unified terminologies used by the food industry in texture evaluation. The related geometric characteristics include particle size, shape and orientation describing popular terms like gritty, grainy and cellular, etc. The pertinent mechanical characteristics are hardness, cohesiveness (describing brittleness, chewiness and gumminess), viscosity, elasticity, and adhesiveness (denoting stickiness, tackiness and gooeyness). Moisture and fat contents are used to indicate if a product is moist, oily or greasy.

[1]To whom correspondence should be addressed.

Journal of Food Process Engineering **19** (1996) 425–444. *All Rights Reserved.*

The textural characteristics described above are not all independent of one another and some may not be applicable to a specific product. For most expanded food products, moisture and fat contents are either unimportant, as in the case of a dry and oilless product, or easily determinable from ingredient formulae or product samples by analytical means. Furthermore, moisture and fat contents are relatively easy to control and their effects are also manifested in the geometric and mechanical properties. For expanded-food texture analysis, therefore, the geometric and mechanical characteristics are often of particular interest.

For routine process monitoring and quality control, the texture-related geometric and mechanical properties are usually measured by instrumental methods. For expanded products, the most important geometric properties are those relating to their cellular structures. Scanning electronic microscopy (SEM) is often used to reveal the internal structure (cross sections) and/or surface appearance in details. From SEM photographs, surface roughness can be observed; cell size, shape and density (count per unit area) can be examined or estimated.

The mechanical properties are associated with mechanical strength and deformation. The most widely used instrumental method for mechanical property measurement is shear or compression test on an Instron universal testing machine. The result of an Instron test is a strain-stress relationship, from which various mechanical properties can be derived.

The texture-related geometric and mechanical characteristics of a food product are directly or indirectly related to its appearance. Evidently, most, if not all, geometric characteristics of interest are visible. The mechanical characteristics of an expanded product relate to its cellular structure and material properties. The cellular structure is visible and the material properties are to some extent reflected on the cellular structure, surface roughness, color and other visible characteristics. This indicates that the texture-related geometric and mechanical characteristics of expanded food products may be revealed and analyzed to a great degree by studying their appearances or images.

Image processing techniques have been developing rapidly in the past two decades. Various statistical and structural approaches, such as those based on textural edginess, structural primitives, grey level co-occurrence and run-length, have been applied in image texture analysis (Haralick 1979). Image processing is undoubtedly a promising new method for food texture analysis. This technology can not only expedite and automate the assessment process for some important food quality attributes but also enhance the objectivity and consistency of measurement results.

There have been a few studies on image processing applications in expanded-food quality assessment. Smolarz *et al.* (1989) used image analysis to evaluate transverse cuts of extruded biscuits. They found that the mean

orientation, mean area and standard deviation of pores were useful in discriminating two types of extruded biscuits. Barrett and Peleg (1992) used an image analyzer to trace the edges in cross-section images of corn puffs displayed on a computer screen. They analyzed the cell size distribution and identified two useful distribution functions. Tan *et al.* (1994) used image processing techniques to measure quality attributes of puffed extrudates. A number of features in color and surface texture were developed and tested for their sensitivity to product appearance changes resulting from variations in extrusion conditions.

The objective of this research was to apply and develop image processing techniques for analysis of expanded-food texture. This entailed extensive development of image features and processing algorithms to characterize the cross-section and surface image texture of a test product. The image features were correlated and compared with SEM measurements for texture-related geometric properties and with Instron measurements for texture-related mechanical properties. The results on geometric properties are reported in Part I and those on mechanical properties reported in Part II.

EQUIPMENT AND SEM MEASUREMENTS

Sample Preparation

Expanded product samples were made through a 50-mm APV-Baker twin-screw food extruder from yellow corn meal. The samples were prepared in a completely randomized experiment design for the following conditions:

Screw Speed: 250, 300, 350 and 400 rpm
Moisture Content: 17%, 20% and 23% (w.b.)

The material feed rate was fixed at 45 kg/h. The levels of screw speed and moisture content covered their normal ranges used for the extruder. The experiments included twelve combinations of processing conditions and thus gave twelve sets of samples. There were visible differences among the sample sets in degree of expansion, cell size, cell distribution, surface roughness, color and other properties.

Image Processing System and Image Acquisition

The computer vision system used for this study consisted of a Sony XC-711 CCD color camera, a Sony PVM-1342Q color video monitor, a Data Translation (Marlboro, MA) DT2871 color image frame grabber, a DT2878 advanced processor, and two programming libraries (AURORA and AIPL) hosted by a 486-50 MHz microcomputer. The image processing algorithms were programmed in Microsoft C/C++ 7.00. The camera was mounted in an enclosed

chamber with warm white deluxe (WWX) fluorescent lighting. The WWX lamps had a color rendering index of 79 and color temperature of 3000 K.

Cross-section and surface images of seven samples per set were acquired individually in the chamber with a uniform black background. The same exposure and focal distance were used for all the images. The chosen exposure was such that the image intensity histograms were roughly centered at the middle of the full scale range (0-255), which gave the best resolution and clearest images. The focal distance was selected to allow the side view of the largest sample to fit in the image frame. Figures 1 and 2 show sections of some example images. The surface images contain information of surface texture while the cross-section images show the internal structure.

Each color image consists of the hue, saturation and intensity frames. Figure 3 shows the three frames of a surface image section along with their histograms. It can be seen that the intensity and saturation frames have more contrast and show the texture more clearly than the hue frame.

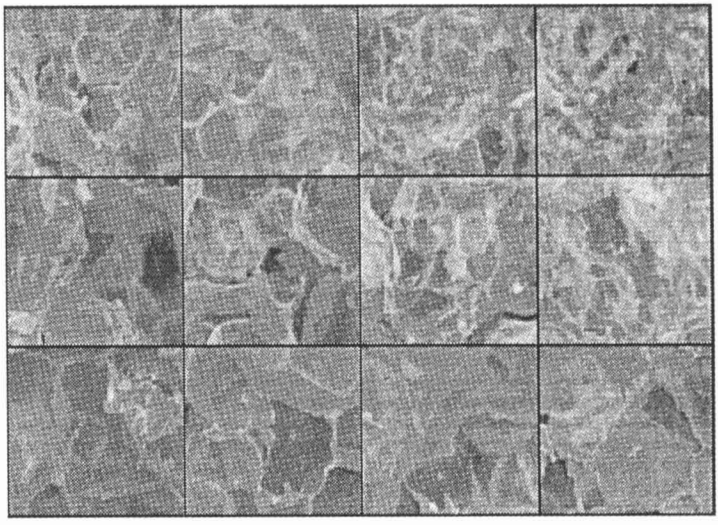

FIG. 1. CROSS-SECTION IMAGES (INTENSITY) FROM THE 12 SAMPLE SETS
(Left to right: screw speed = 250, 300, 350 and 400 rpm; top to bottom: moisture content = 17, 20 and 23% w.b.)

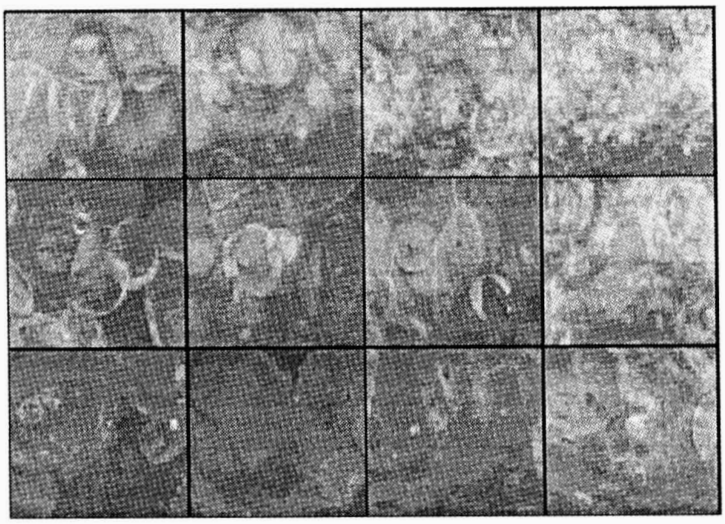

FIG. 2. SURFACE IMAGES (INTENSITY) FROM THE 12 SAMPLE SETS
(Left to right: screw speed = 250, 300, 350 and 400 rpm; top to bottom: moisture content = 17, 20 and 23% w.b.)

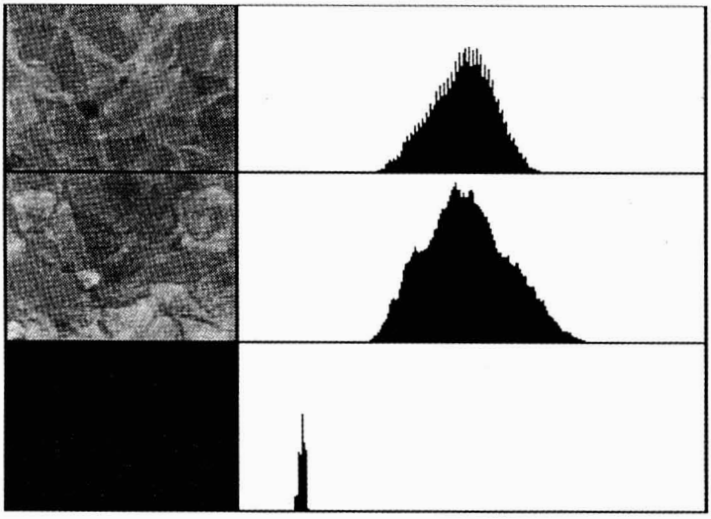

FIG. 3. THE INTENSITY, SATURATION AND HUE FRAMES OF A SAMPLE IMAGE WITH THEIR PIXEL VALUE HISTOGRAMS
(Top to bottom: I, S and H)

SEM Images and Geometric Measurements

Three samples per set were carefully dissected in the transverse direction. The samples were gold-coated and cross-section images were taken by using an AMRAY model-1600 scanning electronic microscope with a 10-kV acceleration voltage and a magnification factor of 9.8. The black and white SEM images, 512 × 512 pixels in size, clearly revealed the detailed internal structure of a sample. Figure 4 shows an example SEM image.

The SEM images showed that there were clear differences in the cellular structure among the sample sets. The cell shape was roughly circular and exhibited little discernable variations from one sample set to another. The geometric differences were predominantly in cell density and size. Therefore, the following two texture-related geometric properties were measured from each SEM image:

(1) N - number of cells per unit area or cell density, and
(2) A - cell size represented by the average area of the three largest cells in a cross section.

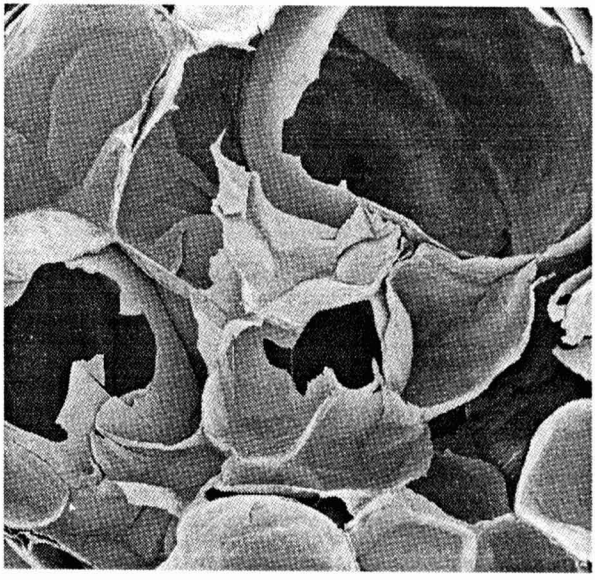

FIG. 4. SCANNING ELECTRONIC MICROSCOPE IMAGE OF A SAMPLE CROSS-SECTION

The number of cells within a fixed image area was counted manually to give N. Examination of the SEM images indicated that the cell sizes differed among sample sets primarily for a few large cells. All samples had many small

cells. It was mainly the sizes of a few large cells that varied considerably from one sample to another. The areas of the three largest cells were thus measured from the SEM images and averaged to serve as a representative cell size.

IMAGE TEXTURE FEATURE EXTRACTION

Image texture features were extracted from the color images acquired to represent the textural characteristics of the product samples. As shown by Fig. 1 and 2, the images have a cellular structure but do not exhibit a readily identifiable repetitive pattern; in other words, the cell size and spatial arrangement vary in a rather random manner. This has been verified in Tan *et al.* (1994) by the fact that the power spectra of such images had little dependence on the spatial direction on the image plane. An image texture with identifiable spatial relationships among its structural primitives would tend to have direction-dependent properties. The lack of repetitive spatial patterns classifies such images as weak textures (Haralick 1979). Expanded-food textures are primarily in this category. Weak image textures are most effectively characterized by statistical approaches. Three major approaches were employed in this research.

Edge Enhancement and Segmentation

Each image frame (H, S or I) is a spatial function, f(x, y), which is simply the pixel value over the 2-D image plane (x, y). The gradient of f(x, y) is

$$\nabla f = \begin{bmatrix} G_x \\ G_y \end{bmatrix} = \begin{bmatrix} \frac{\partial f}{\partial x} \\ \frac{\partial f}{\partial y} \end{bmatrix} \tag{1}$$

where G_x and G_y are respectively the gradients in the x and y directions. The magnitude of this gradient vector is also simply referred to as the gradient and denoted by ∇f; i.e.,

$$\nabla f = |\nabla f| = [G_x^2 + G_y^2]^{1/2} \tag{2}$$

The partial derivatives, G_x and G_y, can be obtained by convolving Sobel operators with an image function, which results in two partial derivative images. The gradient image is obtained from the partial derivative images according to Eq. 2.

The middle part of Fig. 5 is the gradient image of the original intensity function shown by the left part of the same figure. In the gradient image, edges were enhanced and nonedges darkened. The contrast between edges and nonedges was increased, but information about the cell structure was preserved.

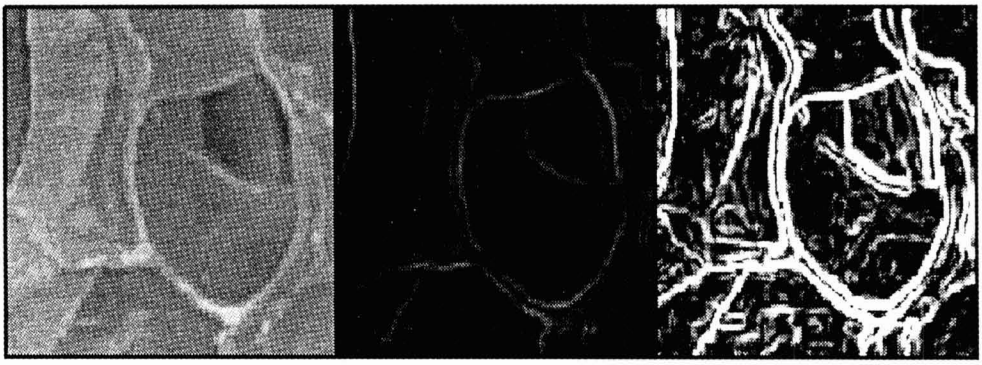

FIG. 5. EDGE ENHANCEMENT AND SEGMENTATION
(Left: intensity of an original cross-section image; middle: edge-enhanced; right: segmented)

The amount of wall edges (or inversely the nonedges) in an image area can be used to describe textural characteristics. More edges per unit image area indicates more walls and thus more but smaller cells. Such information is contained in the pixel value histograms of the gradient images. Both the histogram shape and location would be affected by the amount of wall edges. For example, if a sample has many but small cells, there would be a large amount of edges in its image. Since the edges are brightened in the gradient image, its histogram would have a different shape from that for a sample with less but larger cells. This would lead to variations in the following statistical properties of the gradient image histograms, which were computed as textural features:

(1) μ_e - mean;
(2) σ_e - standard deviation;
(3) M_{e3} - third moment as defined by

$$M_{e3} = \frac{\sum P(V)(V-\mu_e)^3}{N_v} \tag{3}$$

where $P(V)$ is the frequency for pixel value V, and N_v is the total number of pixels;
(4) P_{max} - maximum frequency, and
(5) V_{max} - pixel value of most occurrence (the pixel value corresponding to P_{max}).

If the wall edges are segmented from the nonedges, the amount of edges in an image area can be computed as an indicator of the amount of walls. The pixel

value histograms of both the original and gradient images, however, do not exhibit distinctive peaks (Fig. 3 and 6), indicating that the pixel values of edges overlap with those of nonedges and a simple threshold value cannot be easily determined from the histograms for image segmentation. For the product samples, nevertheless, nonedges constitute a majority of the image area and the edge enhancement operation significantly magnifies the pixel value difference between edges and nonedges as evidenced by the considerable skewness of the histogram in Fig. 6. It would therefore be a reasonable assumption that pixel values $\leq V_{max}$ belong to nonedges. It may be further assumed that the pixels belonging to nonedges proportionally decrease from V_{max} to $2V_{max}$ as shown by the dashed line in Fig. 7 if the nonedge histogram is considered approximately symmetrical about V_{max}. Then edges and nonedges can be segmented by performing a transformation shown by the solid line in Fig. 7 on the edge-enhanced images. The transformation classifies pixels with a value between V_{max} and $2V_{max}$ as partial edges, which reflects the fact that there is not an abrupt pixel value change from edges to nonedges and the pixel values for the two classes overlap in this range.

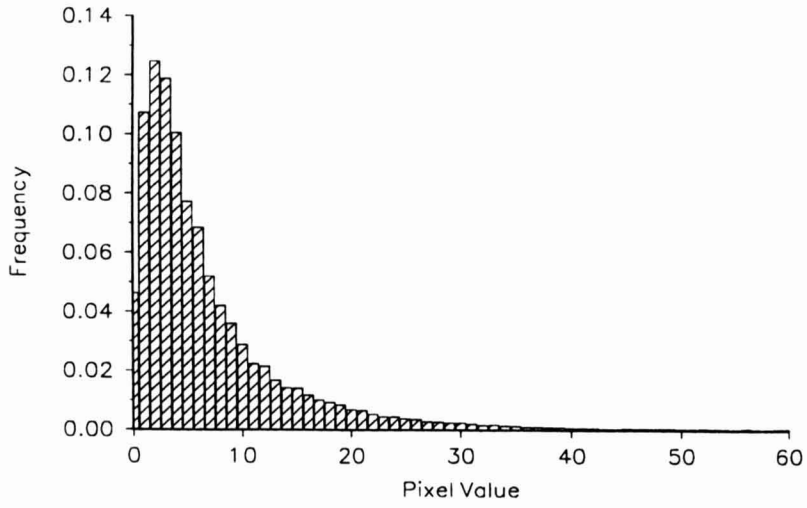

FIG. 6. PIXEL VALUE HISTOGRAM OF AN EDGE-ENHANCED IMAGE

After segmentation, the gradient image in the middle of Fig. 5 becomes that to the right of the same figure, where nonedge pixels have 0 values, edge pixels have 255 and partial edges have a value in between. Two more edge features

were computed from the segmented images as indicators of the texture-related geometric properties:

(6) L_e - total edge length, which is simply the number of edge pixels in a segmented image. A pixel with a value V is counted as V/255 of an edge pixel.

(7) S - nominal cell size, which is the total nonedge area (total image area in pixels subtracted by L_e) divided by the total edge length. S can be thought as the ratio of an area over its perimeter and is thus called nominal cell size.

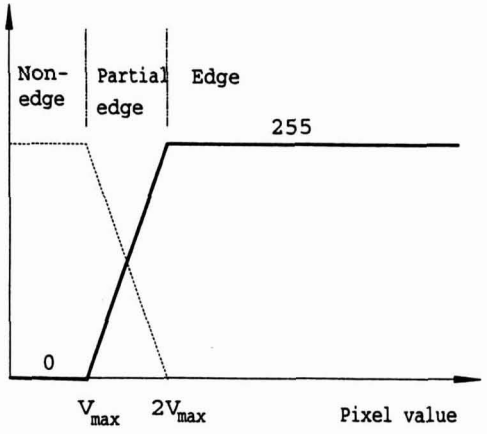

FIG. 7. TRANSFORMATION FUNCTION FOR EDGE SEGMENTATION

Pixel Value Band Run Length

In an expanded food sample image, the voids and walls can be viewed as image texture primitives; i.e., they are the building blocks of the image texture. Within a primitive or block, pixel value variation is relatively small and the pixel values are within a relatively narrow band, forming a fairly smooth and contiguous area. The sizes of such contiguous areas should depend on the cell sizes and thus show textural properties. This motivated the use of run lengths of pixel value bands in a chosen direction. The histogram of pixel value band run length is defined as

$$P = f(R; \Theta, T)$$

where P stands for probability, R is run length in number of pixels, Θ is the run direction on the image plane, and T is the pixel value band thickness. The pixel value band run lengths are computed as follows (for $\Theta=0°$ or horizontal run):

Step 1. Start with the first pixel in a row, count run length R as 1, and set the average pixel value for the current run V_{av} as the first pixel value;

Step 2. Move to the next pixel in the same row; if

$$|V-V_{av}| \leq T/2 \tag{4}$$

then, the pixel is included into the current run, the current run length R is increased by 1 and V_{av} is updated.

Step 3. Repeat step 2 until the condition in Eq. 4 is not satisfied; then, the current pixel marks the beginning of a new run. If the last pixel of the row is reached, go to step 1.

From the run lengths computed, a sample run length histogram can be constructed. Runs can be tallied similarly in different directions to capture direction-dependent properties of a texture (such as oblong cells). For the test samples used, there was little discernable directional trends in the image texture; thus, only $\Theta=0°$ was used.

Different selections of band thickness T give run lengths showing different levels of details of an image texture. A small T will result in short run lengths indicating local textural properties, while a large T will capture textural properties in a large scale. One good choice of T would be an estimated magnitude of pixel value variation within texture primitives. In this research, this was determined by examining the pixel value variations inside the cells. Run lengths for such a T value would be associated with the cellular structure of the product. Three T values were used: 8, 10 and 12.

With a proper selection of camera focal distance, the product cells should generally be much smaller than the image size in the run direction and much larger then zero. Neither very long nor very short run lengths are related to and indicative of the cell sizes. Many short and long run lengths, however, result from the irregularities in the cellular structure of expanded foods. To reduce the effects of short and long run lengths and to emphasize the medium ones, the run length histograms were weighted with the weighting function defined in Fig. 8, where L is an estimated maximum run length associated with the cellular structure.

A weighted histogram of run length is shown in Fig. 9. The following features were computed from the weighted pixel value band run length histograms:

(1) μ_{rT} - mean run length, used to indicate the average cell size, and
(2) σ_{rT} - standard deviation of run length, which may also show the cell size and density since the cell variation appears to increase with cell size.

Subscript T in the symbols denote the band thickness T used.

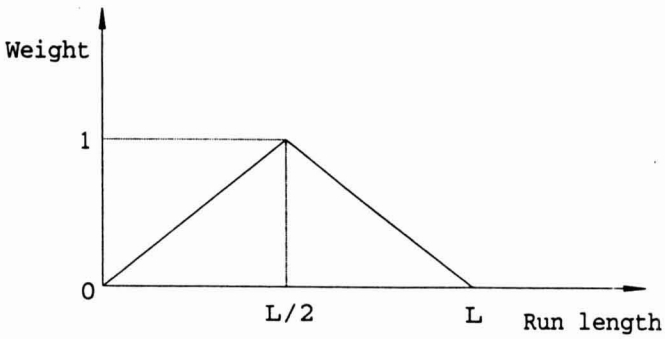

FIG. 8. WEIGHTING FUNCTION USED FOR RUN LENGTH HISTOGRAMS

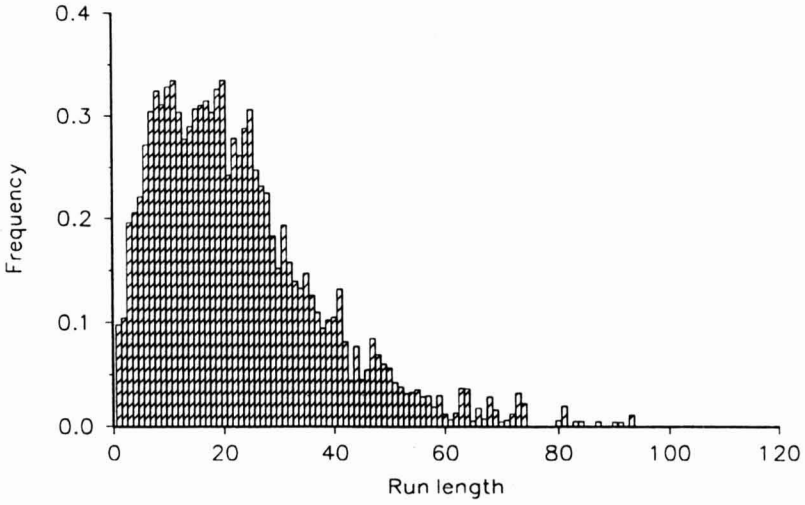

FIG. 9. A WEIGHTED RUN-LENGTH HISTOGRAM

Pixel Value Spatial Dependence

Another method to analyze image textures is to examine the pixel value relationships of a pixel with those a specified distance away. One way to study such relationships is to compute a pixel value co-occurrence matrix, P (Haralick *et al.* 1973). Co-occurrence matrix P is a 2-dimensional histogram, with entry $P(i,j;\Theta,D)$ being the frequency for one pixel value to equal i and for another pixel D pixels away in direction Θ to equal j. This 2-D histogram can show some important characteristics of an image texture. For example, a perfectly smooth image would have only one nonzero entry in the histogram and a rough image with completely random pixel values would result in a flat histogram surface. From the P matrix, several textural features can be extracted. Haralick *et al.* (1973) proposed 14 features (F_1 to F_{14}) based on the matrix (see Haralick *et al.* 1973 for details). The features are not independent of one another and some indicate similar image properties. The following were considered potentially useful for the product images and used in this research:

(1) F_1 - angular second moment, which shows the homogeneity of an image,
(2) F_2 - difference moment, which is an indicator of contrast or degree of local variations,
(3) F_3 - correlation, a measure of pixel value linear dependencies,
(4) F_4 - variance, which signifies the roughness of an image, and
(5) F_9 - entropy, another measure of image homogeneity.

The spatial distance D and direction Θ play similar roles to band thickness T and run direction Θ in pixel value band run length. A small D results in a P matrix relating to the detailed local properties of an image while a large D leads to properties in a large scale. A proper value of D should be around the average size of textural primitives of interest, which are the cells for expanded foods. A number of D values were tested. Again, since the product samples were isotropic, the P matrix was computed only for the horizontal direction ($\Theta=0$).

RESULTS AND DISCUSSION

The extracted image features were computed from the sample images. As shown by Fig. 3, the intensity (I) and saturation (S) functions displayed the textural properties while the hue function had little contrast to show the geometric variations. The image texture features were thus computed from the intensity and saturation functions only. Both the cross-section and surface images were used. The image feature values and SEM measurements were averaged over their replications (7 and 3, respectively). Correlation and regression

analyses were performed to show the effectiveness of the image features in describing the textural geometric characteristics of the product samples.

Features from Edge Enhancement

The correlation coefficients between the features from edge enhancement and the SEM measurements are shown in Table 1. The image features from the edge-enhanced intensity functions of both the surface and cross-section images were highly correlated to the SEM measurements. The pixel value of most occurrence (V_{max}) and maximum frequency (P_{max}) of pixel values were effective indicators of cell density N and cell area A (R values up to 0.93).

Since the edges had much higher pixel values than the nonedges, a gradient image with a larger amount of edges (high cell density N and small cell size A) would have more high-valued pixels. Both the pixel value of most occurrence V_{max} and the mean pixel value μ_e of intensity were therefore positively

TABLE 1.
CORRELATION COEFFICIENTS[1] BETWEEN IMAGE FEATURES[2] FROM EDGE ENHANCEMENT AND SEM MEASUREMENTS[3]

	V_{max}	P_{max}	μ_e	σ_e	M_{e3}
			From intensity of surface images		
N	0.91	-0.93	0.83	-0.82	-0.79
A	-0.82	0.88	-0.70	0.88	0.86
			From intensity of cross-section images		
N	0.92	-0.89	0.71	-0.78	-0.75
A	-0.92	0.92	-0.62	0.87	0.86
			From saturation of surface images		
N			0.61	0.87	0.92
A				0.86	-0.86
			From saturation of cross-section images		
N		0.66		0.86	0.90
A		-0.68	0.59	-0.85	-0.86

[1] Correlation coefficients with $p > 0.05$ are omitted.
[2] Image features: V_{max} - pixel value of most occurrence, P_{max} - maximum frequency, μ_e- mean, σ_e - standard deviation, M_{e3} - third moment.
[3] SEM measurements: N - cell density, and A - cell size.

correlated with N and negatively correlated with A. On the other hand, more edge pixels reduced the degree of dominance of the nonedges, leading to a less skewed histogram with lower maximum frequency P_{max}, standard deviation σ_e and third moment M_{e3}, which explains why these features were negatively correlated with N and positively correlated with A. The correlation coefficients for N and A always have opposite signs as one can expect from the fact that larger cell sizes lead to lower cell density. It is also interesting to note from Table 1 that the intensities of both the surface and cross-section images were equally effective in revealing the cell characteristics of the product samples.

The features relating to the position of the gradient histogram for saturation (μ_e and V_{max}) were not useful but the features relating to the histogram shape (σ_e and M_{e3}) effectively showed the cellular structure. This was true for both the surface and cross-section images.

The signs of correlation coefficients for saturation are opposite to those for intensity. This was due to the fact that the saturation function shows not only the cell structure but also the fine texture on the inner or outer surfaces of the bubbles (Fig. 3). The bubble surface texture is more apparent over a larger contiguous bubble surface area of a large cell. When cells are larger, the fine bubble surface texture becomes more dominant over the effects of the wall structure, forming a finer texture in the saturation image. This is just opposite to the texture formed by only the wall edges as shown by the intensity function. Consequently, features based on the saturation function varied in the opposite direction to those based on the intensity function. This was also the case for the features extracted with other approaches.

Features from Edge Segmentation

Table 2 shows the correlation coefficients between the features extracted from the segmented edge images and SEM measurements. Both total edge length L_e and nominal cell size S based on the intensity function were highly correlated with cell density and size. The correlation coefficient between L_e and cell density N reached 0.97. The surface and cross-section images appeared to be equally useful. L_e was positively related to N and negatively to A, indicating that a larger number of small cells did form longer total edges as originally expected. Similarly, the positive correlation of nominal cell size S with A and negative correlation with N indicate that S was a good measure of cell size.

The saturation function was less effective than the intensity function. This was due to two likely reasons. One was that edge segmentation was performed on the basis of V_{max}, which turned out to have insignificant correlation with the cell structure for the saturation function. The other reason was that the saturation function showed the bubble surface texture, which reduced the relative effectiveness of edges in revealing the cell structure. If the bubble surface

conditions such as roughness are of interest, however, the saturation function would be useful.

TABLE 2.
CORRELATION COEFFICIENTS[1] BETWEEN IMAGE FEATURES[2] FROM EDGE SEGMENTATION AND SEM MEASUREMENTS[3]

	Surface		Cross-section	
	L_E	S	L_E	S
		Intensity		
N	0.97	-0.89	0.91	-0.85
A	-0.83	0.88	-0.93	0.92
		Saturation		
N	-0.61	0.65	-0.69	0.80
A	0.72	-0.73	0.72	-0.78

[1] All correlation coefficients shown are significant at $p=0.05$.
[2] Image features: L_e - total edge length, S - nominal cell size.
[3] SEM measurements: N - cell density, and A - cell size.

Features from Pixel Value Band Run Length

Table 3 shows the correlation coefficients between the features extracted from pixel value band run length and SEM measurements. The run length features from the intensity function, especially those computed from the surface images, represented the cellular structure well (R values up to 0.92). Among the three band thicknesses used, 8 appears to give better correlation than others for the particular product tested. The positive correlation of average run lengths (the μ_r's in Table 3) with A (negative with N) show that larger cell sizes did result in longer pixel value band run lengths as expected.

The positive correlation between the run length standard deviation (the σ_r's) and cell area A means that when cell size increases, the variation in cell size also increases. This proves the observation made during SEM measurement that cell size differences among sample sets were predominantly in a few large cells. Size changes in these large cells would then lead to simultaneous changes in average cell size and cell size uniformity. A large σ_r therefore indicates both a large average cell size and significant cell nonuniformity.

The run length features based on the saturation function were not as highly correlated to the cell structure as those based on the intensity function. In fact, those features computed from the surface saturation were not significantly related to N and A at $p=0.05$ and thus omitted from Table 3. The correlation coefficients for saturation had consistently opposite signs to those for intensity as explained earlier.

TABLE 3.
CORRELATION COEFFICIENTS[1] BETWEEN IMAGE FEATURES[2] FROM PIXEL VALUE BAND RUN LENGTH AND SEM MEASUREMENTS[3]

	μ_{r8}	σ_{r8}	μ_{r10}	σ_{r10}	μ_{r12}	σ_{12}
			From intensity of surface images			
N	-0.92	-0.90	-0.90	-0.89	-0.89	-0.88
A	0.86	0.85	0.83	0.82	0.81	0.81
			From intensity of cross-section images			
N	-0.82	-0.80	-0.78	-0.77	-0.75	-0.74
A	0.91	0.91	0.88	0.87	0.85	0.84
			From saturation of cross-section images			
N	0.74	0.76	0.76	0.78	0.78	0.80
A	-0.69	-0.71	-0.71	-0.72	-0.73	-0.74

[1] All correlation coefficients shown are significant at $p=0.01$.
[2] Image features: μ_{rn} - mean run length, σ_{rn} - standard deviation of run length, where subscript n denotes band thickness T in number of pixels.
[3] SEM measurements: N - cell density, and A - cell size.

Features from Pixel Value Spatial Dependence

The pixel value spatial dependence features, F_1 to F_4 and F_9, were computed with different values for spatial distance D, which included 2, 4, 6, 8, 10, 12, 16 and 18 pixels. The correlation coefficients between features for D = 16 and SEM measurements are shown in Table 4. Since the features represent different aspects of a texture and different D values reveal textural properties at different scales as discussed earlier, the level of correlation with N and A for each spatial dependence feature varied with the D value. When D was changed from low to high within the range used, some features became somewhat more correlated with N and A while others became less correlated with them. Overall, D = 16 appeared to be a proper choice for the particular test product.

As shown in Table 4, the saturation function was more useful than the intensity function in revealing the geometric characteristics in terms of the image features computed. The features based on the intensity of cross section images were not significantly correlated with N and A at $p=0.05$ and thus not included in Table 4. The homogeneity feature F_1 (angular moment) and roughness feature F_4 (variance) were found useful. The saturation homogeneity of both surface and cross section images were highly correlated with cell density N. The higher the

cell density was, the more homogeneous the saturation function became. The surface image roughness was an effective indicator of cell size A. A rougher product surface corresponded to larger cell sizes.

TABLE 4.
CORRELATION COEFFICIENTS[1] BETWEEN IMAGE FEATURES[2] FROM PIXEL VALUE SPATIAL DEPENDENCE (D = 16) AND SEM MEASUREMENTS[3]

	F_1	F_2	F_3	F_4	F_9
			From intensity of surface images		
N	-0.69	-0.76	0.87	0.83	0.59
A	0.70	0.87	-0.88	-0.78	-0.63
			From saturation of surface images		
N	0.93	-0.80	0.77	-0.82	-0.78
A	-0.76	0.87	-0.68	0.91	0.74
			From saturation of cross-section images		
N	0.90	-0.74	-0.78	-0.80	
A	-0.72	0.77	0.80	0.85	

[1] All correlation coefficients shown are significant at $p=0.05$.
[2] Image features: F_1 - angular second moment, F_2 - difference moment, F_3 - correlation, F_4 - variance, and F_9 - entropy.
[3] SEM measurements: N - cell density, and A - cell size.

Regression of Geometric Properties vs. Image Features

Cell density N and size A were plotted versus each image feature computed. While the correlation coefficients varied, all the image features appeared to be linearly related to N and A. Regression analysis further confirmed this observation. When N or A was regressed against an image feature, rarely did a second- or higher-order term of the feature survive the SAS backward elimination procedure at a significance level of $p=0.05$.

Since a number of features extracted were highly correlated with N and A, regression relationships can be readily developed to predict N and A from the image features. For example, cell density N may be predicted from total edge length L_e computed from the intensity functions of surface images. A linear regression line of N versus L_e is shown in Fig. 10 along with the measured data. It gave a R^2 value of 0.94. Cell size A may be predicted effectively with several image features. A regression line of A versus the mean pixel value band run length based on the intensity of cross-section images (μ_{r8}) is shown in Fig. 11. The R^2 value was 0.84.

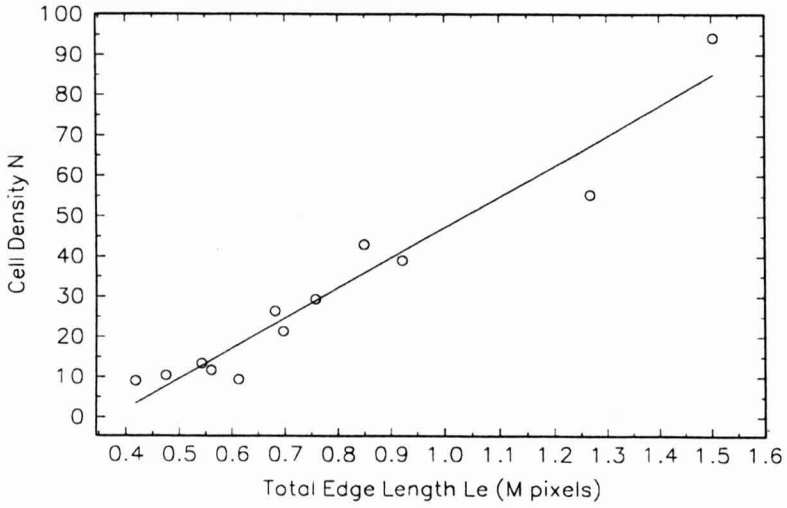

FIG. 10. REGRESSION OF CELL DENSITY AGAINST TOTAL EDGE LENGTH
($R^2 = 0.94$)

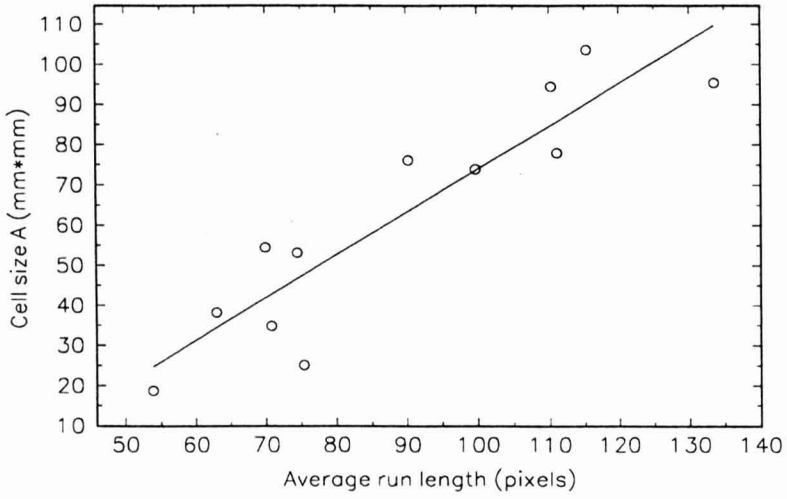

FIG. 11. REGRESSION OF CELL SIZE AGAINST AVERAGE PIXEL BAND RUN LENGTH
(band thickness T = 8, $R^2 = 0.83$)

CONCLUSIONS

A number of image features extracted were highly correlated to the SEM measurements. This indicates that the image processing algorithms developed and used in this research are effective. Edge segmentation and pixel value band run length appear to be useful approaches for extracting textural features of expanded food products. Texture-related geometric characteristics of expanded foods can be rapidly and consistently evaluated through image processing.

Both the intensity and saturation functions of a color image carry useful textural information while the two show different dominant aspects of geometrical characteristics. The high correlation of surface image features with SEM measurements of internal structure indicate that the internal structure of the test product is shown by the surface. This suggests that textural properties of an expanded food product can be assessed from the surface without dissecting the samples.

REFERENCES

BARRETT, A.M. and ROSS, E. 1992. Cell size distributions of puffed corn extrudates. J. Food Sci. *57*(1), 146–154.

BRANDT, M.A., SKINNER, E. and COLEMAN, J. 1963. Texture profile method. J. Food Sci. *28*, 404–410.

GONZALEZ, R.C. and WOODS, R.E. 1992. *Digital Image Processing*. Addison-Wesley, New York.

HARALICK, R.M. 1979. Statistical and structural approaches to texture. Proc. of IEEE, *67*(5).

HARALICK, R.M., SHANMUGUM, K. and DINSTEIN, I. 1973. Textural features for image classification. IEEE Trans. on System, Man and Cybernetics. SMC-*3*(6), 610–621.

SMOLARZ, A., VAN HECKE, E. and BOUVIER, J.M. 1989. Computerized image analysis and texture of extruded biscuits, J. Texture Studies *20*, 223.

SZCZESNIAK, A.S. 1963. Classification of textural characteristics. J. Food Sci. *28*, 385–389.

TAN, J., GAO, X. and HSIEH, F. 1994. Characterization of extrudates by image processing. J. Food Sci. *59*(6), 1247–1250.

ANALYSIS OF EXPANDED-FOOD TEXTURE BY IMAGE PROCESSING PART II: MECHANICAL PROPERTIES

X. GAO and J. TAN[1]

Dept. of Biological & Agricultural Engineering
University of Missouri
Columbia, MO 65211

Accepted for Publication January 14, 1996

ABSTRACT

Image texture and color features were used to represent the mechanical properties of expanded food products. Texture-related mechanical properties were measured through Instron shear and compression tests. The image features extracted were found highly correlated with the mechanical properties. The analysis showed useful relationships between geometric properties and mechanical behavior. Image processing proved to be an effective technique for textural analysis of expanded food products.

INTRODUCTION

The accompanying paper describes extraction of image texture features and analysis of texture-related geometric properties of expanded foods. Another important aspect of expanded-food texture is the related mechanical properties (Szczesniak 1963). This part of the paper reports the results on evaluation of mechanical properties of expanded food products by image processing.

An expanded food sample is a 3-dimensional physical structure. Its mechanical characteristics or responses to forces therefore depend on: (1) the geometric structure, including cell size, thickness and uniformity of walls, and how the walls are arranged; and (2) the physical properties of the wall solids. The geometric structure can be described with image texture features (Part I) and it affects the textural perceptions and mechanical behavior of a product (Barrett and Peleg 1992; Barrett *et al.* 1994). The wall solid properties are conceivably exhibited to some extent by the wall appearance such as color and surface roughness (an aspect of texture). Jin *et al.* (1994) and Lue *et al.* (1994) reported that the color of extruded puffs was significantly influenced by material composition (contents of fiber, salt and sugar), degree of gelatinization, and other variables that determine the wall solid properties. Similar variations in wall

[1]To whom correspondence should be addressed.

Journal of Food Process Engineering **19** (1996) 445–456.

surface conditions were reported by Lue *et al.* (1991). Significant correlations between color properties and product breaking strength can be obtained from the experimental data included in Lue *et al.* (1994).

Since geometric structure and, at least to some degree, the physical properties of wall solids can be indicated by visually discernable characteristics, it is a logical hypothesis that texture-related mechanical properties of expanded food products can be evaluated by image processing. In this part of the research, frequently used mechanical properties of the test product were measured through shear and compression tests on an Instron universal testing machine. Image features in texture and color were used to describe the mechanical properties.

PROCEDURES

Specimen Preparation

The expanded product samples had a roughly cylindrical shape. For shear tests, forces were applied in the lateral direction; thus the samples required no further preparation except for dehydration. For compression tests in the axial direction, the samples needed to be cut into equal-length segments with ideally parallel top and bottom surfaces. Many methods were tested to cut the samples to minimize alterations to their physical structures. The easiest and most satisfactory method found was to use a high-speed grinder to trim the samples. Twenty samples per set (12 sets in all) were ground into 10-mm long cylindrical segments as specimens for compression tests. Before testing, all specimens, trimmed for compression and untrimmed for shear, were dehydrated at 90C for 24 h.

Instron Measurements

Both shear and compression tests were performed at a constant strain rate on an Instron Model-1132 testing machine. Shear tests were conducted by using a pair of blades to shear a specimen in the lateral direction. Such tests mimic biting of the product with incisors. Compression tests were done with a pair of parallel plates applying a force in the axial direction of a specimen. Compression tests simulate crushing of the product by molars.

The result of each Instron test was a curve of force versus displacement. The diameter of every specimen was measured and all specimens used for compression were 10-mm long. From these dimensions, force-displacement relationships were converted into stress-strain relationships. Though the measured curves varied from sample to sample to a great degree, the general shapes of shear and compression curves were as depicted in Fig. 1.

Many mechanical properties of a specimen can be derived from its stress-strain relationship. The following five characteristics were computed from

each shear or compression test as mechanical properties of the product samples (Fig. 1):

(1) τ_f for shear or σ_f for compression - Failure stress or breaking strength, the stress at which a specimen started to fail,
(2) E - Young's modulus of elasticity, the slope of the initial elastic section (line a-b in Fig. 1),
(3) β - Failing rate (or failing modulus), which is the slope of the curve right after the initial failure (line c-d),
(4) W - Destruction work, which is the area under the curve, and
(5) ϵ_f - Failure strain.

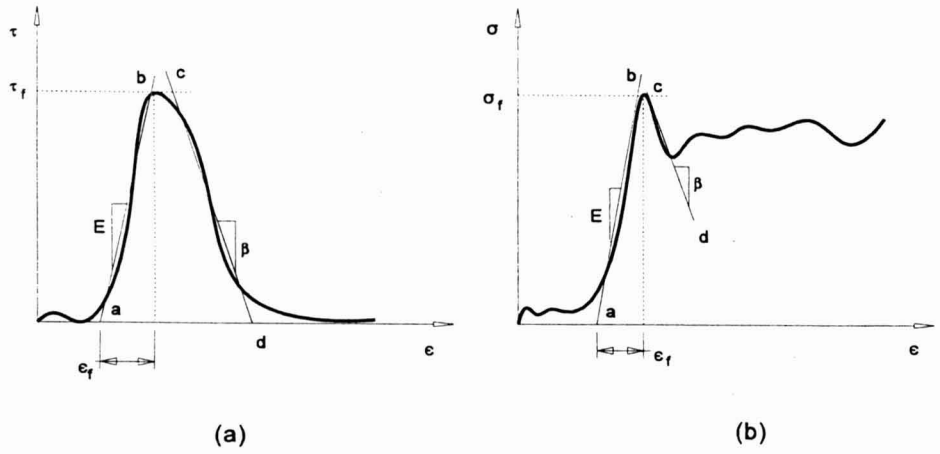

FIG. 1. ILLUSTRATION OF STRESS-STRAIN CURVES FROM INSTRON TESTS AND DEFINITION OF MECHANICAL PROPERTIES:
(a) Shear, (b) Compression

Breaking strength τ_f or σ_f indicates how difficult it is to break a specimen; so it is a measure of product hardness. Young's modulus E shows how resistive a specimen is to deformation under stress or force; thus it indicates such sensory attributes as brittleness, crispness and hardness. Failing rate β signifies how rapidly a specimen loses its ability to sustain force after the initial failure; hence it shows how cohesive, fracturable, crisp or brittle a sample is. Destruction work W is the mechanical work needed per unit sample volume to destroy the physical structure of a specimen. For a shear test, destruction refers to complete dissecting of a specimen, and for a compression test, it is complete crushing. W

is then an indicator of how difficult a sample can be chewed, encompassing hardness, cohesiveness and crispness, etc. As a result of densification, compression curves do not diminish to zero stress after failure (Fig. 1b); therefore, destruction work W was computed to a fixed strain value beyond failure for all samples. Although failure strain ϵ_f is theoretically a duplicate measure of failure stress and Young's modulus, an exact relationship among the three does not always apply because of irregularities in the test curves. ϵ_f was therefore included as a direct measure of the maximum strain or deformation a sample could sustain before it broke. It is also a useful measure of brittleness.

As shown in Fig. 1, some low stress values were registered at low strain levels, especially for compression tests. This part of the curve was associated with the initial partial contact between a specimen and the testing plates or blades. Since the specimens for compression could not be made to have perfectly parallel top and bottom sides and the shear blades were not exactly in the shape of the specimen contour, there would always be a settling-in period when the relevant specimen area (cross-section) was not entirely stressed. The stress responses during this period were not representative of the overall properties of a sample and thus were disregarded.

Image Features

As discussed earlier, image texture features can indicate both the geometric structure and partly the wall solid properties, which collectively determine the mechanical properties of a sample. All the texture image features extracted and described in Part I were tested as indicators of mechanical properties.

Since color could show wall solid properties, some color features were included in the analysis. They were:

(1) μ_c - mean,
(2) σ_c - standard deviation, and
(3) M_{c3} - third moment.

The mean obviously indicates an average color characteristic. For example, the mean of hue represents the average color type and the mean of saturation shows the average fullness of color over a sample area. The standard deviation signifies the scatteredness or nonuniformity of a color function. The third moment measures the skewness or imbalance of a color function histogram.

Data Analysis

As discussed in Part I, the image texture features were computed from the intensity and saturation functions. The color features were computed from three image functions: hue, saturation and intensity. Both surface and cross-section

images were used. The image feature values and Instron measurements were averaged over their replications (7 and 20, respectively). Correlation and regression analyses were performed to determine the usefulness of the image features in describing the mechanical properties of the product samples.

RESULTS AND DISCUSSION

Every image feature was computed from several potentially useful image functions of both surface and cross-section images and every computed feature value was used in the analysis. The highest correlation coefficient obtained for an image feature/mechanical property combination is presented in Tables 1 to 5. The image function that resulted in the highest correlation coefficient for each combination is noted in the tables.

Features from Edge Enhancement

The correlation coefficients between the features from edge enhancement and Instron mechanical properties are shown in Table 1. Overall, these features exhibited similar effectiveness in representing the mechanical properties. Each feature had an R value above or near 0.9 with at least one mechanical property. The levels of correlation and the mechanical property an image feature had the highest correlation with are clear from the table and require little further comment. A few interesting observations, however, can be made from Table 1.

The failing rate β for shear was highly correlated with almost all the image features, having an R value with σ_e up to 0.96. Because the image features in Table 1 primarily describe edge characteristics, these high correlations indicate that the shear failing rate heavily depended on the edge or wall structure of the samples. This also means that the wall structure had much influence on how cohesive and crisp a sample was.

As indicated by the subscripts on the R values in Table 1, there seems to be a mixture of image functions (intensity of surface images, saturation of cross-section images, etc.) that resulted in the highest correlation coefficients. The saturation function of surface images (designated by subscript c), however, appeared more often than others in Table 1, especially for shear tests; i.e., the surface saturation function gave more highest correlations than others. This is likely a consequence of the fact that the surface saturation function shows not only the cellular structure but also details of wall surface characteristics (Part I) which could reflect wall solid properties.

Shear work was little related to the image features from edge enhancement. This was also true for features developed with other methods, indicating that the work needed to dissect the product was not a simple function of visually discernable characteristics.

TABLE 1.
HIGHEST CORRELATION COEFFICIENTS[1] BETWEEN IMAGE FEATURES[2] FROM EDGE ENHANCEMENT AND INSTRON MEASUREMENTS[3]

	V_{max}	P_{max}	μ_e	σ_e	M_{e3}
			Shear test		
τ_f	0.64_c[4]	-0.85_c	0.86_c	-0.79_b	0.76_a
E	0.84_c	-0.84_c	0.76_c	0.87_c	0.89_a
β	-0.79_c	0.94_c	-0.89_c	0.96_b	-0.95_a
W					
ϵ_f	-0.70_c	0.68_c	-0.58_c	-0.84_a	-0.84_a
			Compression test		
σ_f	0.85_a	-0.78_a	0.75_a	0.60_d	0.65_c
E	-0.72_d	-0.67_a		-0.81_b	-0.82_b
β	-0.60_a		-0.59_a		
W	0.91_a	-0.87_a	0.79_a	0.75_d	0.78_c
ϵ_f	0.70_b	-0.88_b	0.62_b	0.91_d	-0.91_b

[1] Correlation coefficients with $p>0.05$ are omitted.

[2] Image features: V_{max} - pixel value of most occurrence, P_{max} - maximum frequency, μ_e - mean, σ_e - standard deviation, M_3 - third moments about origin.

[3] Properties from Instron measurements: τ_f, σ_f - breaking strength, E - Young's modulus, β - failing rate, W - destruction work, and ϵ_f - failure strain.

[4] Subscript denotes image function giving the highest correlation for the feature/property combination: a - intensity of surface images, b - intensity of cross-section images, c - saturation of surface images, or d - saturation of cross-section images.

For geometric properties, the signs of correlation between image features and instrumental measurements could be consistently explained in terms of cell size and other geometric considerations. For mechanical properties, such consistencies did not exist. An obvious reason for this is that mechanical properties do not depend only on geometric structure. The physical properties of wall solids affect both the mechanical behavior and image texture of a sample in a complex manner. This makes it difficult to interpret the signs of correlation coefficients or trend relationships between the image features and mechanical properties.

Features from Edge Segmentation

Table 2 shows the correlation coefficients between the image features extracted from edge segmentation and Instron measurements. Both total edge length L_e and nominal cell size S were highly correlated with several mechanical properties with R values up to 0.96. Since these two features had generally high correlations with breaking strength, Young's modulus and failing rate for shear,

and destruction work and failure strain for compression, they would be good indicators of hardness, brittleness and cohesiveness.

The features from edge segmentation were generally useful for representing both geometric (Part I) and mechanical properties. This shows that edge segmentation was an effective approach for texture feature extraction of expanded food products. The image functions yielding the highest correlations were well mixed, signifying the applicability of the approach to different color functions of both surface and cross-section images.

TABLE 2.
HIGHEST CORRELATION COEFFICIENTS[1] BETWEEN IMAGE FEATURES[2] FROM EDGE SEGMENTATION AND INSTRON MEASUREMENTS[3]

	L_E	S
	Shear test	
τ_f	0.87_b[4]	-0.85_b
E	0.90_c	-0.85_c
β	-0.94_c	0.96_c
W		
ϵ_f	-0.78_c	-0.79_a
	Compression test	
σ_f	0.80_a	-0.67_a
E	-0.73_d	-0.75_a
β		
W	0.90_a	-0.80_a
ϵ_f	0.90_b	-0.91_b

[1] Correlation coefficients with $p > 0.05$ are omitted.
[2] Image features: L_e - total edge length, S - nominal cell size.
[3, 4] See Table 1 for notations.

Features from Pixel Value Band Run Length

Table 3 shows the correlation coefficients between the features extracted from pixel value band run lengths and Instron measurements. An immediate observation from Table 3 is that the features gave approximately equal correlation coefficients for the three values used for band thickness T (8, 10 and 12 pixels). Though band thickness resulted in some noticeable differences in correlations with geometric properties (Table 3, Part I), these differences were not significant for mechanical properties. This agrees with the fact that the

mechanical behavior is not determined by the geometric structure alone. When the band thickness changed, the level of textural details revealed by the image features varied, possibly gaining information about one of the two aspects (structural or physical properties) and losing information about the other.

The run length features had generally higher correlation with properties for shear than with those for compression. They were most effective in representing failing rate for shear and failure strain for compression, which are properties relating to product brittleness and cohesiveness.

TABLE 3.
HIGHEST CORRELATION COEFFICIENTS[1] BETWEEN IMAGE FEATURES[2] FROM PIXEL VALUE BAND RUN LENGTH AND INSTRON MEASUREMENTS[3]

	μ_{r8}	σ_{r8}	μ_{r10}	σ_{r10}	μ_{r12}	σ_{r12}
			Shear test			
τ_f	-0.84_d[4]	-0.84_d	-0.83_d	-0.83_d	-0.83_d	-0.82_d
E	0.85_b	0.86_b	0.89_b	0.89_b	0.90_b	0.90_b
β	0.95_d	0.95_d	0.95_d	0.95_d	0.95_d	0.95_d
W						
ϵ_f	-0.87_b	0.88_b	-0.87_b	-0.88_b	-0.89_b	-0.89_b
			Compression test			
σ_f	-0.67_a	-0.64_a	-0.64_a	-0.61_a	-0.63_a	-0.61_a
E	-0.73_b	-0.73_b	0.72_b	-0.73_b	-0.73_b	-0.73_b
β						
W	-0.79_a	-0.77_a	-0.76_a	-0.74_a	-0.77_a	-0.74_a
ϵ_f	-0.91_b	-0.91_b	-0.90_b	-0.90_b	-0.89_b	-0.90_b

[1] Correlation coefficients with $p > 0.05$ are omitted.
[2] Image features: μ_{rn} - mean run length, σ_{rn} - standard deviation of run length, where subscript n denotes band thickness T in number of pixels.
[3, 4] See Table 1 for notations.

Though their physical meanings and implications require further studies, it is interesting to note a few consistencies in the usefulness of the image functions for the run length features. The highest correlation coefficients for shear were given by the cross-section images (either intensity or saturation functions as denoted by subscript b or d) whereas the those for compression were given by the intensity functions (either surface or cross section images as denoted by subscript a or b). The shear strength and failing rate were best indicated by features from saturation of cross-section images, modulus and failure strain for both shear and compression best represented by features from intensity of

cross-section images, and compression strength best described by features from intensity of surface images.

Features from Pixel Value Spatial Dependence

The correlation coefficients between features from pixel value spatial dependence for D = 16 and Instron measurements are shown in Table 4. One important point to note about these features is that they were correlated to a reasonable degree (R = 0.71 ~ 0.80) with failing rate β for compression. This property was not significantly correlated with almost all the edge and run length features. This indicates that β for compression was dependent more on the spatial arrangement of walls as characterized by the spatial dependence features than on the amount of walls as described by the edge and run length features. Overall, the entropy feature (F_9) seems less useful than others.

TABLE 4.
HIGHEST CORRELATION COEFFICIENTS[1] BETWEEN IMAGE FEATURES[2] FROM PIXEL VALUE SPATIAL DEPENDENCE (D = 16) AND INSTRON MEASUREMENTS[3]

	F_1	F_2	F_3	F_4	F_5
			Shear test		
τ^f	0.75_b[4]	0.70_d	-0.70_d	0.64_c	
E	0.68_b	0.87_d	-0.70_b	0.85_d	-0.63_b
β	-0.84_b	-0.92_d	0.86_d	0.88_c	0.75_b
W					
ϵ_f	0.59_d	-0.86_b	0.80_b	-0.88_d	-0.67_c
			Compression test		
σ_f	0.81_C		0.74_a	0.89_a	-0.72_C
E				-0.64_A	
β	0.74_C	-0.71_C	0.80_a	0.78_a	-0.73_C
W	0.90_C	-0.70_C	0.86_a	0.95_a	-0.81_c
ϵ_f	0.80_c	-0.88_c	0.89_a	0.86_c	-0.74_c

[1] Correlation coefficients with $p > 0.05$ are omitted.
[2] Image features: F_1 - angular second moment, F_2 - difference moment, F_3 - correlation, F_4 - variance, and F_9 - entropy.
[3, 4] See Table 1 for notations.

Color Features

Table 5 shows the correlation coefficients of the color features with Instron measurements. It is worth of noting that the mean (μ_c) and standard deviation (σ_c) of color functions had generally significant correlation with all the mechanical properties but shear work. Both were highly correlated with failing

rate for shear and failure strain for compression (R values up to 0.97). The third moment (M_{c3}) turned out to be a less useful feature.

The mean and standard deviation of a color function respectively show the average color and color variation in a sample area. These two features, especially the mean, carry little information about the geometric structure of a sample; therefore, their significant correlations with mechanical properties imply that color show the physical properties of wall solids as discussed earlier.

TABLE 5.
HIGHEST CORRELATION COEFFICIENTS[1] BETWEEN IMAGE FEATURES[2] FROM COLOR AND INSTRON MEASUREMENTS[3]

	μ_c	σ_c	M_{c3}
		Shear test	
τ_f	0.79_b[4]	0.77_e	
E	0.87_b	0.83_e	0.61_a
β	-0.97_b	0.95_e	0.69_c
W			
ϵ_f	0.91_d	-0.83_b	-0.76_a
		Compression test	
σ_f	-0.78_f	0.84_a	-0.75_b
E	0.85_d	-0.79_e	-0.82_a
β	0.64_f	0.66_d	0.59_b
W	-0.81_f	0.86_a	-0.77_b
ϵ_f	0.93_d	-0.90_e	-0.76_a

[1] Correlation coefficients with $p > 0.05$ are omitted.
[2] Image features: μ_c - mean, σ_c - standard deviation, M_{c3} - third moment.
[3] See Table 1 for mechanical property notations.
[4] Subscript denotes image function giving highest correlation for the feature/property combination: a - intensity of surface images, b - saturation of surface images, c - hue of surface images, d - intensity of cross-section images, e - saturation of cross-section images, or f - hue of cross-section images.

Regression of Mechanical Properties vs. Image Features

As each mechanical property was highly correlated with several image features, regression relationships of the mechanical properties versus the image features can be easily developed. For example, by simply using one image texture feature and one color feature that exhibited high linear correlations with a mechanical property, the SAS backward elimination procedure gave the significant independent variables and R^2 values as shown in Table 6.

Though only two image variables were used and the order of terms was limited to 2, regression analysis resulted in very high R^2 values, with three reaching 0.99 and the lowest being 0.82. This further demonstrates the usefulness of the image features extracted in representing and describing the mechanical properties of expanded food products. Both the image texture and color features appeared in every regression relationship, verifying the initial hypothesis that the two types of features are respectively related with two different aspects of an expanded food product (geometric structure and wall-solid properties), both of which contribute to the mechanical behavior of the product.

TABLE 6.
REGRESSION OF MECHANICAL PROPERTIES VERSUS IMAGE FEATURES

Mech. property[1] (Dependent Var.)	Image features[2] (Independent variable)	R^2-value
Shear		
τ_f	$L_e\mu_c$, μ_c^2	0.82
E	μ_{r12}, $\mu_{r12}\mu_c$, μ_c^2	0.99
β	σ_e, μ_c, σ_e^2, μ_c^2	0.99
ϵ_f	μ_{r12}, $\mu_{r12}\mu_c$	0.90
Compression		
σ_f	μ_c, F_4^2	0.93
E	M_{e3}, μ_c, $M_{e3\mu c}$, M_{e3}^2	0.90
β	F_3, σ_c, $F_3\sigma_c$, F_3^2	0.89
W	F_4, $F_4\sigma_c$, σ_c^2	0.96
ϵ_f	L_e, μ_c, $L_e\mu_c$, L_e^2, μ_c^2	0.99

[1] See Table 1 for notations of mechanical properties.
[2] See Tables 1-5 for notations of image features.

CONCLUSIONS

Mechanical properties of expanded food products were highly correlated with the image texture and color features extracted in this research. The image texture features effectively revealed geometric or structural characteristics while the color features were related with the physical properties of wall solids. Frequently used mechanical properties could be effectively represented by the image features.

How rapidly an expanded food sample fails under stress (cohesiveness and crispness) depended heavily on its geometric structure as revealed by the edge features, but the shear work associated with dissecting the product was little

related to visually discernable characteristics. The surface saturation function contained much useful information on product mechanical behavior since it depended on both the product cellular structure and wall solid properties. Image features derived from edge segmentation were useful to indicate hardness, brittleness and cohesiveness. The pixel value band run length approach produced features having generally high correlation with most of the mechanical properties measured. The failing rate for compression was best indicated by features characterizing spatial arrangement of walls.

Both the geometric and mechanical aspects of expanded-food texture can be effectively analyzed through processing of product surface and cross-section images. Image processing is a convenient and consistent way to characterize, quantify and predict textural attributes of expanded food products.

REFERENCES

BARRETT, A.H., CARDELLO, A.V., LESHER, L.L. and TAUB, I.A. 1994. Cellularity, mechanical failure, and textural perception of corn meal extrudates. J. Texture Studies *25*, 77–95.

BARRETT, A.H. and PELEG, M. 1992. Extrudate cell structure-texture relationships. J. Food Sci. *57*, 1253–1257.

JIN, Z., HSIEH, F. and HUFF, H.E. 1994. Extrusion cooking of corn meal with soy fiber, salt, and sugar. Cereal Chem. *71*(3), 227–234.

LUE, S., HSIEH, F. and HUFF, H.E. 1991. Extrusion cooking of corn meal and sugar beet fiber: effects on expansion properties, starch gelatinization, and dietary fiber content. Cereal Chem. *68*(3), 227–234.

LUE, S., HSIEH, F. and HUFF, H.E. 1994. Modeling of twin-screw extrusion cooking of corn meal and sugar beet fiber mixtures. J. Food Eng. *21*, 263–289.

SZCZESNIAK, A.S. 1963. Classification of textural characteristics. J. Food Sci. *28*, 385–389.

OPTIMIZATION OF PROTEIN PRECIPITATION IN ACID WHEY OBTAINED FROM SMALL RUMINANT'S MILK

MANUELA E. PINTADO and F. XAVIER MALCATA[1]

Escola Superior de Biotecnologia
Universidade Católica Portuguesa
Porto, Portugal

Accepted for Publication January 14, 1996

ABSTRACT

Attempts to maximize the precipitation yield of the major proteins via thermal processing of whey obtained from milks of Portuguese native breeds of ewes and goats was done using heating time, heating temperature, and stirring rate as independently manipulated variables. The experiments were planned according to a full factorial design with eight corner points, six axial points, and three replicated center points. Assessment of the fractions of β-lactoglobulin and α-lactalbumin removed by precipitation was done by gel filtration chromatography. The loci of the values of each manipulated variable (when the remaining two are fixed) which lead to critical points were obtained for both proteins, and the nature of such points was found. Comparative evaluation of the various loci has indicated that maxima for the precipitation of α-lactalbumin and β-lactoglobulin from both whey sources exist. However, a maximum value for the selectivity of precipitation of β-lactoglobulin relative to that of α-lactalbumin (within physically realizable conditions and without extrapolation from the experimental range covered) exists only for goat's whey (at a temperature of ca. 92C, heating time of ca. 46 min, and stirring rate of ca. 79 r.p.m.).

INTRODUCTION

Temperature is the single most important environmental factor influencing the structure and behavior of whey proteins, and has been extensively studied by a variety of authors (e.g., Shahani and Sommer 1951; Larson and Roleri 1954; Townend and Gyuricsek 1974; Hill *et al.* 1982; Manji and Kakuda 1986; Hill and Irvine 1988; Pearce 1989; Parris *et al.* 1991) namely for the recovery of such proteins from the whey proper; it has also been well established that the whole process of precipitation consists of sequential steps of protein denaturation

[1] Correspondence address: Dr. F. Xavier Malcata, Assistant Professor, Escola Superior de Biotecnologia, Rua Dr. António Bernardino de Almeida, 4200 Porto, Portugal.

and aggregation, where the former is clearly the rate-limiting and the more heat-labile step.

Although bulk precipitation of all whey proteins is in order if the goal is to obtain animal feed additives, selective precipitation of such proteins may be interesting if higher added-value applications are sought (e.g., fortification of human foods). Although such processing factors as pH and ionic strength of the whey have been related to heat precipitation of cow's whey proteins (Guy *et al.* 1963; Hill *et al.* 1985; Hill and Irvine 1988; Xiong *et al.* 1993), very few studies have focused on the characterization of the thermal precipitation of proteins from goat's and ewe's wheys (Ramos 1978; Calvo *et al.* 1989).

The reasons for this study were (1) to provide a deeper insight into the effects of three thermal processing variables, viz. heating temperature (related to the level of random molecular kinetic energy), heating time (related to the amount of random molecular kinetic energy transported), and stirring rate (related to the rate of transport of random molecular kinetic energy), on the degree of precipitation of β-lactoglobulin and α-lactalbumin, and (2) to eventually obtain conditions leading to maxima of the precipitation yield of either of these proteins, and maxima of the ratio of the precipitation yield of one to the precipitation yield of the other protein. (Both pH and ionic strength were not deliberately included in this study because they cannot be considered thermal variables and because their control at the farmer's manufacture level is not practically feasible given the facilities normally available.)

MATERIALS AND METHODS

Reagents

Milk from Bordaleira ewes and milk from Alpina goats was collected from preselected herds and used throughout the experiments in our laboratory. Protein standards from cow's milk, immunoglobulin G (IgG), blood serum albumin (BSA), α-lactalbumin (α-La), and β-lactoglobulin (β-Lg) were obtained from Sigma (USA). Hydrochloric acid, sodium chloride, di- and monosodium phosphate, and sodium azide were purchased from Merck (Germany).

Equipment

The heat treatments were performed using a controlled temperature, stirred bath from Julabo (Germany). The FPLC™ gel filtration chromatographic system by Pharmacia (Sweden) was employed for the quantitation of soluble proteins; this system was used in a configuration including two P-500 positive displacement pumps, an electrically-powered MV-7 motorized valve, a gel filtration column Superose 12 HR 10/30, a UV1 single path spectrophotometer monitor, a REC-102 double channel recorder, and a LCC-500 controller. Separation of

the supernatant whey from the precipitate following thermal treatment was performed using a centrifuge from Dupon (USA).

Preparation of Whey

The whey was obtained by acid precipitation of the caseins in the milks of both breeds of small ruminants using 1 M hydrochloric acid added to a final pH of 4.6, followed by heating at 46C for 10 min, cooling to room temperature, and centrifugation at 7,000 rpm for 15 min at 4C.

Application of Heat Treatments

Unreplicated experiments were performed at all possible combinations of two levels of temperature (85 and 95C), two levels of stirring rate (0 and 100 r.p.m.), and two levels of heating time (30 and 60 min). An extra experimental point at 90C, 50 r.p.m., and 45 min replicated three times was further included in the initial factorial design. As discussed below, this design was later added with six unreplicated experiments laid as axial points (see Table 1). In each experiment, 10 mL of either type of whey were submitted to the heat treatment in question in a test tube, and following completion of this treatment the tube was cooled and the supernatant removed by centrifugation at 7,000 rpm for 15 min. The supernatant was then frozen for further protein analyses.

Quantitation of Whey Proteins

Aliquots of 100 μL of the supernatant whey following heat treatment were injected in the gel filtration system and eluted with a phosphate buffer (pH 7.0) containing 0.5 M sodium chloride and 0.2 g/L sodium azide included as a preservative. Both samples and buffer were filtered through 0.22 μm filter paper, and the buffer was also degassed prior to chromatographic analysis. The buffer flow rate used was 0.4 mL/min. In order to locate the two major soluble proteins in the whey of the small ruminants, standards of bovine IgG, BSA, α-La, and β-Lg (the only standards commercially available) were used in a qualitative fashion. The precipitation yield of either α-La or β-Lg of ewe's and goat's wheys, P_i, was calculated via

$$P_i = \frac{A_{i,0} - A_i}{A_{i,0} - A_{i,\infty}} \times 100 \qquad (1)$$

where $A_{i,0}$, A_i, and $A_{i,\infty}$ are the integration areas (absorbance $\times$ time) of the i-th protein in soluble form in the whey before application of thermal treatment, after application of thermal treatment, and after application of an extreme heat treatment (sufficiently severe that higher temperatures or heating times do not

TABLE 1.
EXPERIMENTAL CONDITIONS FOR HEATING TIME (t), TEMPERATURE (T), AND STIRRING RATE (s); AND RESULTING DATA OBTAINED FOR THE FRACTIONAL PRECIPITATION OF β-LACTOGLOBULIN AND α-LACTALBUMIN FROM EWE'S AND GOAT'S WHEYS UPON THERMAL TREATMENT

							ewe's whey		goat's whey	
	t	x_1	T	x_2	s	x_3	β-Lg	α-La	β-Lg	α-La
	30	-1	85	-1	0	-1	14.7	19.6	4.70	17.0
	30	-1	85	-1	100	+1	16.3	22.4	29.5	35.3
	30	-1	95	+1	0	-1	98.3	72.0	81.2	61.6
C	30	-1	95	+1	100	+1	98.7	70.2	93.6	64.3
	60	+1	85	-1	0	-1	31.5	46.4	1.0	17.1
	60	+1	85	-1	100	+1	29.8	44.6	32.2	41.7
	60	+1	95	+1	0	-1	98.7	82.2	74.9	58.6
	60	+1	95	+1	100	+1	98.6	90.4	85.4	60.6
	45	0	90	0	50	0	94.3	74.1	27.3	22.3
c	45	0	90	0	50	0	94.7	71.4	30.1	17.5
	45	0	90	0	50	0	94.8	73.7	25.8	17.5
	30	-1	90	0	50	0	88.3	61.3	18.5	9.5
	60	+1	90	0	50	0	99.1	72.8	43.5	24.5
	45	0	85	-1	50	0	25.0	31.3	24.8	35.1
ax	45	0	95	+1	50	0	93.2	83.3	92.1	64.3
	45	0	90	0	0	-1	92.5	73.5	30.9	26.9
	45	0	90	0	100	+1	96.5	81.9	31.9	22.4

Note: **ax** - axial points; **c** - Center points; **C** - corner points; x_1 - Normalized value of heating time, defined as (**t**-45)/15, where **t** is expressed in min; x_2 - Normalized temperature, defined as (**T**-90)/5, where **T** is expressed in °C; x_3- Normalized stirring rate, defined as (**s**-50)/50 where **s** is expressed in r.p.m.

lead to further precipitation yields), respectively. (The value of $A_{i,\infty}$ was negligible when compared with $A_{i,0}$.) It is important to remember that, in the range where Beer's law is valid (as was the case with the supernatant wheys obtained in all our experiments), the spectrophotometric detector of the chromatographic system responds linearly with the concentration of the absorbing species in question, C_i (i.e. $A_i = a + bC_i$, where a and b constants), and so Eq. (1) may, for convenience, be replaced by

$$P_i = \frac{C_{i,0} - C_i}{C_{i,0} - C_{i,\infty}} \times 100 \qquad (2)$$

where $C_{i,0}$, C_i, and $C_{i,\infty}$ are the molar concentrations of the i-th protein in

soluble form in the whey before application of thermal treatment, after application of thermal treatment, and after application of a similar extreme heat treatment, respectively.

RESULTS AND DISCUSSION

First Order Design Model

The experimental results in terms of precipitation yields for the starting 2^3 factorial design with one replicated center point are depicted in Table 1. The model to be fitted by linear regression analysis reads

$$\hat{y}=\bar{y}+a_1x_1+a_2x_2+a_3x_3 \tag{3}$$

where $\hat{y}$ is the fitted response, $\bar{y}$ is the average of all data, and the a's are adjustable parameters. The x's are the manipulated variables in coded, normalized form: x_1 is the normalized value for the heating time, t, and is defined as (t-45)/15, where t is expressed in min; x_2 is the normalized value for the temperature, T, and is defined as (T-90)/5, where T is expressed in °C; and x_3 is the normalized value for the stirring rate, s, defined as (s-50)/50, where s is expressed in r.p.m.

Estimates of the sums of all quadratic effects associated with the form of Eq. (3), obtained as outlined elsewhere (Box *et al.* 1978), were -17 ± 2 for α-La and -33.8 ± 0.4 for β-Lg from ewe's whey, and 25 ± 4 for α-La and 19 ± 9 for β-Lg from goat's whey (the 95% confidence intervals were obtained using the variance of the center replicates as estimator for the standard deviation). In view of this diagnostic, one concluded that second order effects were likely to be of importance, and so the experimental design was expanded accordingly.

Second Order Design Model

The experimental results in terms of precipitation yields for the 2^3 factorial design with one replicated center point and six axial points are depicted in Table 2. The model to be fitted by linear regression analysis reads

$$\begin{aligned}\hat{y}=\bar{y}+b_1x_1+b_2x_2+b_3x_3+\ldots\\ \ldots b_{11}x_1^2+b_{22}x_2^2+b_{33}x_3^2+\ldots\\ \ldots b_{12}x_1x_2+b_{13}x_1x_3+b_{23}x_2x_3\end{aligned} \tag{4}$$

where the b's are adjustable parameters. Linear regression techniques were employed to compute all such adjustable parameters, and the results are tabulated in Table 2. Differentiating Eq. (4) with respect to x_1 or x_2 or x_3 at a

TABLE 2.

SECOND ORDER EXPERIMENTAL DESIGN FOR HEATING TIME (t), TEMPERATURE (T), AND STIRRING RATE (s); VALUES OF MAIN LINEAR EFFECTS (x_1, x_2, AND x_3), MAIN QUADRATIC EFFECTS (x_1x_1, x_2x_2, AND x_3x_3), AND INTERACTIONS (x_1x_2, x_1x_3, AND x_2x_3) WITH ASSOCIATED 95% CONFIDENCE INTERVALS.

		E&I									
	U	avg	x_1	x_2	x_3	x_1x_1	x_2x_2	x_3x_3	x_1x_2	x_1x_3	x_2x_3
C	1	+1	-1	-1	-1	+1	+1	+1	+1	+1	+1
	2	+1	-1	-1	+1	+1	+1	+1	+1	-1	-1
	3	+1	-1	+1	-1	+1	+1	+1	-1	+1	-1
	4	+1	-1	+1	+1	+1	+1	+1	-1	-1	+1
	5	+1	+1	-1	-1	+1	+1	+1	-1	-1	+1
	6	+1	+1	-1	+1	+1	+1	+1	-1	+1	-1
	7	+1	+1	+1	-1	+1	+1	+1	+1	-1	-1
	8	+1	+1	+1	+1	+1	+1	+1	+1	+1	+1
c	9	+1	0	0	0	0	0	0	0	0	0
	10	+1	0	0	0	0	0	0	0	0	0
	11	+1	0	0	0	0	0	0	0	0	0
ax	12	+1	-1	0	0	+1	0	0	0	0	0
	13	+1	+1	0	0	+1	0	0	0	0	0
	14	+1	0	-1	0	0	+1	0	0	0	0
	15	+1	0	+1	0	0	+1	0	0	0	0
	16	+1	0	0	-1	0	0	+1	0	0	0
	17	+1	0	0	+1	0	0	+1	0	0	0
ewe's whey	β-Lg	93.9880	4.1400	37.0200	0.4200	0.1755	-34.4282	0.9730	-3.7500	-0.4750	0.0500
		±0.2068	±0.2996	±0.2996	±0.2996	±0.2996	±0.2996	±0.2996	±0.3585	±0.3585	±0.3585
	α-La	73.0553	9.0900	23.3800	1.5800	-5.9930	-15.7461	4.6550	-2.3250	0.6750	0.6750
		±1.1387	±1.6501	±1.6501	±1.6501	±1.6501	±1.6501	±1.6501	±1.9747	±1.9747	±1.9747
goat's whey	β-Lg	31.1308	0.9500	33.5000	7.9900	-2.6762	24.7716	-2.2778	-1.6875	0.5625	-4.1375
		±1.7055	±2.4715	±2.4715	±2.4715	±2.4715	±2.4715	±2.4715	±2.9577	±2.9577	±2.9577
	α-La	21.0447	1.4800	16.3200	4.3100	-5.5010	27.1972	2.1478	-1.6500	0.7000	-4.7750
		±2.1656	±3.1382	±3.1382	±3.1382	±3.1382	±3.1382	±3.1382	±3.7556	±3.7556	±3.7556

Note: **ax** - axial points; **c** - Center points; **C** - Corner points; **EE** - Estimated Effects; **E&I** - Effects (linear and quadratic) and Interactions (second order); **avg** - grand average; **U** - rUn; x_1 - Normalized value of heating time, defined as (**t**-45)/15, where **t** is expressed in min; x_2 - Normalized temperature, defined as (**T**-90)/5, where **T** is expressed in °C; x_3 - Normalized stirring rate, defined as (**s**-50)/50, where **s** is expressed in rpm.

time, and setting each result thus obtained equal to zero provides necessary conditions for optima to exist. The resulting three linear equations can, in turn, be algebraically solved with respect to x_1 or x_2 or x_3, respectively; the results in terms of loci of the optima when variables x_2 and x_3, or x_1 and x_3, or x_1 and x_2, respectively, are deliberately prefixed are depicted in Table 3. Differences appear, thus, to exist between the thermal behaviors of the whey originating from the two breeds of small ruminants considered.

Although a true global maximum exists for β-lactoglobulin in ewe's whey, the location of such mathematical optimum violates physical constraints and is well beyond the range chosen for experimentation; therefore, the actual maximum lies on an operational constraint. For α-lactalbumin of ewe's whey and for both major proteins in goat's whey no true local optima can be found.

A second analysis which can be carried out in view of the results depicted in Table 3 pertains to the conditions associated with a maximum value for the ratio of fractional precipitation of, say, β-Lg to α-La (i.e., $\hat{y}_\beta/\hat{y}_\alpha$). If such maximum existed, it should give the maximum selectivity of the thermal treatment in terms of protein precipitation, and should clearly be associated with a maximum for the numerator and a minimum for the denominator (differentiation of the ratio $\hat{y}_\beta/\hat{y}_\alpha$ with respect to each of the manipulated variables at a time and setting each condition equal to zero supports this assertion). Geometrically, this reasoning corresponds to finding the straight line resulting from the intersection of the two planes defined by every set of two relationships listed in each column of Table 3 for each source of whey (provided that the relationship in the first row corresponds to a maximum and the relationship in the second row corresponds to a minimum). For example, the maximum for such ratio in the case of goat's whey when x_3 is used as tentative independent variable is obtained from combination of $x_1 = 0.3344 - 0.8881\ x_2$ with $x_3 = 0.5376 + 0.1464\ x_2$. For the remaining situations, the loci of such optima violate physical constraints or lie outside the region $[-1,+1]$ for the (coded) manipulated variables, including those tentatively associated with a maximum for the ratio $\hat{y}_\alpha/\hat{y}_\beta$. Hence, only the situation described above is considered hereafter, and is plotted in Fig. 1. Inspection of this figure indicates that the maximum in terms of selectivity corresponds to nearly 50% more precipitation of β-lactoglobulin relative to α-lactalbumin, and is obtained when $x_1=0.041$, $x_2=0.330$, and $x_3=0.586$.

Physicochemical and Statistical Considerations

Inspection of Table 1 indicates that higher extents of precipitation occur for ewe's whey than for goat's whey under similar processing conditions. This observation is consistent with data reported by Ramos (1978) and Calvo *et al.* (1988) which indicate that ovine β-lactoglobulin is more sensitive to heat than their bovine or caprine counterparts.

TABLE 3.

LOCI AND TYPE OF OPTIMA FOR EVERY OPERATING VARIABLE (HEATING TIME, x_1, TEMPERATURE, x_2, AND STIRRING RATE, x_3) ASSOCIATED WITH THE SECOND ORDER MODELS FITTED TO THE DATA OBTAINED FOR THE FRACTIONAL PRECIPITATION OF THE MAJOR PROTEINS FROM EWE'S AND GOAT'S WHEYS.

		LO			TO		
		x_1	x_2	x_3	x_1	x_2	x_3
ewe´s whey	β-Lg	$2.6739 + 1.4281\ x_2 + 0.0304\ x_3$	$14.7065 + 1.1489\ x_1 + 1.1245\ x_3$	$0.9907 + 0.0071\ x_1 + 0.3265\ x_2$	max	max	max
	α-La	$0.3169 - 0.0128\ x_2 + 0.4472\ x_3$	$0.1783 + 0.0037\ x_1 + 0.0329\ x_3$	$11.9926 + 5.5817\ x_1 - 1.4353\ x_2$	min	max	min
goat´s whey	β-Lg	$-0.2499 + 0.0586\ x_2 - 0.0976\ x_3$	$-0.5311 + 0.0586\ x_1 - 0.2148\ x_3$	$0.5002 + 0.1117\ x_1 + 0.2456\ x_2$	min	min	max
	α-La	$-0.9079 + 0.2801\ x_2 + 0.4813\ x_3$	$-15.6687 + 12.1246\ x_1 + 5.9068\ x_3$	$0.6185 - 0.2421\ x_1 - 0.0686\ x_2$	max	max	min

Note: **LO** - Loci of Optima; **TO** - Type of Optima; x_1 - Normalized value of heating time, defined as (**t**-45)/15, where **t** is expressed in min; x_2 - Normalized temperature, defined as (**T**-90)/5, where **T** is expressed in °C; x_3 - Normalized stirring rate, defined as (**s**-50)/50, where **s** is expressed in r.p.m.

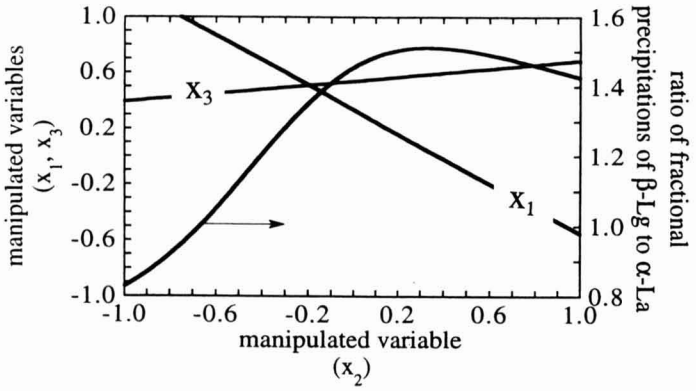

FIG. 1. OPTIMUM RATIO OF PRECIPITATION OF β-LACTOGLOBULIN TO α-LACTALBUMIN IN THE CASE OF GOAT'S WHEY, AND CORRESPONDING LOCI OF THE MANIPULATED PROCESSING VARIABLES

The existence of optima in terms of precipitation of the proteins in whey originating from small ruminants was somewhat expected in view of results reported by a variety of researchers. Hill *et al.* (1982) have shown that maximum protein recovery (predominantly α-lactalbumin and β-lactoglobulin) is obtained upon heating bovine milk to 95C for 5 min prior to acidification. Pearce (1983) has proven that the extents of precipitation increase with temperature, and that maximum precipitation of α-La and β-Lg occurs for pH in the vicinity of their isoelectric point. Dumay and Cheftel (1989) concluded that the precipitation of β-Lg increases with heating time, heating temperature, and pH of whey, as well as with overall protein concentration.

Temperature is the most important linear effect for both α-lactalbumin and β-lactoglobulin in ewe's whey (see Table 2), a conclusion which is in clear agreement with Pearce (1989). By the same token, heating time is less important, and stirring rate is the least important effect (for the case of α-La, its effect is virtually nil). The present results also agree with data available elsewhere (Pintado and Malcata 1994) pertaining to ewe's whey. All quadratic effects are important (at the 5% significance level) in the case of precipitation of α-lactalbumin, especially the temperature; in the case of β-lactoglobulin, the quadratic effect of heating time is not important. In terms of interactions, only the temperature-heating time crossed interaction is important (at the same level of statistical significance).

In the case of goat's whey, temperature is again the most important linear effect, but, interestingly, heating time has a negligible effect, whereas stirring rate still has a significant (at the 5% level), yet small effect associated with it. Temperature is also clearly the only meaningful quadratic effect. In what concerns the interactions, only the temperature-stirring rate interaction is relatively important.

The experimental results obtained suggest that there is a situation in which preferential precipitation of β-lactoglobulin relative to α-lactalbumin can be achieved by controlling the processing conditions during thermal processing. This possibility, which complements that reported by Kaneko *et al.* (1985) on the effect of addition of ferric chloride to whey, and that reported by Hill and Irvine (1988) on pH manipulation (it was shown that precipitation of α-lactalbumin following heat treatment at pH in the range 2.4-3.4 is greater than that of β-lactoglobulin, but the reverse holds at pH in the range 5.7-6.8), may be the scope of further consideration from a processing standpoint.

ACKNOWLEDGMENTS

Funding for author M.E. Pintado was provided by a fellowship issued within the framework of CIENCIA (BD-2526/93-IF) administered by JNICT (Portugal). Funding for the project was provided through research grants attributed by FLAD (Portuguese-American Foundation for Development) and project LIFE94/P/A125/P/01310/NOR (European Union program LIFE).

REFERENCES

BOX, G.E.P., HUNTER, W.G. and HUNTER, J.S. 1978. *Statistics for Experimenters*. John Wiley & Sons, New York.

CALVO, M.M., AMIGO, L., OLANO, L. and MARTIN, P.J. 1989. Effect of thermal treatments on the determination of bovine milk added to ovine or caprine milk. Food Chem. *32*, 99.

DUMAY, E. and CHEFTEL, J.C. 1989. Chauffage d'un concentré proteique de β-lactoglobuline en millieu faiblement alcalin. Effets sur la solubilité et le comportement chromatographique de la β-lactoglobuline et de α-lactalbumine. Science des aliments *9*, 561.

GUY, E.J., VETTEL, H.E. and PALLANSON, M.J. 1967. Denaturation of cottage cheese whey proteins by heat. J. Dairy Sci. *50*, 828.

HILL, A.R., BULLOCK, D.H. and IRVINE, D.M. 1982. Recovery of whey proteins from concentrated sweet whey. Can. Inst. Food Sci. Technol. J. *15*, 180.

HILL, A.R. and IRVINE, D.M. 1988. Effects of pH on the thermal precipitation of proteins in acid and sweet cheese wheys. Can. Inst. Food Sci. Technol. J. *21*, 386.

HILL, A.R., IRVINE, D.M. and BULLOCK, D.H. 1982. Precipitation and recovery of whey proteins: a review. Can. Inst. Food Sci. Technol. J. *15*, 155.

KANEKO, B.T., WU, B.T. and NAKAI, S. 1985. Selective concentration of bovine immunoglobulins and α-Lactalbumin from acid whey using $FeCl_3$. J. Food Sci. *50*, 1531.

LARSON, B.L. and ROLLERI, G.D. 1955. Heat denaturation of the specific serum proteins in milk. J. Dairy Sci. *38*, 351.

MANJI, B. and KAKUDA, Y. 1986. Thermal denaturation of whey proteins in skim milks. Can. Inst. Sci. Technol. J. *19*, 163.

PARRIS, N., PURCELL, J.M. and PTASHKIN, S.M. 1991. Thermal denaturation of whey proteins in skim milk. J. Agric. Food Chem. *39*, 2167.

PEARCE, R.J. 1983. Thermal separation of β-lactoglobulin and α-lactalbumin in bovine cheddar cheese whey. Aust. J. Dairy Technol. *38*, 144.

PEARCE, R.J. 1989. Thermal denaturation of whey proteins. Bull. Int. Dairy Fed. *238*, 17.

PINTADO, M.E. and MALCATA, F.X. 1994. Effect of thermal treatment on the protein profile of whey from ovine and caprine milk throughout lactation. Int. Dairy J. *6*, 497.

RAMOS, M. 1978. Effects of heating on the nitrogen fractions of ewe's, goat's, and cow's milk. p. 613. XXth International Dairy Congress. Paris.

SHAHANI, K.M. and SOMMYER, H.H. 1951. The protein and non-protein nitrogen fractions in milk. The effect of heat treatments and homogenization. J. Dairy Sci. *34*, 1035.

TOWNEND, R. and GYURICSEK, D.M. 1974. Heat denaturation of whey and model protein systems. J. Dairy Sci. *57*, 1152.

XIONG, Y.L., DAWSON, K.A. and WAN, L. 1993. Thermal aggregation of β-Lactoglobulin: effect of pH, ionic environment, and thiol reagent. J. Dairy Sci. *76*, 70.

EFFECTS OF pH ON THE ULTRAFILTRATION OF BOVINE SERUM ALBUMIN AT HIGH IONIC STRENGTH USING A MACROPOROUS TITANIA MEMBRANE

M. TRZEBIATOWSKA and A.R. SZANIAWSKI

Division of Water Environment Engineering
Technical University of Szczecin
Al. Piastów 50, 70-311
Szczecin, Poland

AND

H.G. SPENCER[1]

Department of Chemistry
Clemson University
Clemson, SC 29634-1905

Accepted for Publication March 19, 1996

ABSTRACT

The ultrafiltration of bovine serum albumin (BSA) buffered at pH 3.8, 4.8 and 6.8 in solutions with ionic strengths greater than 0.05 mol dm^{-3} was investigated at pressures of 0.20 and 0.70 MPa using a macroporous titania membrane. Protein rejections as high as 0.94 were obtained. Both pH and pressure affected the permeability and rejection. The relative amount of irreversible fouling was estimated by evaluating parameters of a resistance model. Conditions providing the lowest fouling index and the least irreversible fouling while retaining high BSA rejection were obtained at the highest pH, 6.8, and lowest pressure, 0.20 MPa.

INTRODUCTION

The ultrafiltration, or partially retentive microfiltration, of dilute protein solutions with macroporous titania membranes has been investigated at low ionic strength (Zhang and Spencer 1993). Separations of bovine serum albumin (BSA) and bovine gamma globulin from their mixtures were accomplished at low ionic

[1] Address correspondence to: H.G. Spencer, Department of Chemistry, Clemson University, Clemson, SC 29634-1905; Tel. (803) 656-5021.

Journal of Food Process Engineering **19** (1996) 469–478. *All Rights Reserved.*

strength and pressure by the partially retentive microfiltration at optimal values of the pH. The rejection of the proteins and the separation factor decreased significantly with increasing ionic strength. This investigation is concerned with the effect of pH and pressure on the rejection and flux of dilute BSA solutions at ionic strengths greater than the 0.02 mol dm^{-3} maximum previously investigated. The effect of pH was investigated because the isoelectric point (pI) of the titania microfiltration membrane is near pH 6.2 and the pI of BSA is 4.8. At pH 3.8, both the membrane and the BSA are positive in charge. At pH 4.8, the membrane is positive but the net charge on the BSA is near zero. At pH 6.8, both the BSA and the membrane are negative in charge. Of course, adsorption of BSA would alter the charge of the membrane so that it approached the charge sign of the BSA in solution at any pH. At the higher ionic strengths used in this investigation, 0.05 to 0.17 mol/dm^3, ultrafiltration results influenced by electrostatic repulsion between charged BSA species, and between a BSA species and the membrane that occur at low ionic strengths should be altered significantly. In the range of ionic strength used in the protein separation experiments, less than approximately 0.001 M, the electrokinetic radius for a 1:1 electrolyte solution is about 2.6 in a membrane with a pore radius of approximately 0.03μm (McGregor 1974). Electrostatic effects could be significant. However, the electrokinetic radius approaches 12 for a 0.02 M solution and becomes greater than 20 in the solutions used in this investigation. An electrokinetic radius this large suggests significant electrostatic effects between protein and pore in the rejection of the BSA at ionic strengths used in this investigation should be negligible.

MATERIALS AND METHODS

Membrane and Materials

The membrane used in the experiments was a titania microfiltration membrane permanently affixed to the inside surface of a porous sintered stainless steel tube. The module was a 1.6 cm ID tube providing an area of 0.025 m^2 enclosed in a stainless steel housing. The average pore radius in the titania layer is in the range of 0.03 to 0.05 μm (Trzebiatowska *et al.* 1996).

The BSA used in the experiments was albumin fraction V obtained from Sigma Chemical Co. (St. Louis, USA). All other compounds were reagent grade and the water was deionized with a mixed bed, MB-8, Amberlite ion exchanger.

Buffer solutions were prepared as described by Harrigan and McCance (1966). The ionic strengths of the dilute BSA solutions were essentially determined by the contribution of the buffer which varied with pH; 0.05 at pH 3.8, 0.08 at pH 4.8 and 0.17 mol dm^{-3} at pH 6.8. All ionic strengths are larger than previous experiments where the pH was obtained by addition of a minimum

amount of strong acid or base and were much less than 0.02 mol dm^{-3} except in experiments accomplished with electrolyte added to obtain 0.02 mol dm^{-3} (Zhang and Spencer 1993).

Ultrafiltration System and Procedures

The ultrafiltration system consisted of a feed tank, high pressure Tonkaflow pump, membrane module, pressure gauge at the outlet of the module, control valves before and after the module and in the line by-passing the module as shown schematically in Fig. 1. The temperature was controlled with a heat exchanger in the return line. Flows were measured by timed volume collection. The instantaneous rejection of BSA, r, was determined from the concentrations of permeate, c_p, and retentate, c_r, taken at the same time during the ultrafiltration experiments by $r = 1 - c_p/c_r$. The pressure, P, and crossflow velocity, u, were established with the control valves. Water permeability, ultrafiltration, water rinsing and chemical cleaning processes were run in the apparatus. All filtration and permeation experiments were conducted at 27C. The ultrafiltration experiments were effectively zero recovery; accomplished by returning the retentate and permeate from the membrane possessing a small area to the feed reservoir.

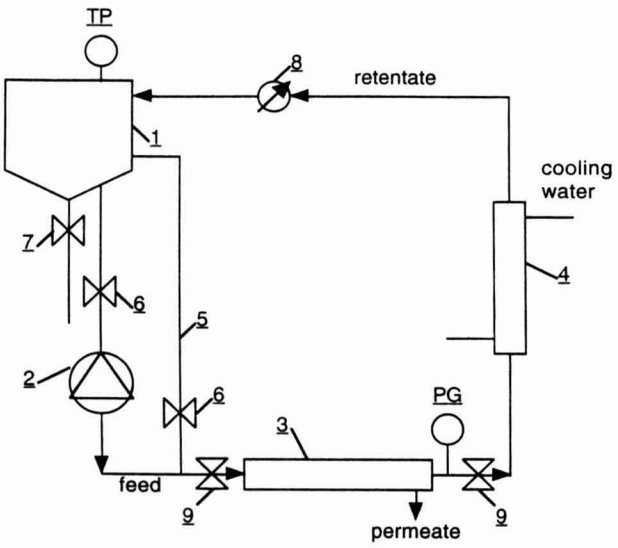

FIG. 1. SCHEMATIC DIAGRAM OF THE ULTRAFILTRATION SYSTEM
1-feed reservoir, 2-pump, 3-membrane module, 4-heat exchanger, 5-by-pass, 6-valve, 7-valve, 8-flow meter, and 9-ball valve

The experimental sequence consisted of the determination of the flux of water through the clean membrane as a function of pressure to 1.5 MPa in an increasing then decreasing pressure sequence, the ultrafiltration experiment with BSA, determination of the water permeability as a function of pressure after discharging and draining the BSA solution, chemical cleaning, and determination of the water permeability of the clean membrane as a function of pressure. The ultrafiltration experiments were run for 180 min at 27C with 1.00 g dm^{-3} BSA solutions buffered at pH 3.8, 4.8 and 6.8, crossflow velocity 2.0 m s^{-1}, and pressures of 0.20 and at 0.70 MPa.

The flux and concentration of BSA in the permeate and retentate were determined at intervals during the course of the experiment.

Analysis Procedures

The protein concentration was determined by a colorimetric method (Ellman 1964). Proteins and peptides in the presence of copper ions in an alkaline medium form a violet complex. The intensity of the absorbance at a wave length of 546 nm is directly proportional to the protein concentration. Absorbance measurements were accomplished with a SPECOL 11 spectrophotometer.

Membrane Cleaning

Following each ultrafiltration experiment, the BSA solution was discharged, the apparatus filled with water and the water permeability determined at increasing and decreasing pressures up to 1.5 MPa at 27C. The membrane was then cleaned by circulating a pH 11.5 NaOH solution for about 10 min, discharging this solution, circulating a dilute (about 0.2%) hydrogen peroxide solution for about 30 min with the temperature controlled to less than 45C, discharging this solution, circulating a pH 2.5 HNO_3 solution for 30 min with the temperature controlled to less than 45C, and determining the water permeability at increasing and decreasing pressures up to 1.5 MPa at 27C. This cleaning procedure either restored or slightly increased the original permeability to the membrane throughout the series of experiments.

Treatment of Data

The data consisted of the water flux of the clean membrane, J_{wb}, as a function of pressure; volume flux of the BSA solution, J, and rejection, r, of BSA as a function of time during the ultrafiltration experiment; water flux after the ultrafiltration experiment, J_{wa}; and the water flux after chemical cleaning, J_{wb}. These fluxes were converted to experimental resistances in the units of m^{-1} as $(P / \eta J_i)$, where η is the viscosity of water at 27C. Using a resistance model, the experimental resistances were converted to characteristic resistances, R_i, as

defined in Table 1 and based on the model described by Ko and Pellegrino (1992). Table 1 also contains equations relating experimental resistances to characteristic resistances.

TABLE 1.
DEFINITIONS OF EXPERIMENTAL AND CHARACTERISTIC RESISTANCE AND EQUATIONS

Experimental resistances:

$(P/\eta J_{wh})$	Resistance of the clean membrane to water, before the ultrafiltration experiment and after chemical cleaning following the ultrafiltration experiment
$(P/\eta J_x)$	Resistance to the BSA solution at the end of the ultrafiltration experiment
$(P/\eta J_{wa})$	Resistance of the membrane to water following the ultrafiltration experiment

Characteristic resistances:

R_m	Membrane resistance
R_f	Resistance of the irreversible fouling layer, i.e., the resistance not removed by the solution discharge and water rinse after the ultrafiltration experiment
π'	Normalized osmotic pressure difference, π, during the ultrafiltration experiment, representing all reduction of flux not accounted for by R_f, $\pi' \approx \pi/P$,
R_f'	Normalized resistance of the irreversible fouling layer

Equations relating characteristic resistances to experimental resistances:

$$R_m = (P/\eta J_{wh})$$
$$R_f = (P/\eta J_{wa}) - (P/\eta J_{wh})$$
$$R_x = (P/\eta J_x) = (R_m + R_f)/(1 - \pi')$$
$$R_f' = R_f/R_m$$

The dependence of J on P for water obtained after the ultrafiltration experiment was concave against the P axis, indicating some fouling during the water permeability experiments, probably the result of protein remaining in the system after the simple exchange of liquids accomplished by discharging and draining the solution used in the experiment and filling the system with water. The permeability of the water was estimated from these nonlinear plots by obtaining a second order equation in P for the dependence of J on P, taking its derivative and evaluating the limiting slope as P approached zero. To be consistent, a similar procedure was used for the dependence of J on P for water

with the clean membranes, although the J versus P dependence was nearly linear after the cleaning procedure. The reciprocal of the limiting permeability divided by the viscosity of water, i.e., the resistance, was calculated for each water permeability experiment.

A second order equation in time, t, describing J(t) for each ultrafiltration experiment was integrated over the time limits of the experiment, 0 to 180 min, to obtain the total volume of permeate produced, V_p(total).

RESULTS AND DISCUSSION

The volume flux, J, decreased with time during the BSA ultrafiltration experiments as shown in Fig. 2. The equations

$$J = J_c - b \ln t \text{ and } J/J_c = 1 - B \ln t \quad (1)$$

were used to describe the dependence of J on t where J_c is a characteristic flux obtained by extrapolating J/J_c versus ln t to ln t = 0, or t = 1 (min). Plots of J/J_c versus ln t for the ultrafiltration experiments are shown in Fig. 3. The coefficient B, i.e., the negative of the slopes of these plots of J/J_c versus ln t, represents a fouling index where B = 0 identifies no decrease in flux with time and an increase in B indicates an increase in the rate of the flux decline.

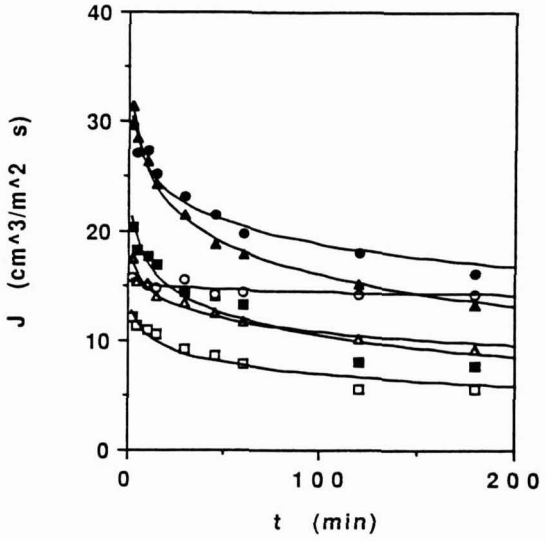

FIG. 2. J VS t
(empty symbols), P = 0.20 MPa; (filled symbols), P = 0.70 MPa; (circles), pH 6.8; (triangles), pH 4.8; and (squares) pH 3.8.

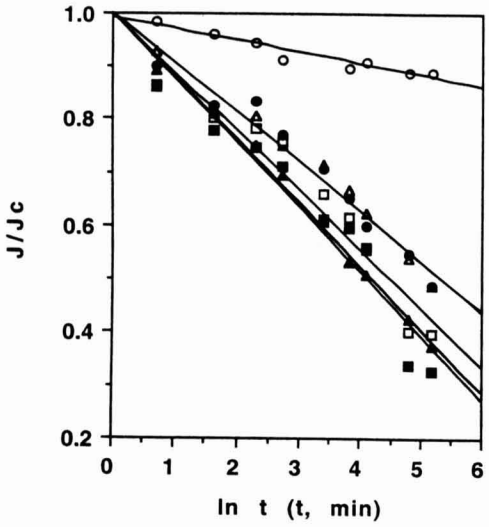

FIG. 3. J/J_c VS ln t
(empty symbols), P = 0.20 MPa; (filled symbols), P = 0.70 MPa; (circles), pH 6.8; (triangles), pH 4.8; and (squares) pH 3.8.

The values of B obtained from the slopes are given with standard deviations in Table 2. These values range from 0.09 to 0.12 for all experiments except the one at P = 0.20 MPa and pH 6.8, which is much smaller (0.021). The total volume of permeate obtained during the 180 min experiments, V_p(total), is also given in Table 2. The ultrafiltration experiments at P = 0.70 MPa produced larger total volumes of permeate in the experiments of 180 min duration than those at P = 0.20 MPa compared at the same pH even when the fouling indexes were higher.

The rejection of BSA increased during the course of each experiment suggesting that fouling plays a role in attaining high rejections with these macroporous membranes. The changes in rejection are indicated in Table 2, where the rejections at 5 min and at 180 min elapsed time of the experiment are provided. The amount of the increase was dependent on pressure and pH. The increase was smallest for the experiment at P = 0.70 MPa and pH 4.8, the pI of the protein, and largest for the experiment at the same pH, but at P = 0.20 MPa. The smaller increase in the rejection at the higher pressure at the pI of BSA is contrary to the greater increase at the higher pressure observed at pH one or more units removed from it. This result suggests that at the pI of the protein it is immobilized in the membrane pores at the lower pressure but remains mobile at the higher pressure in the associated higher convective flow rate.

TABLE 2.
FOULING INDEX, REJECTION AT 5 MIN AND THE FINAL REJECTION AT 180 MIN, AND TOTAL PERMEATE VOLUME PER SQUARE METER FOR THE ULTRAFILTRATION OF 1.0 g/L BSA WITH A TITANIA MEMBRANE AT u = 2.0 m/s, T = 300K FOR 180 MIN

Pressure (MPa)	pH	B (from J/J'vs ln t)	r(5 min)/r(180 min)	V_p(total) (dm^3/m^2)
0.20	6.8	0.021 ± 0.003	0.85/0.92	2.59
	4.8	0.093 ± 0.006	0.69/0.94	2.05
	3.8	0.11 ± 0.01	0.75/0.83	1.29
0.70	6.8	0.09 ± 0.02	0.76/0.94	3.58
	4.8	0.118 ± 0.004	0.79/0.81	3.17
	3.8	0.12 ± 0.01	0.80/0.92	2.17

The experimental resistances are provided in Table 3. The resistance of the chemically-cleaned membrane was $6.8 \pm 0.9 \times 10^{12}$ m^{-1}. The relative resistances of the irreversible fouling layer, R_f' varied significantly with pH and pressure. Little irreversible fouling occurred at pH 6.8 at either pressure; $R_f' = \pm 0.1$. In contrast, significantly larger relative resistances of the irreversible fouling layer were observed at pH 3.8, with the larger value occurring at the higher pressure; $R_f' = 4.3$ at 0.70 MPa and 1.0 at 0.20 MPa.

TABLE 3.
EXPERIMENTAL RESISTANCES AND RELATIVE RESISTANCES OF THE IRREVERSIBLE FOULING LAYER FOR BSA ULTRAFILTRATION WITH A TITANIA MEMBRANE AT u = 2.0 m/s and T = 300K

Pressure (MPa)	pH	$10^{-12}(P/\eta J_{wb})$ (m^{-1})	$10^{-12}(P/\eta J_{wa})$ (m^{-1})	$10^{-12}(P/\eta J_x)$ (m^{-1})	R_f'
0.20	6.8	8.2	7.7	16	-0.1
	4.8	6.2	10.1	25	0.6
	3.8	6.9	14.1	41	1.0
0.70	6.8	5.7	6.0	50	0.1
	4.8	7.4	9.2	60	0.3
	3.8	6.4	34.0	104	4.3

The rejection of BSA was greater at the higher ionic strength employed in this investigation than suggested by the experiments at low ionic strength using similar macroporous titania membranes (Zhang and Spencer 1993). The retention of rejection in the ionic strength range investigated is consistent with increasing aggregation of the BSA or greater fouling of the membrane by the BSA to alter its pore structure as the ionic strength increased. The potential for these phenomena increases with ionic strength and the associated decrease of the Debye length in the solution and electrostatic repulsion between charged proteins of like sign.

The flux increased with increasing pH, which was also accompanied by increasing ionic strength in these buffered solutions. The high flux with almost no irreversible fouling accompanied by high rejection obtained at pH 6.8 recommends this condition for concentrating BSA with the membrane. It also appears possible to utilize the higher pressure without increasing the irreversible fouling significantly and thus obtain a higher productivity while maintaining the reduced need for chemical cleaning.

The variation in flux, rejection and irreversible fouling with pressure at pH 4.8, the pI of BSA, is especially interesting. These results are consistent with BSA aggregation and interaction with the membrane that are weak enough at its pI to be influenced by the pressure difference, or the convective flow, across the membrane.

CONCLUSIONS

BSA rejections in the 0.92 to 0.94 range can be obtained at ionic strengths greater than 0.05 mol/dm^3 with the macroporous titania membrane under controlled conditions of pH and pressure. The rejection increased during the course of the ultrafiltration from a modest to a higher value. The incremental increase depends on pH and pressure and may reflect differences in fouling. High rejection accompanied by the smallest observed flux decline and irreversible fouling were obtained at the highest pH, 6.8, and the lower pressure, 0.2 MPa, suggesting that these operating conditions would be desirable for applications requiring high rejection with minimal flux decline and a simple cleaning regimen.

ACKNOWLEDGMENTS

Support for this research has been received from KBN, Polish Committee of Science, grant BW/RKH-1994. One of the authors (HGS) also gratefully thanks the Polish-U.S. Fulbright Commission for support of this research through a research award. The authors also thank diploma-students, Mr. Marurouski and Mr. B. Stanuch, for their helpful laboratory work.

REFERENCES

ELLMAN, G.L. 1962. The biuret reaction: changes in the ultraviolet absorption spectra and its application to the determination of peptide bonds. Anal. Biochem. *3*, 40–48.

HARRIGAN, W.F. and McCANCE, M.E. 1966. *Laboratory Methods in Microbiology*. Academic Press, London.

KO, M.K. and PELLEGRINO, J.J. 1992. Determination of osmotic pressure and fouling resistance and their effects on performance of ultrafiltration membranes. J. Membr. Sci. *74*, 141–157.

McGREGOR, R. 1974. *Diffusion and Sorption in Fibers and Films*. Vol. 1, Academic Press, New York.

TRZEBIATOWSKA, M., FALKOWSKI, J. and SZANIAWSKI, A.R. 1994. Ultrastructure of TiO_2 layer used as a support for immobilization of enzymes. Environmental Protection Eng., Wroclaw, Poland.

ZHANG, L. and SPENCER, H.G. 1993. Selective separation of proteins by microfiltration with formed-in-place membranes. Desalination *90*, 137–146.

AUTHOR INDEX

Journal of Food Process Engineering **19** (1996) 479-481. *All Rights Reserved.*

SUBJECT INDEX

Journal of Food Process Engineering **19** (1996) 482-483.

UNITED STATES POSTAL SERVICE™

Statement of Ownership, Management, and Circulation

(Required by 39 USC 3685)

1. Publication Title	2. Publication Number	3. Filing Date
JOURNAL OF FOOD PROCESS ENGINEERING	0 1 4 5 - 6 4 9 0	10/1/96
4. Issue Frequency	**5. Number of Issues Published Annually**	**6. Annual Subscription Price**
Quarterly	4	$149.00

7. Complete Mailing Address of Known Office of Publication *(Not printer)* *(Street, city, county, state, and ZIP+4)*
6527 Main Street, Trumbull, Fairfield, Connecticut 06611

Contact Person
John J. O'Neil
Telephone
(203) 261-8587

8. Complete Mailing Address of Headquarters or General Business Office of Publisher *(Not printer)*
6527 Main Street, P.O. Box 374, Trumbull, Connecticut 06611-0374

9. Full Names and Complete Mailing Addresses of Publisher, Editor, and Managing Editor *(Do not leave blank)*

Publisher *(Name and complete mailing address)*
John J. O'Neil, 6527 Main Street, P.O. Box 374, Trumbull, CT 06611-0374

Editor *(Name and complete mailing address)*
Dr. Dennis R. Heldman, 253 Agricultural Engineering, Missouri University, Columbia, MO 65211
Dr. R. Paul Singh, Dept. of Agricultural Engineering, University of California, Davis, CA 956

Managing Editor *(Name and complete mailing address)*
None

10. Owner *(Do not leave blank. If the publication is owned by a corporation, give the name and address of the corporation immediately followed by the names and addresses of all stockholders owning or holding 1 percent or more of the total amount of stock. If not owned by a corporation, give the names and addresses of the individual owners. If owned by a partnership or other unincorporated firm, give its name and address as well as those of each individual owner. If the publication is published by a nonprofit organization, give its name and address.)*

Full Name	Complete Mailing Address
Food & Nutrition Press, Inc.	6527 Main Street, POB 374, Trumbull, CT 06611
John J. O'Neil	53 Stonehouse Road, Trumbull, CT 06611
Michael J. Tulley	3 N. Slope, Union Gap, Clinton, NJ 08809
Kathryn & Christopher Ziko	8 Maria Alicia Dr., Huntington, CT 06484
John J. O'Neil, Jr.	509 Meadow Brook Drive, Columbia, SC 29223

11. Known Bondholders, Mortgagees, and Other Security Holders Owning or Holding 1 Percent or More of Total Amount of Bonds, Mortgages, or Other Securities. If none, check box → ☒ None

Full Name	Complete Mailing Address
None	

12. Tax Status *(For completion by nonprofit organizations authorized to mail at special rates)* *(Check one)*
The purpose, function, and nonprofit status of this organization and the exempt status for federal income tax purposes:
☐ Has Not Changed During Preceding 12 Months
☐ Has Changed During Preceding 12 Months *(Publisher must submit explanation of change with this statement)*

13. Publication Title	14. Issue Date for Circulation Data Below
Journal of Food Process Engineering	March 1996; May 1996; July 1996; Sept. 1996

15. Extent and Nature of Circulation		Average No. Copies Each Issue During Preceding 12 Months	Actual No. Copies of Single Issue Published Nearest to Filing Date
a. Total Number of Copies *(Net press run)*		400	400
b. Paid and/or Requested Circulation	(1) Sales Through Dealers and Carriers, Street Vendors, and Counter Sales *(Not mailed)*	0	0
	(2) Paid or Requested Mail Subscriptions *(Include advertiser's proof copies and exchange copies)*	240	243
c. Total Paid and/or Requested Circulation *(Sum of 15b(1) and 15b(2))*	▶	240	243
d. Free Distribution by Mail *(Samples, complimentary, and other free)*		47	47
e. Free Distribution Outside the Mail *(Carriers or other means)*		0	0
f. Total Free Distribution *(Sum of 15d and 15e)*	▶	47	47
g. Total Distribution *(Sum of 15c and 15f)*	▶	287	290
h. Copies not Distributed	(1) Office Use, Leftovers, Spoiled	113	110
	(2) Returns from News Agents	0	0
i. Total *(Sum of 15g, 15h(1), and 15h(2))*	▶	400	400
Percent Paid and/or Requested Circulation *(15c / 15g x 100)*		84	84

16. Publication of Statement of Ownership
☒ Publication required. Will be printed in the Vol. 19 #4 issue of this publication.
☐ Publication not required.

17. Signature and Title of Editor, Publisher, Business Manager, or Owner — **Date**
John J. O'Neill, Publisher — Oct. 1, 1996

I certify that all information furnished on this form is true and complete. I understand that anyone who furnishes false or misleading information on this form or who omits material or information requested on the form may be subject to criminal sanctions (including fines and imprisonment) and/or civil sanctions (including multiple damages and civil penalties).

GUIDE FOR AUTHORS

If the manuscript has been produced by a word processor, a disk containing the manuscript would be greatly appreciated. Word Perfect 5.1 is the preferred word processing program. The original and THREE copies of the manuscript should be sent along with the disk to the editorial office. The typing should be double-spaced throughout with one-inch margins on all sides.

Page one should contain: the title, which should be concise and informative; the complete name(s) of the author(s); affiliation of the author(s); a running title of 40 characters or less; and the name and mail address to whom correspondence should be sent.

Page two should contain an abstract of not more than 150 words. This abstract should be intelligible by itself.

The main text should begin on page three and will ordinarily have the following arrangement:

Introduction: This should be brief and state the reason for the work in relation to the field. It should indicate what new contribution is made by the work described.

Materials and Methods: Enough information should be provided to allow other investigators to repeat the work. Avoid repeating the details of procedures that have already been published elsewhere.

Results: The results should be presented as concisely as possible. Do not use tables *and* figures for presentation of the same data.

Discussion: The discussion section should be used for the interpretation of results. The results should not be repeated.

In some cases it might be desirable to combine results and discussion sections.

References: References should be given in the text by the surname of the authors and the year. *Et al.* should be used in the text when there are more than two authors. All authors should be given in the Reference section. In the Reference section the references should be listed alphabetically. See below for style to be used.

RIZVI, S.S.H. 1986. Thermodynamic properties of foods in dehydration. In *Engineering Properties of Foods*, (M.A. Rao and S.S.H. Rizvi, eds.) pp. 133-214, Marcel Dekker, New York.

MICHAELS, S.L. 1989. Crossflow microfilters ins and outs. Chem. Eng. *96*, 84-91.

LABUZA, T.P. 1982. *Shelf-Life Dating of Foods*, pp. 66-120, Food & Nutrition Press, Trumbull, CT.

Journal abbreviations should follow those used in Chemical Abstracts. Responsibility for the accuracy of citations rests entirely with the author(s). References to papers in press should indicate the name of the journal and should only be used for papers that have been accepted for publication. Submitted papers should be referred to by such terms as "unpublished observations" or "private communication." However, these last should be used only when absolutely necessary.

Tables should be numbered consecutively with Arabic numerals. The title of the table should appear as below:

TABLE 1.
ACTIVITY OF POTATO ACYL-HYDROLASES ON NEUTRAL LIPIDS, GALACTOLIPIDS AND PHOSPHOLIPIDS

Description of experimental work or explanation of symbols should go below the table proper. Type tables neatly and correctly as tables are considered art and are not typeset. Single-space tables.

Figures should be listed in order in the text using Arabic numbers. Figure legends should be typed on a separate page. Figures and tables should be intelligible without reference to the text. Authors should indicate where the tables and figures should be placed in the text. Photographs must be supplied as glossy black and white prints. Line diagrams should be drawn with black waterproof ink on white paper or board. The lettering should be of such a size that it is easily legible after reduction. Each diagram and photograph should be clearly labeled on the reverse side with the name(s) of author(s), and title of paper. When not obvious, each photograph and diagram should be labeled on the back to show the top of the photograph or diagram.

Acknowledgments: Acknowledgments should be listed on a separate page.

Short notes will be published where the information is deemed sufficiently important to warrant rapid publication. The format for short papers may be similar to that for regular papers but more concisely written. Short notes may be of a less general nature and written principally for specialists in the particular area with which the manuscript is dealing. Manuscripts that do not meet the requirement of importance and necessity for rapid publication will, after notification of the author(s), be treated as regular papers. Regular papers may be very short.

Standard nomenclature as used in the engineering literature should be followed. Avoid laboratory jargon. If abbreviations or trade names are used, define the material or compound the first time that it is mentioned.

EDITORIAL OFFICE: DR. D.R. HELDMAN, COEDITOR, *Journal of Food Process Engineering*, Food Science/Engineering Unit, University of Missouri-Columbia, 235 Agricultural/Engineering Bldg., Columbia, MO 65211 USA; or DR. R.P. SINGH, COEDITOR, *Journal of Food Process Engineering*, University of California, Davis, Department of Agricultural Engineering, Davis, CA 95616 USA.

JOURNAL OF FOOD PROCESS ENGINEERING VOLUME 19, NUMBER 4

CONTENTS